POLITECNICO DI TORINO

Dipartimento di Ingegneria Chimica e dei Materiali

Corso di Laurea Magistrale in Ingegneria dei Materiali

Tesi di Laurea Magistrale

Investigation on microstructure, mechanical properties and corrosion resistance of AISI P20 steel produced with Wire Arc Additive Manufacturing

Relatori:

Prof. Daniele Ugues

Dr. Ir. M.J.M. Hermans

Dr. Constantinos Goulas

Candidato:

Benedetto Antonio di Castri

Novembre 2018

Contents

Introduction

This thesis focused on the 3D printing of P20 steel. This is an innovative field from the process and material point of view. The research has been conducted during an internship in RAMLAB, a start-up in the port of Rotterdam. This company as experience in the 3D printing of large component for maritime applications. One of the most successful project is the printing of the WAAMpeller, a propeller made of Nickel Aluminum Bronze (NAB).

The aim of this research is to investigate the microstructural evolution of P20 steel during Wire Arc Additive Manufacturing, understand how the thermal cycle affects the microstructure and the material properties. Since WAAM is a novel technique that involved particulars thermal cycles, a study on microstructure development on WAAM part has been performed to predict the material behavior during deposition. The material structure is strictly related to the thermal cycle that the material experiences.

The microstructural investigation during WAAM represents a complex topic. In order to approach correctly the problem different experiments and analysis are performed:

- Measurement of the thermal cycle;
- EPMA for segregation of alloying elements;
- Dilatometry to measure the solid state transformation temperatures of the material;
- Microstructural investigation using different etching techniques;
- The main questions to be answered are:
- Which microstructure characterizes the 3D printed P20 steel and which are the main differences with the traditional one;
- Are the properties of the 3D printed P20 steel comparable with the traditional one?;
- Is it possible to avoid the post-deposition heat treatment?;

1 Literature review

1.1 General overview

1.1.1 Plastic injection molding

Plastic injection molding is a process where a polymer is injected in a cavity by application of pressure and heat. Due to the high production capabilities, accuracy and ability to produce complex parts, plastic injection molding finds application in different fields such as automotive, aerospace and in common objects used in everyday life.

During the process, the pressure inside the mold can vary between 80-300 MPa depending on the type of material, while the temperature can vary between 140-300°C (He, 2011). The final product, called plastic, consists of a mixture of agents with different functions (Preciado and Bohorquez, 2006):

- The polymer, which acts as a matrix;
- Additives, which give additional properties to the plastic, such as flame and UV resistance, impermeability and electrical conductivity. Additives can also be added to decrease the cost of the final product;
- Reinforcement are also introduced in polymer matrixes to increase the mechanical properties of the final product;

The thermal-mechanical cycling loading in presence of abrasive particles, which can also produce corrosive agents, promotes the damage of the mold. Since the tolerances of the surface accuracy are low in the plastic injection molding, the failure of the mold attracts a lot of interest.

The mold manufacturing process starts with a steel bloom (dimensions of which can reach 1x1x1 m^3). This bloom is produced by ingot casting and with subsequent forging to obtain a squared shape. After the forging dehydrogenization is performed. Following post processing such as quenching and multiple tempering are performed to obtain proper toughness, strength and hardness for the application. These mechanical properties are determined by the microstructure. The process of mold manufacturing is proposed in Figure 1.1

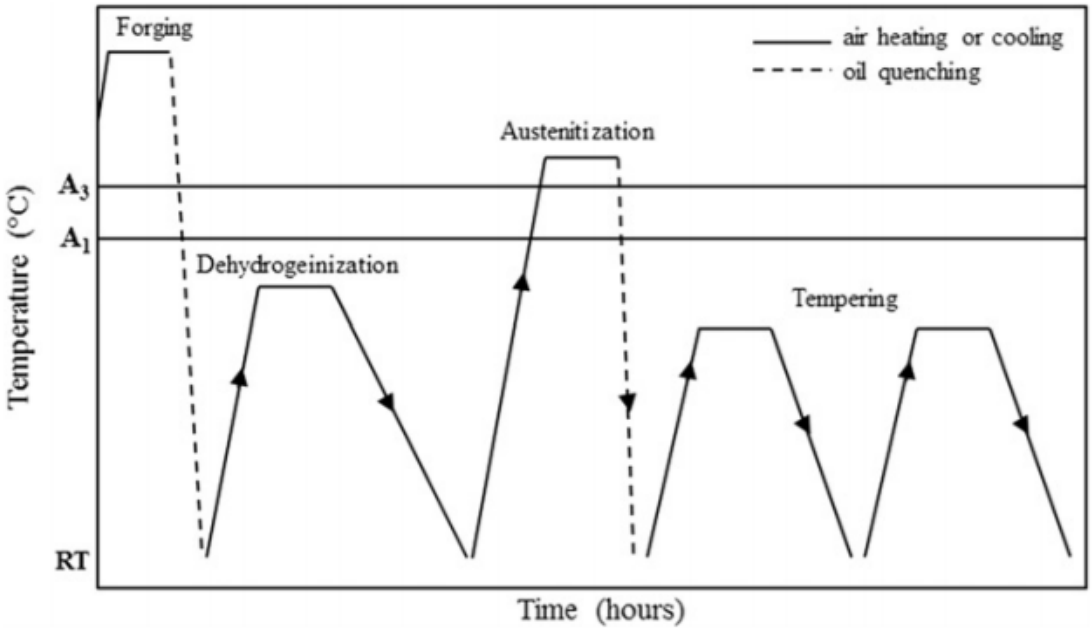

Figure 1.1 General process of mold manufacturing and related heat treatment (Firrao et al., 2013)

1.1.2 Material

The material selection concerns two main aspects. The material should be suitable for mold manufacturing process and its properties should meet the application requirements. An ideal mold material should have good machinability and good surface finishing, since the traditional mold manufacturing starts from solid forged metal block to obtain the net-shape part. The material properties include hardness, wear resistance, corrosion resistance, fatigue strength, core strength, toughness and dimensional stability are the main requirements (He, 2011) (Roberts, Krauss and Kennedy, 1998). The hardenability of the material during the heat treatment of the bloom is also important. The hardness should be homogenous to ensure equal performances at the core and at the surface of the final mold. Luo et all studied microstructure and hardness uniformity in a non-quenched pre-hardened steel (Luo et al., 2009). According to their study it is possible to obtain pre-hardened conditions also without the application of the quenching and tempering process, which might include hardness inhomogeneities and quench cracking in the part.

AISI P20 has been used for this study because it is one of the commonly used plastic injection molding materials. Traditionally, this steel is at pre-hardened state with hardness ranging between 30-50 HRC. The chemical composition and properties are summarized in Figure 1.2 and 1.3 respectively. Comparing with the other tool materials, P20 presents low wear resistance. Thus surface heat treatments are performed to increase performances. In the section 1.3.3 the mold heat treatment is reviewed with some practical examples.

The microstructure of P20 consists mainly of martensite and bainite. This has been reported in different works (Chen, Xue and Lijue, 2002) (Zhang et al., 2011).

The ideal austenitization temperature is 890 °C, higher values will lead to grain coarsening which negatively affects material properties. The hardness of P20 after quenching is 52 HRC. After tempering at 590 °C the material hardness reduces to 28-35 HRC as small carbides form between the martensite laths. Increasing the tempering temperature will promote the coarsening of the carbides, which has negative effects on the material properties.

Type	UNS No.	Composition(a), %								
		C	Mn	Si	Cr	Ni	Mo	W	V	Al
Low-carbon mold steels										
P2	T51602	0.10 max	0.10–0.40	0.10–0.40	0.75–1.25	0.10–1.50	0.15–0.40	...	...	...
P3	T51603	0.10 max	0.20–0.60	0.40 max	0.40–0.75	1.00–1.50	...	...	...	...
P4	T51604	0.12 max	0.20–0.60	0.10–0.40	4.00–5.25	...	0.40–1.00	...	...	...
P5	T51605	0.10 max	0.20–0.60	0.40 max	2.00–2.50	0.35 max	...	...	...	...
P6	T51606	0.05–0.15	0.35–0.70	0.10–0.40	1.25–1.75	3.25–3.75	...	...	...	...
P20	T51620	0.28–0.40	0.60–1.00	0.20–0.80	1.40–2.00	...	0.30–0.55	...	...	...
P21	T51621	0.18–0.22	0.20–0.40	0.20–0.40	0.50 max	3.90–4.25	...	...	0.15–0.25	1.05–1.25

Figure 1.2 Chemical composition of different plastic mold steels (Roberts, Krauss and Kennedy, 1998)

1.2 Mold regeneration

Sustainable and economic pressures drive industry to repair and remanufacture the damaged components to minimize environmental impact, material waste and energy consumption. The mold industry is not an exception. As the surface finishing is important for a mold, repair and regenerating the mold with good surface finishing is important. To be able to increase the service time of the mold further investigation on optimal chemical composition, mechanical properties, heat treatment, surface accuracy and durability is needed.

Increased service time of a mold is very important according to the concept of circular economy. The circular economy is an idealized closed-loop in which material wasting, energy consumption and environmental impacts are minimized by repairing, re-use, re-manufacturing, recycling and recovery the ex-serviced components before exiting their life cycle.

The mold can be re-used when it can still withstand less critical working condition. Re-manufacturing includes the dismantling, restoring and substitution of parts of a product. Recycling is a process involving physical, chemical and electrochemical reactions, aiming to bring back the material to its original quality. Recovery consists in conversion of the material in energy. In Figure 1.4 is shown the material source system.

Factor	For hobbed and/or carburized cavities					For machined cavities				
	P2	P3	P4	P5	P6	P20	P21	13Cr–0.12C	13Cr–0.35C	17Cr–0.65C
Major factors										
Wear resistance	1(a)	1(a)	1(a)	1(a)	1(a)	1(a)	1	2	3	5
Toughness	9	9	9	9	9	8	8	8	6	5
Hot hardness	2(a)	2(a)	4(a)	2(a)	3(a)	2(a)	4	5	6	6
Minor factors										
Usual working hardness, HRC	58–64(a)	58–64(a)	58–64(a)	50–64(a)	58–61(a)	30–50	36–39	40–42	50–53	51–57
Depth of hardening	S	S	M	S	M	M	D	M	M	M
Finest grain size at full hardness, Shepherd standard	...	...	...	...	...	7½	...	...	7	7½
Surface hardness as-quenched, HRC	62–65(a)	62–64(a)	62–65(a)	62–65(a)	60–62(a)	52–54	22–26	40–43	50–53	55–58
Core hardness (25 mm, or 1 in., diam round), HRC	15–21	15–21	33–35	20–25	35–37	45–50	22–26	40–43	50–53	55–58
Manufacturing factors										
Availability	2	1	2	2	2	3	2	1	1	1
Cost	1	1	2	1	1	1	2	2	2	2
Machinability	7	7	5	7	6	8	5	4	4	4
Quenching medium	O	O	A,O	O, W	O	O	O	O, A	O	O,A
Hardening temperature, °C (°F)	830–845(a) (1525–1550)	800–830(a) (1475–1525)	885–925(a) (1625–1700)	845–870(a) (1550–1600)	790–815(a) (1450–1500)	815–870 (1500–1600)	870–900 (1600–1650)	955–1010 (1750–1850)	980–1040 (1800–1900)	1010–1065 (1850–1950)
Dimensional change on hardening	M	M	M	M	M	M	M	M	M	M
Safety on hardening	M	M	M	M	M	M	H	H	M	M
Susceptibility to decarburization	M	M	M	M	M	M	L	M	M	M
Approximately hardness as-rolled or forged, HB	200	200	350	230	280	310	...	400	500	550
Annealed hardness, HB	103–123	109–137	116–135	103–123	180–207	150–180	248–269	150–180	160–202	187–228
Annealing temperature, °C (°F)	730–815 (1350–1500)	730–815 (1350–1500)	870–900 (1600–1650)	845–870 (1550–1600)	675–695 (1250–1280)	760–790 (1400–1450)	870–900 (1600–1650)	790–845 (1450–1550)	845–900 (1550–1650)	845–900 (1550–1650)
Tempering range, °C (°F)	150–260 (300–500)	150–260 (300–500)	150–260 (300–500)	150–260 (300–500)	150–230 (300–450)	150–260 (300–500)	580–540 (900–1000)	260–425 (500–800)	150–425 (300–800)	150–425 (300–800)
Forging temperature, °C (°F)	1010–1120 (1850–2050)	1010–1120 (1850–2050)	1010–1120 (1850–2050)	1010–1120 (1850–2050)	1065–1175 (1950–2150)	1010–1120 (1850–2050)	...	1120–1175 (2050–2150)	1095–1205 (2000–2200)	1095–1150 (2000–2100)

Figure 1.3 General overview of the properties of different mold steel. The ranking is based on a 1 to 9 scale, where 1 means low and 9 high. a) after carburizing (Roberts, Krauss and Kennedy, 1998)

It also illustrates the involved different stages of material life cycle. Depending on the material (component) which has to be re-used or re-manufactured or recycled, the material enters different states by applying different solutions.

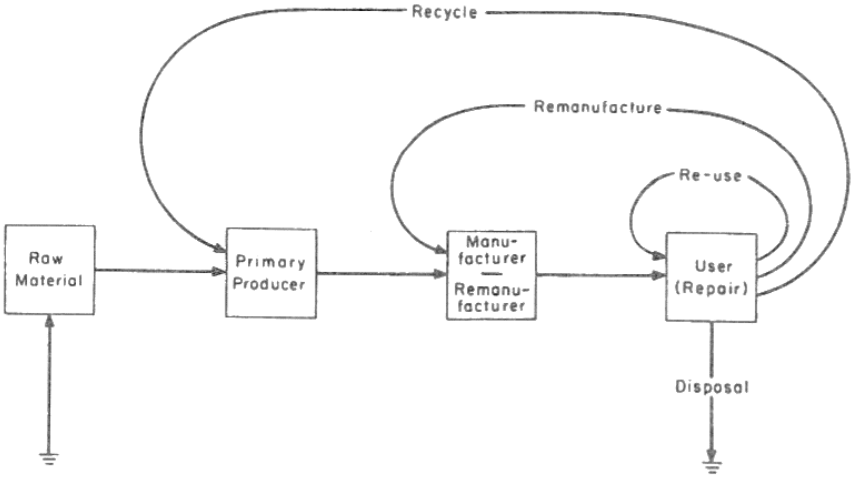

Figure 1.4 Material resource system (Lund, 1981)

In the case of dies much efforts have been made to stimulate the application of repair and remanufacturing/refurbishing technique to increase the service life of the tools (Chen et al., 2014). It is estimated that the adoption of the circular economy offers extending of the dies service life and cost reduction.

There is a slight difference between remanufacturing and refurbishing, according to (Leino, Pekkarinen and Soukka, 2016) . Remanufacturing restores the product quality to an “as new” condition (usually by the manufacturers), while refurbishment brings the product to an acceptable condition and this can also be conducted by third parts.

According to (Lund and Hauser, 2010) criteria must be followed to remanufacture a component, since not all the parts have the requirement to undergo a similar process. The criteria include:

- Ability to be disassembled: help in inspection, damage detection and accessibility for repairing;
- Repair the damage to the quality level of the core material;
- In some case a good weldability is needed if welding is the adopted repair technique;
- Sufficient added value of the core material: it must be economically convenient to re-manufacture the part;
- Enough technology level and value on the market;

In practice, the die repair involves disassembly, cleaning, evaluation of the repair potential, repair or substitution, refurbishment and assembly. The repair itself involves many steps that are currently performed manually, which is a time consuming and high labor cost process. Many logistic and technical issues are still challenging and can cause delays during repairing process. As there is a need in saving time and reducing cost, it is important to automate the repairing process to ensure the work flow smoothly. This requires designing the whole process accordingly . Digitally controlled repair can initiate future research trend as the design for remanufacturing is defined as "A combination of design processes whereby an item is designed to facilitate remanufacture" (Charter and Gray, 2008)

1.3 Damage and Failure mechanism of plastic molds

1.3.1 Wear

Relative sliding of solid surfaces promotes frictional forces leading to material removal, which refers to wear. This is a tribological phenomenon depends on materials involved and their service environment (Kato, 2002). According to Kato there are three types of wear mechanisms: mechanical, chemical and thermal wear. Mechanical wear is the surface fracture and deformation. Ductile and brittle materials behave differently, the ductile materials are prone to plastic deformation while the brittle materials are prone to fracture. Chemical wear is based on the contact between two surfaces where chemical reaction is taking place. The friction accelerates the chemical reaction, and it usually creates a new film called as tribo-film. Thermal wear is a process in which the local melting of material takes place.

The aforementioned classification needs further extension to specific wear models. Therefore abrasive, adhesive, fatigue wear and tribo-chemical wear will be treated. These type of wear are usually contributing to the final damage of the tool. Bergstrom et al. (Bergstrom et al., 2001) reported that these mechanisms occur simultaneously during the service of a component but the dominant wear damages is different based on the application.

Modeling of these mechanisms is important for a better design of the molds. However practical cases are more complicated than the models as assumptions are often made to simplify the problem. This creates strong boundary which may deviating the simulation results from the practice. Different studies have already emphasizes on the difficulties encountered during the development of models to predict the wear mechanism in plastic injection molds (Kato, 2002) (Bergstrom et al., 2001). The main reason is the large number of parameters that can vary during the process. For example, the geometry of the mold affects the nature of wear, which is difficult to simulate even by experiments. The material properties regulate the wear rate. In practice, material properties are optimize through heat treatments (Firrao et al., 2009) and surface coatings to reduce the surface degradation. Apart from the hardness, surface roughness, geometry of the asperities and their distance, temperature, presence of corrosive agents, local

sliding velocity are parameters that can affect the wear rate. The detail of different wear mechanisms are presented in the following paragraphs.

1.3.1.1 Adhesive wear

Adhesive wear is based on the formation on junctions between sliding surfaces promoted by the normal applied stress. The continuous loading on the surface induces the fracture of the adhered part, causing the formation of particles that increase the wear. In Figure 1.5 a schematic drawing of the adhesive wear is illustrated.

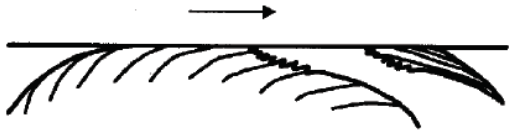

Figure 1.5 Adhesive wear by adhesive shear (Gahr, 1987)

On the interface between sliding surfaces covalent or non-covalent bonds fomr by interaction of the surfaces. The nature of these bonds is related to the crystal structure, composition and affinity of the two materials. This phenomenon can be explained from both mechanical and physio-chemical point of view (Sikorski, 1964). On one hand, the mechanical theory derives from the idea that the crystal structures prone to plastic deformation, have higher adhesion coefficient, defined as the ratio between the force to break the junction and the normal applied force. The increase in plastic deformation leads to an increment of the real contact area, which maximizes the interaction between the two materials. Thus, crystal structures, such a face center cubic (FCC), promote the adhesion mechanism, while hexagonal structures present lower adhesion coefficient. On the other hand the physio-chemical theory is based on the minimization of the surface energy. Materials with high surface energy tend to have higher adhesion coefficient because of the increased number of interactions, which lead to more adhesion.

Adhesion wear can be described mathematically by Eq.1 valid for elastic materials:

$$V = K\frac{WL}{H_v} \tag{1}$$

Where K is the wear coefficient that depends on the type of systems, W is the applied normal load, L is the sliding distance and H_v is the hardness of the softer material.

1.3.1.2 Abrasive wear

Abrasive wear is the removal of material caused by the presence of hard particles in one or both the sliding surfaces (Gahr, 1987). Hard particles could be materials that naturally shows this properties or asperities that act as hard due to their sharp geometry. This mechanism can be described by the Eq.2:

$$V = \alpha\beta \frac{WL}{H_V} \tag{2}$$

where α is a shape factor of the asperity and β the degree of wear at one asperity.

Abrasive wear can be classified in two-body abrasion and three body abrasion. In the first type the hard particles are contained in the material surface, while in the second they lie on the interface between the two sliding surfaces. This case is similar to practical case of the plastic injection molding, where the polymer matrix is mixed with additives or fibers. In Figure 1.6 the schematization of the four types of abrasive wear are illustrated. They are: microploughing, microcutting, microfatigue and microcracking. A detailed description of these processes is proposed in the literature (Gahr, 1987).

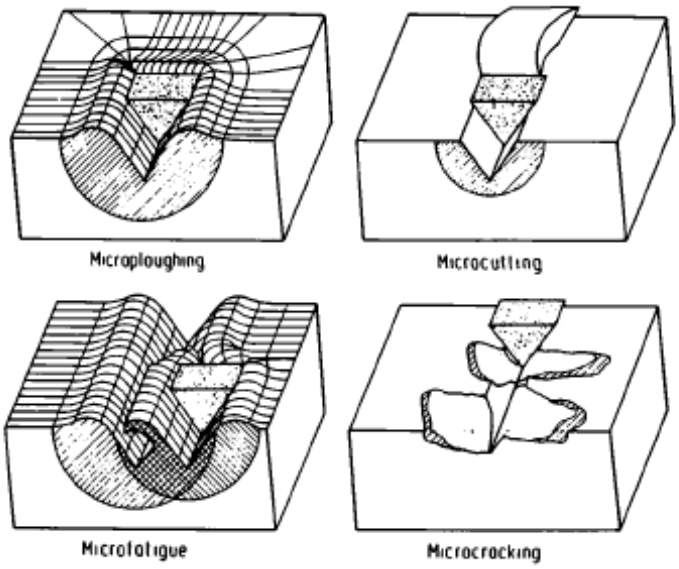

Figure 1.6 Schematization of micro-ploughing, microcracking, micro-fatigue and microcracking cause by abrasion of steel by hard abrasive material (Gahr, 1987)

1.3.1.3 Fatigue wear

Fatigue wear refers to damage caused by repeated or alternating loading on solid surfaces. This can be initiated by fluids or contact with solid surface. This mechanism is that cracks nucleate on the surface (surface crack) or beneath (sub-surface cracks) leading to propagation and eventually failure of the material. Surface cracks are generated by fretting (displacements of solid surfaces) or solid contacts, while sub-surfaces cracks nucleate at the interface of inclusions or carbides, where the shear stress is maximum. In Figure 1.7 the schematization of fatigue cracks is proposed. Surface fatigue can also be caused by cyclic adhesive and abrasive wear, thus the fatigue wear in couplings with more wear mechanism is possible.

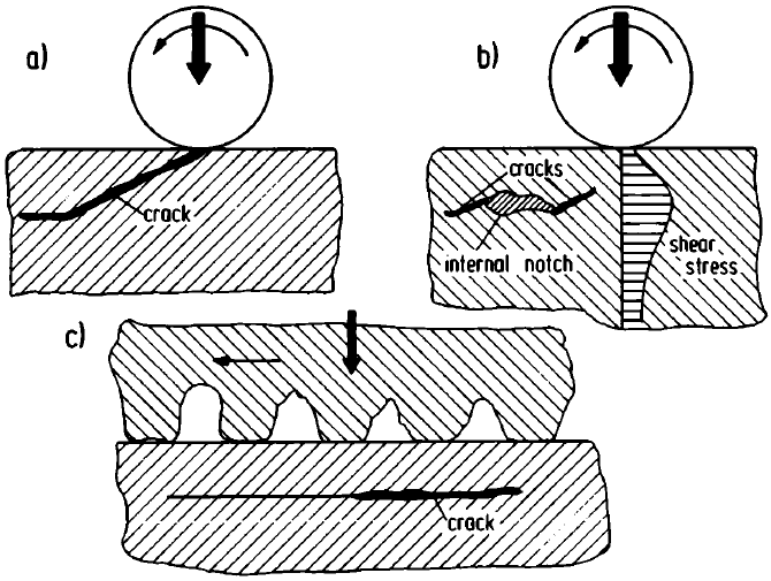

Figure 1.7 Different type of fatigue wear: a) surface crack, b) crack generated by internal notches and c) subsurface crack (Gahr, 1987)

Fatigue wear in the high cycle range can be described with a law similar to the Basquin relation as can be seen in Eq. 3 (Kato, 2002):

$$N_f = b\, W^{-n} \tag{3}$$

where N_f is the fatigue limit, b and n are experimental constant that depends on the type contact. The crack propagation can be investigated with a linear fracture mechanics model of a propagating sub-surface crack:

$$\frac{da}{dN} = c\Delta K^m \tag{4}$$

where a is the crack length, N is the number of cycle, c and m are experimental constants and ΔK is the the variation in the stress intensity factor.

Tribo-chemical wear

Corrosive wear is also called tribo-chemical wear, where the solid surfaces are in contact with and reacts to the service environment. The process can be summarized and schematically shown in Figure 1.8. At low chemical reactivity there is not reaction of the metal surface, thus the wear mechanism is mostly adhesive. Increasing the reactivity, a thin protective layer forms a coating. This coating has higher hardness than the metal substrate, thus it decreases the wear and prevent the material removal. If the chemical reactivity raises, the width of the film increases making the protective oxide more brittle. In this condition abrasive wear mechanism is preferred. The overall process is regulated by the continuous formation and removal of the oxide layers.

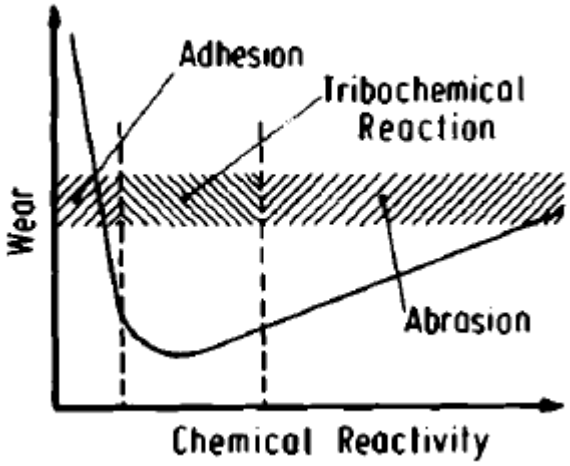

Figure 1.8 Plot of the wear in function of the chemical reactivity of the environment (Gahr, 1987)

The delamination of the oxide layers occurs when it reaches a critical width ζ, hence the wear coefficient K can be expressed in Eq. 5 (Gahr, 1987):

$$K = dA\,\frac{\exp(\frac{-Q}{R_g T})}{\zeta^2 \rho^2 U} \tag{5}$$

where A is the Arrenhius constant, Q is the activation energy of the reactions assumed to be constant during the process, R_g is the gas constant, T is the absolute temperature, ρ the density of the oxide, U the sliding velocity and d the distance of the wearing contact. Eq. 5 underlines

an important concept behind the corrosive wear, the fact that is strictly dependent on the kinetic of the process. As can be seen in Eq. 5 the wear coefficient increases when the temperature increases, because it the temperature enhances the chemical reactivity of the substances.

1.3.2 Corrosion in plastic injection molds

Corrosion can be considered as a degradation process of the system (the material) through chemical reaction with the environment. During this process a redox reaction takes place, which involves oxidation and reduction of species through electron exchange. The presence of corrosion requires three elements: anode, cathode and electrolyte. At the anode the oxidation process leads to material degradation with deposition of new material (usually oxides from the previous metal species), while at the cathode reduction of material occurs. The function of the electrolyte is to transfer the electrons from the anode to the cathode. Electrolytes can be found in solid or liquid state, but usually when corrosion takes place they are in the liquid states (aqueous solutions such as salty water). The anodic or cathodic reactions can be studied by looking into the tendency of substances to be reduced or oxidized by other species, which is called electrochemical potential. In the galvanic series positives values of the potential give higher corrosion, while negatives values are related with cathodic reaction.

The material can react to the corrosive environment in different ways: passivation, corrosion and immunity. Passivation is the formation of a compact oxide layer that protect the material from corrosion, corrosion is the oxidation process of the material and immunity is when the material does not react to the environment. In Figure 1.9 the Pourbaix diagram of Iron is illustrated. This diagram shows the equilibrium of electrochemical reactions of elements in function of potential (E) and pH value. In Figure 1.9 three types of lines are present: constant pH (vertical lines), constant E (horizontal lines) and variable pH values and potential (obliquus lines). This means that it is possible to obtain the same product by increasing only the pH value while the E is constant or the same product can be obtained in two reactions where the first is constant PH value and the second constant E.

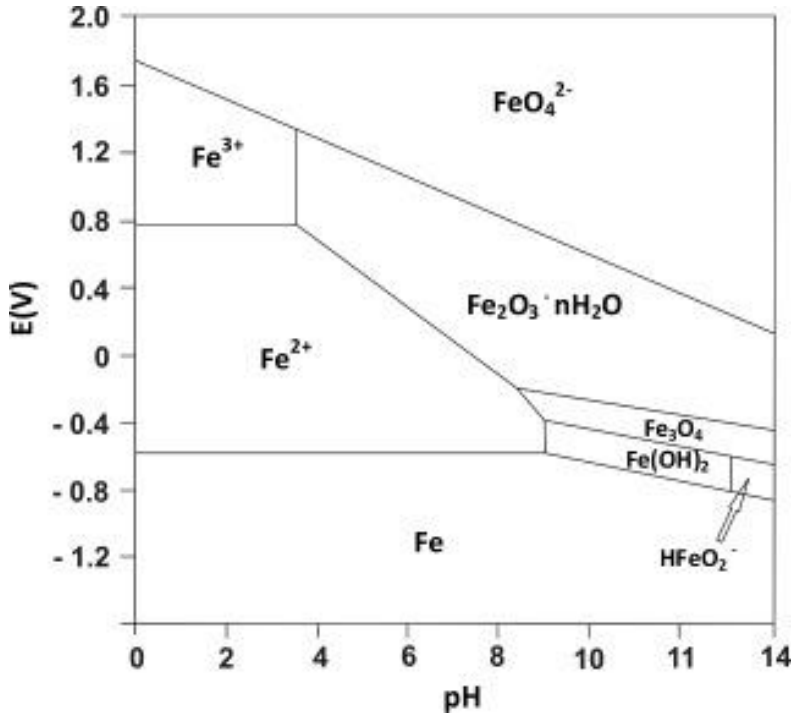

Figure 1.9 Pourbaix diagram of Fe

The most important corrosion mechanisms are listed as:

- Pitting corrosion: it represents a harmful type of corrosion that is focused on local discontinuities (carbides, precipitates and other types of damages) of the passivation layer. It is characterized by high corrosion rate, since the pit (anode) is much smaller than the cathode.;
- Galvanic corrosion: it occurs when material with different potential are in contact and an electrolyte is present, such as in double-phase materials;
- Intergranular corrosion: it takes place on the grain boundary where usually carbides precipitate (for example Cr carbides), the neighboring grain are deprived of alloying elements with effect on the electrochemical potential. Thus reaction can take place between species at the grain boundaries and the grains;
- Stress corrosion: it is usually related to applied loads in presence of corrosive agents that modify the mechanical properties of the material. This phenomenon is also linked with fracture mechanics, since corrosive processes can lead to embrittlement. This type of corrosion is often related with intergranular corrosion;
- Fatigue corrosion: it is observed when alternating loading is accompanied by corrosive agents. The oxidative reaction can enhance crack nucleation, propagation and failure. During nucleation, the presence of corrosion products can facilitate the crack nucleation at the surface. In the case of pitting, the reaction from local spots around carbides and precipitate can lead to material removal that can act as a surface defect, harmful for fatigue nucleation. During

propagation of the crack, the crack type can experience oxidation, thus embrittlement that can help the crack propagation;

- Crevice corrosion: it is related with narrow spaces where high concentration of corrosive species are present. For examples in the case of bolts in salty water, Cl ions could diffuse in the interface under the bolt leading to high concentration of ions and reactions of the joint;

In plastic molds corrosion is typically coupled with wear process. The damage process is complicated and has not been widely studied in literature, although coupling effects have been reported (Wen, 2009a) (Wen, 2009b). The wear component is given mainly by additives or reinforcements that abrade the surface, while the production of corrosive substances by degradation of the polymer matrix due to overheating promote corrosion of the tool.

According to Wen, the mechanism with which corrosion starts is pitting, due to the local damage of the passive layer. In their study the description of the relation between erosion and corrosion was attempted, to prove this an erosion-corrosion test has been performed on NAK80, a tool steel for plastic injection molds. The main result from their study is the knowledge that corrosion is influenced by the shape of the damages area during the worn of the surface. The shape and geometry of the abrasion is strictly related with the attack angle, velocity and particle size. During the corrosion-erosion test some pits start to appear on the damaged area, during time the pitting start to increase even more. Cracks starts to nucleate and propagate around the pitting area, due to the fatigue wear. These cracks propagate from the boundary of the pitting area and afterwards they interact. The presence of this cracks enhance the corrosion process, since the crack acts as a anode, while the matrix as a cathode. The attack angle is an important feature in the prediction of the material behavior. The study highlights that for the tested material the maximum of the erosion-corrosion degradation occurs at impact angles where the wear mechanism changes. At low values the surface is only scratched, increasing the angle plastic deformation and current of the surface start to be more important. Between 30 and 45° the material is taken out from the surface leading to larger damaged areas. Increasing more the impact angle, the damage starts to reduce in dimension, since the material is subject only to impact/compressive loading and the shear component are even more reduced going towards the 90° angle. The erosion-corrosion rate is proposed in Figure 1.10, the trend around 30-45° is clear in the picture. The effect of the impact velocity shown in the graph also, as can be expected increasing the impact velocity causes higher degradation rate for all the impact angle. The particle dimension, as expected, also has a role in the damage mechanism, in fact the increasing the particle size, the degradation rate is almost double the value.

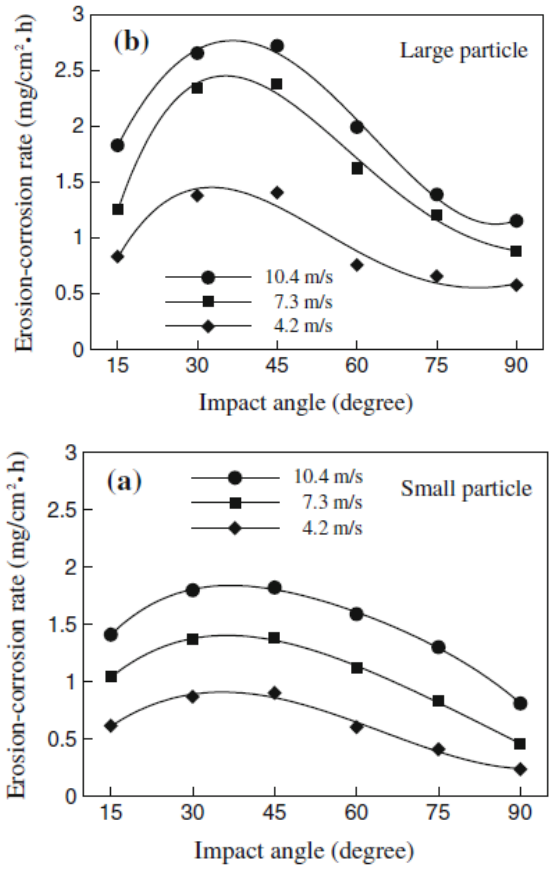

Figure 1.10 Erosion corrosion behavior of NAK80 under different impact velocity conditions (Wen, 2009a)

1.3.3 Heat treatment

Fatigue strength, thermal stability, wear resistance, toughness and in some cases corrosion resistance of the mold material are important. The mold used for plastic injection experiences the cyclic thermo-mechanical loading (temperature depends on the type of polymer), and abrasive wear due to the presence of additives and reinforcements. Corrosion resistance of the mold is required as for particular polymers which can cause corrosive environment. Heat treatments play an important role to obtain the material properties for manufacturing the mold. To meet different properties requirement for different applications, the heat treatment procedures of the mold can be different:

- Pre-hardened: the mold is treated with a quenching and tempering heat treatment;
- Post roughing hardened steel: the mold receives the hardening treatment after the roughing process;
- Case hardening steels: the mold undergoes a special surface treatment to increase the hardness of the surface, while the core preserve its toughness;

- Corrosion resistant steels: adding alloying elements to achieve special corrosion properties against aggressive agents;
- Precipitation hardening steels: the material is subjected to ageing in order to promote precipitation of carbides, that increase uniformly the mechanical properties of the mold.

Wear contributes to most of the total damages in plastic injection molds, it is important to prevent premature failure of the mold. There different ways to counteract the problem of worn tool surface:

- Heat treatment (quenching and tempering) and surface treatment (nitriding, carburizing, laser cladding);
- Surface smoothness;
- Use of less abrasive particles;
- Increase lubrication;

As described in the previous section wear is related with the hardness of the softer material, increasing the mechanical properties benefits are yielded from the wear damage point of view. Heat treatment and surface treatment are the common used tools to increase the wear properties of mold and die material. Their beneficial effect stands on the microstructure control of the material and increase in mechanical properties.

A common practice for plastic mold steels is the quenching and tempering (QT) heat treatment (pre-hardened state) that consists of three stages:

- Solubilization;
- Quenching;
- Multiple tempering;

In the solubilization step the mold is heated above the A_{C3} to convert the original phases to austenite. This stage is characterized by phase transformation of the previous microstructure into austenite. The temperature is hold until the phase transformation is completed and all the alloying elements solubilize, thus the holding time is a key factor in terms of final result and also cost. The austenitization temperature is a key factor for high carbon steels and large components. In the first case the high content of C stabilize the austenite and lowered the A_{c1}, hence they can suffer grain coarsening. The same issues can be encountered in the case of large components (such as molds) where the holding time is increased to ensure complete and homogenous austenitization and alloys solubilization.

During the quenching the component is rapidly cooled below the M_s temperature, (the temperature at which the metastable martensite transformation takes place). This transformation can be defined as military since it is diffusion-less and it evolves by cooperated atoms movements at the interface. During the transformation the carbon atoms present in the FCC cell of the Fe crystal structure are constrained in the octahedral interstitial, and they are not able to diffuse due to the low cooling time. According to the Fe-C equilibrium phase

diagram at room temperature the stable crystal structure is the BCC, in contrast the saturated lattice avoid the equilibrium transformation. Hence the Fe atoms arrange in a body centered tetragonal (BCT) lattice with C atoms in the octahedral sites. This transformation is accompanied by volume expansions that introduces residual stresses in the microstructure. During the transformation the new lattice is accommodated by the austenite matrix through introduction of dislocations (result of twinning and slip). In Figure 1.11 two types of martensite are displayed, lath, and plate martensite. The difference in morphologies are explained in reference of (Stormvinter, Hedström and Borgenstam, 2011). It is important to point out that at low carbon content the lath morphology formation is more favorable while at the higher carbon contents the plate-like martensite is more prone to form.

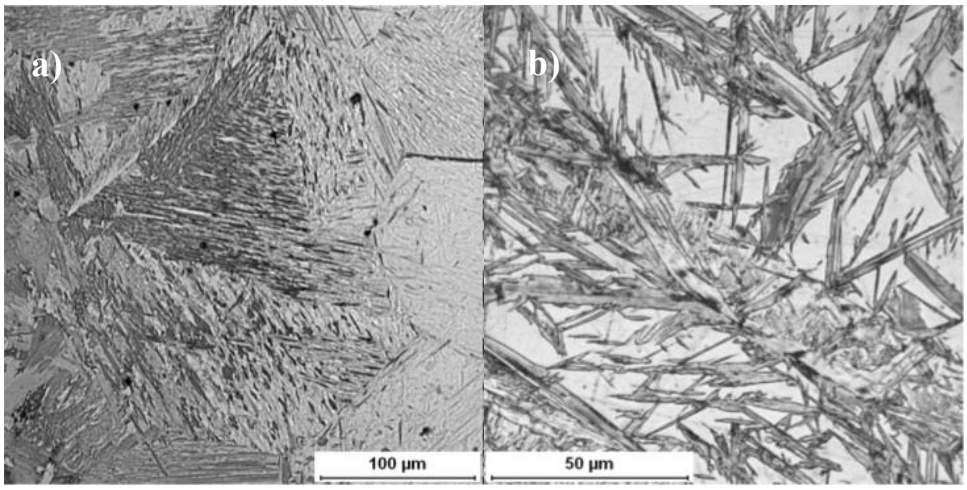

Figure 1.11 Martensite microstructure: a) lath martensite and b) plate martensite (Stormvinter, Hedström and Borgenstam, 2011)

The martensite phase is a metastable phase, with high interfacial energy, high residual induced stresses and high number of dislocation, resulting in a very brittle microstructure. Tempering is the process of heating the martensite phase in order to release the entrapped energy of the system. There several stages of tempering and all of them result in different type of final phase morphologies. For molds industry tempering is performed above 550 °C to enable precipitation of fine alloying carbides, promote dislocation rearrangement and decrease the internal energy of the system. Another important scope of the tempering is the transformation of the retained austenite, in ferrite, that eventually can be transformed in martensite during cooling, and fine carbide particles. This process is repeated multiple times to obtain almost complete transformation of the retained austenite. A schematization of the overall QT process is proposed in Figure 1.12.

During the heat treatment of a fully martensitic component, it does not experience homogenous temperature distribution. This can be explained by: i) if the component is bulky, there will be temperature difference on the surface and within the component. ii) the surface reaches the

heat treatment temperature faster than the center of the material. During cooling the surface of the material is cooling faster than the center, which can induce tension on the surface and compression in the center. The presence of this stresses can cause distortion of the part. Understanding the material properties and the complexity of the geometry can help to design correct heat treatment procedures.

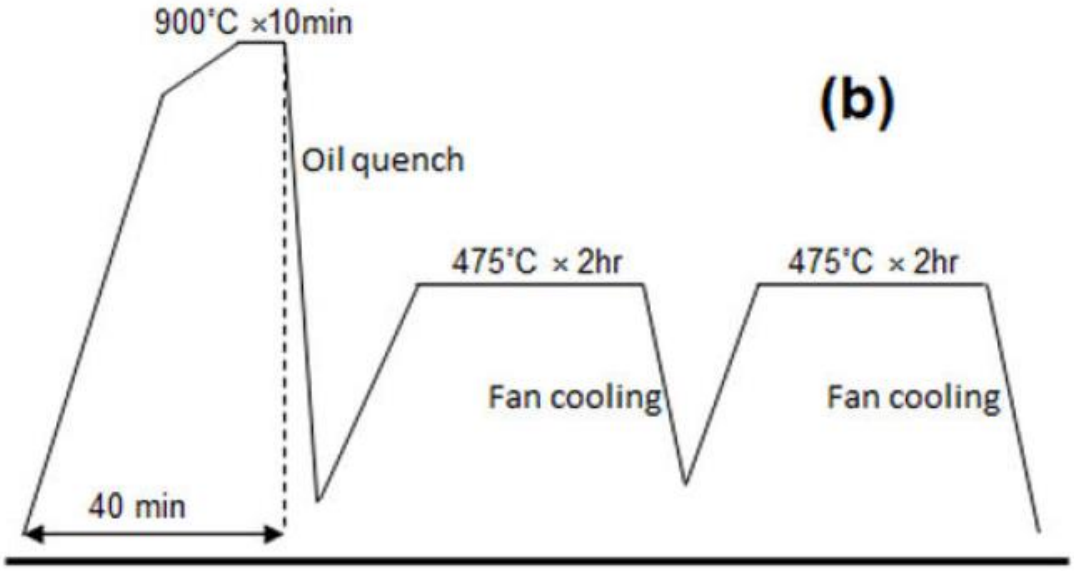

Figure 1.12 Scheme of the quenching and tempering heat treatment (Akhavan et al., 2015)

Precipitation hardened mold steel is suitable for application demanding for wear resistance due to its high hardness. This type of steels are alloyed with V, Nb and Ti (Firrao et al., 2013) to increase hardness, yield, and ultimate strength by precipitation hardening and grain refinement. In addition, the hardness homogeneity can be achieved through heat treatment.

After the process of the bloom, the mold undergoes solubilization at hypercritical or subcritical temperature, followed by ageing at subcritical temperature. Temperature and time are important parameters to obtain proper hardness and toughness. Increasing the ageing temperature and the time will lead the mechanical properties of the steel to increase before weakening due to elevated temperature. It is due to carbide coarsening enhanced by diffusion.

Firrao et al. studied the effect of precipitation hardening on the fatigue properties and fracture toughness of 1.2738 steel used for large molds. The resulting martensite is uniformly distributed with fine precipitated carbides. Furthermore the carbides precipitated during the first hardening treatment (quenching and tempering) are unstable at ageing temperature, hence their solubilization in the matrix, their place is taken by new fine carbides (Firrao et al., 2013) (Firrao et al., 2009). As shown in Figure 1.13 this heat treatment allows higher threshold values

of the stress intensity factor and lower Paris slope, that means lower tendency of crack propagation under cyclic loading. The heat treatment also increases the fracture toughness respect to the QT condition, due to the presence of homogenous tempered martensite along the bloom depth.

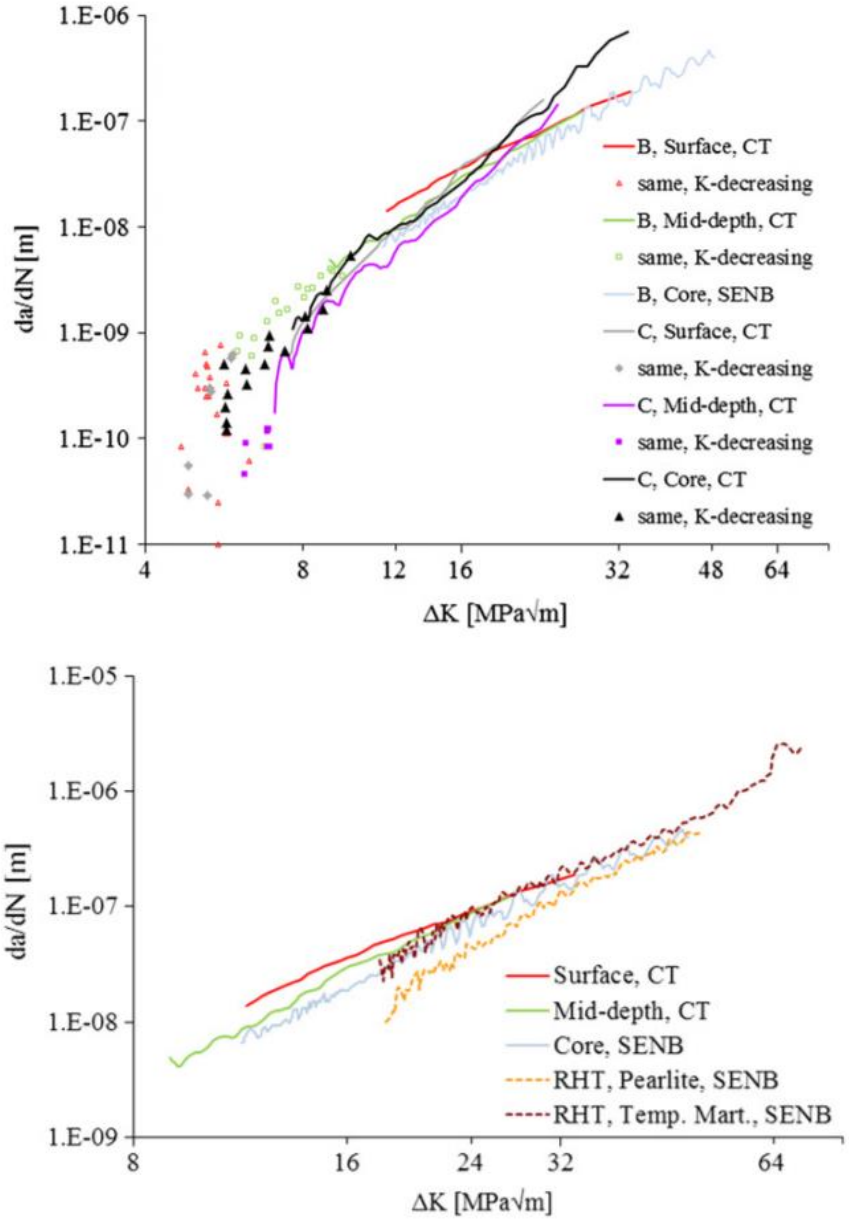

Figure 1.13 Plot of crack propagation for QT mold steel and PH steel at the bottom (Firrao et al., 2013)

1.3.3.1 Case hardening

Case hardening is a process that promotes diffusion of chemical elements through the surface of a component to achieve different specific properties (hardness, wear resistance, corrosion resistance) while the rest of material is in pre-treatment conditions. There are different types of case hardening and it can be characterized as:

- Carburizing;
- Carbonitriding;
- Nitriding;
- Nitrocarburizing;

There are different methods to promote the diffusion of carbon in the material during carburizing:

- Gas carburizing;
- Vacuum carburizing or low pressure carburizing for those case where the oxygen content needs to be low;
- Plasma carburizing;
- Salt bath carburizing: the component is placed in a salt bath with high carbon potential;
- Pack carburizing: the part is covered by solid compound with high carbon potential;

Two main factors are concerned during carburizing. The first is the austenitization of the material since the carbon has higher solubility in the austenite due to the presence of FCC lattice. The second is the CO concentration. The CO provides carbon according to the Boudouard reaction:

$$2CO \leftrightarrow CO_2 + C \tag{1}$$

It was found out that even if in the case of liquid or solid carburization, the transfer of carbon from the source to the material, occurred through the decomposition of carbonaceous substances with production of CO that reacts with Fe atoms on the surface leading to migration of carbon into the component (Lampman, 2016). In gas carburization the enriching gas is mixed with and endothermic gas (mixture of gaseous substances that favor the carburizing process) inside a furnace, between 850-950 °C to promote the austenite formation. During the process ventilation of the atmosphere is important to ensure homogenous conditions during the heat treatment. Since the CO reacts to give the reaction product, it is important to continuously keep constant the chemical potential of the CO in the gas mixture. The carbon diffuses from the surface into the material, leading to formation of a concentration gradient along the section of the component. The diffusion process can be modelled with the second Fick's law:

$$C_{x,t} = C_s[1 - \left(1 - \frac{C_i}{C_s}\right) \mathrm{erf}\frac{x}{\sqrt{D * t}}] \tag{2}$$

Where $C_{x,t}$ is the concentration in function of the depth x and time t, C_s is the concentration of carbon at the surface, C_i is the initial carbon concentration in the steel, erf is an error function,

x is the depth, D the diffusivity of C in the Fe lattice and t the time. This law describes the diffusion as function of time and depth, under the hypothesis that the concentration of carbon is kept constant at the surface, that is quite realistic since the gas is continuously maintain under monitoring. The diffusivity coefficient is function of temperature, chemical composition of the material and type of crystal lattice, increasing the temperature the energy barrier to promote interstitial diffusion is decreased, allowing higher diffusion rate. At the same time the carbon concentration in the steel is also important because the main driving force for diffusion is the concentration gradient. According to the stable phase in function of temperature the Fe atoms arrange in different crystal structures that have diverse interstitial sites, the FCC lattice, typical of austenite, allows higher solubility of carbon due to the presence of bigger sites.

The carbon content at the surface can reach 0.9 - 1.1 wt%. This lead to different consequences:

- from the metallurgical point of view, the material is influenced by the presence of a C gradient that defines different critical cooling rates and M_s temperature. During quenching, the core of the material transforms to martensite before the surface due to the lower C content (because C is an austenite stabilizer), the transformation occurs with expansion of the material below the surface. When the temperature at the surface reaches the martensite start temperature, the atoms are constrained by the layer below, thus compressive beneficial residual stresses are introduced. These residual stresses are one the advantages of the carburizing process, since they increase the strength, wear resistance and fatigue life of the component. When compressive residual stresses are introduced the loading capacity is increased. When the load is applied, it compensates the compressive residual stresses.
- The higher carbon content at the surface, enhance the presence of retained austenite after the quenching process. This can be beneficial for some application where surface toughness is requested;
- Carbides formation;
- Retained austenite can transform into untampered martensite during service life by mechanical induced transformation if shear stresses are present.

The main advantages of carburizing are the low material cost, low energy input for machining, controlling of mechanical properties, presence of compressive stresses on the surface, easiness of performing cold/hot working on mild and high carbon steel. However high capital cost, high energy consumption and presence of distortion of the component characterized this process.

In the traditional mold manufacturing wear resistance is increased through the carburizing technique, and surface nitriding is used to ensure better corrosion properties. The difference between these two methods is related to the chemical compounds formed at the surface, the chemical compounds distribution and thickness of the layer. Nitriding ensure thicker depth (depth of the modified layer) with better overall properties overall.

Conventional surface nitriding process is a diffusion process of nitrogen from a gas or liquid system to a component at a high temperature (over 550 °C). This diffusion process is accompanied by the reactions of nitrogen with the elements present in the steel. The result of these reactions is the formation of new compounds that can increase the wear and corrosion resistance. The typical nitrided surface is composed by two layers: diffusion layer and compound layer. The first layer generally contains interstitial elements and small distributed nitrides. The lattice is strengthened by the interstitial solution , thought decreased mobility of iron atoms and pinning effect of precipitates on dislocations. The second layer is composed of ε (Fe_2−3N) and γ' (Fe_4N) that are responsible for better corrosion and wear resistance (Wen, 2009b) (Boztepe et al., 2018).

Zhang Wei et al. (Zhang et al., 2011) studied the effect of laser alloying on P20 steel microstructure and mechanical properties. Their method modifies the chemical composition of the surface by addition of WC during surface melting the P20 steel. In Figure 1.14 it is shown that the hardness on the surface of the nitride P20 is comparable to the laser alloyed surface (up to 200 μm). However, the thickness of the modified surface is different with nitriding than by laser alloying. Laser alloying is a more suitable technique when deeper surface modification is required.

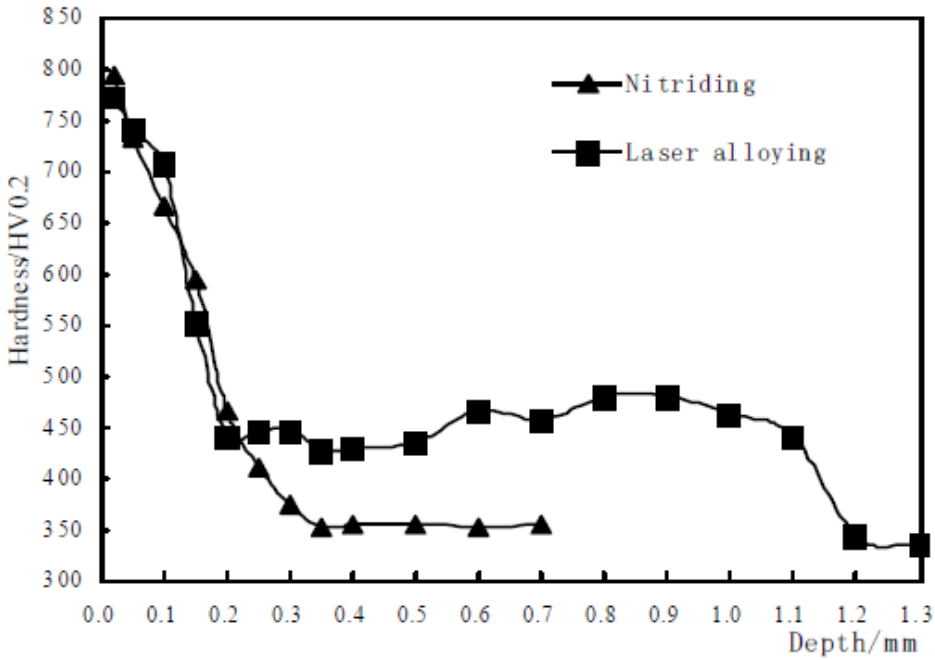

Figure 1.14 Micro hardness results along the section, for nitrided and laser cladded material (Zhang et al., 2011)

The main advantages of laser alloying over the traditional approaches (carburizing and nitriding) is that it does not depend on the original chemical composition of the mold steel. Laser cladding can be performed with automation, precision, low level of distortions (low heat input) and good metallurgical bonding with the substrate (Zhang et al., 2011).

1.4 Traditional repair techniques

Extension of the service life of molds and dies is a topic of interest for the mass production industry such as forging, stamping, casting and injection moulding(Chen et al., 2014)(Jhavar, Paul and Jain, 2013). The production cost of parts is affected by the failure of the mould/die during manufacturing, which leads to the replacement of the tool. The application of a re-manufacturing process allows 20% to 80% of cost savings (Chen et al., 2014).

(Jhavar, Paul and Jain, 2013) gives an overview on the failure mechanisms and repair techniques for mould and dies. Failure is define as deterioration of performances due to changes in shape, dimensions and material properties. Failure can be classified as: i) catastrophic, ii) manufacturing and iii) operational. Catastrophic failure is related to force majeour, improper storage, faulty design and mishandling during transportation. Operational failure occurs during post-processing such as machining or grinding, which can lead to surface damage due to the crack sensitivity of the steel. Manufacturing failures are related to the deterioration of tool performances during the service life. This can be caused by wear, corrosion, impact, plastic deformation, thermal cracking or fatigue, depending on the working conditions.

The study divides the repair process in steps:

- Damage estimation;
- Surface cleaning;
- Repair strategy selection;
- Rebuilding;
- Testing and inspection;
- Finishing process;

The damage estimation is the first step, which requires analysis of the damage type, dimension, shape and location. Surface cleaning is adopted in order to remove organic substances, oils or rust which could be present on the surface and contaminate the material. There are different types of cleaning process. They can be chemical, physical or chemical-physical processes. Machining is a commonly used process, in terms of surface quality and dimensional tolerances. In order to accomplish a successful repair, it is important to select the most suitable technique according to the type of damage. The factors taken into account are deposition rate, equipment portability, access to intricate geometries, cost, setup time and requirement of heat treatment. In Figure 1.15 these criteria are listed for different types of repair techniques. As can be seen fusion welding is the most suitable process in order to achieve high deposition rate, satisfactory

material properties and build integrity. After selection of the method, the material is deposited and the damaged area is filled back to the original dimension. The deposited material is inspected and tested to ensure performance. Finally surface finishing is required to obtain a smooth surface.

Fusion welding is commonly performed for repairing components with machining errors or damage during service life (Jhavar, Paul and Jain, 2013) . It is a suitable repair technique that allows fast material deposition and satisfactory properties. Several types of welding are available according to heat source used. Each technique has different features that make it suitable for different applications. This can be seen in Figure 1.16 which shows the common repair processes used for casting dies, forging dies, die-casting dies and plastic injection molds. It can be seen that for each case a different repair strategy can be used according to specific criteria.

According to (Silva, Pires and Quintino, 2008)(Jhavar and Paul, 2016) (Grum and Slabe, 2004) (Jhavar, Paul and Jain, 2013) (Chen et al., 2014) the commonly used welding repair techniques as follows:

- Tungsten Inert Gas (TIG);
- Plasma Arc welding (PAW)
- Laser welding;

During TIG welding, an electric arc melts the feed wire and promotes the transfer on the substrate. TIG welding is used for its easy applicability, high welding quality, good surface accuracy. On the other hand, the high heat input leads to the presence of residual stresses and distortions. Furthermore the thermal history also affects the metallurgical properties of the deposit. Laser welding is preferred when more precise weld paths are needed with lower heat affection. (Silva, Pires and Quintino, 2008) compared TIG and laser welding for repairing of plastic injections molds. The results show that the HAZ for laser welding is narrower compared to TIG welding. The lower thermal load in the case of laser welding leads to less residual stresses, distortions and no need for pre-heating. On the other hand presence of defects such as pores and lack of fusion were detected.

PAW is less common compared to the aforementioned techniques. An electric arc forms between the non-consumable electrode and the contact tip. The arc ionizes the plasma gas which is blown along the torch. The plasma is surrounded by the shielding gas. PAW can be wire or powder-fed. The main advantage of this technique is the cylindrical shape of the plasma that allows lower heat input and more controlled deposition compared to TIG welding. The cost involved in this process can be one of the major limitations (Pinkerton, Wang and Li, 2008).

Criteria	GTAW/ PTAW	Laser based deposition	Micro TIG /Plasma	EBW	Electro-spark welding	Cold spray	Thermal coatings
Rate of Deposition	●●●●○	●●●○○	●●○○○	●●●●●	●○○○○	●●○○○	●●●●●
Equipment portability	●●●●○	●●○○○	●●●●○	●○○○○	●●●●○	●●●○○	●●○○○
Access to intricate geometries	●●●●○	●●○○○	●●●●○	●○○○○	●○○○○	●○○○○	●●○○○
Cost	●○○○○	●●●●○	●●○○○	●●●○○	●○○○○	●●○○○	●●○○○
Metallurgical properties	●○○○○	●●●●○	●●●○○	●●○○○	●●●○○	●●○○○	●●○○○
Setup time	●●○○○	●●●●○	●●●○○	●○○○○	●●●○○	●●●○○	●●○○○
Requirement of heat treatment	●○○○○	●●●●○	●●●○○	●●○○○	●●●○○	●●●○○	●●○○○

High ●●●●●, Medium ●●●○○, Low ○○○○○.

Figure 1.15 Comparison of various material deposition processes (Jhavar, Paul and Jain, 2013)

	Stamping dies	Hot forging dies	Die casting dies	Injection moulds
Production quantity	High volume	High volume	High volume	High volume
Value	High	High	High	High
Evolution rate	Low	Low	Low	Medium
Mould material	Cold work	Hot work	Hot work	Hot work
Main failure modes	Wear (85%), plastic deformation	Wear (70%), thermal cracks, plastic deformation	Wear, thermal cracks (70%), soldering	Wear, thermal cracks, plastic deformation
Repair strategies	Machining	Machining	Tungsten Inert Gas (TIG) welding, laser welding, surface engineering	TIG welding, surface engineering

Figure 1.16 Main features of dies and moulds and their repair strategies(Chen et al., 2014)

These processes can be manual or automated. According to (Norrish, 2009) automated systems can be classified as:

- Simple mechanization (tractors and manipulator);
- Special purpose systems (orbital welders);
- Dedicated automation (purpose designed);
- Modular automation (component systems);
- Programmable systems (robots, CNC machines);

Automation can improve the weld quality, productivity and decrease the amount of scraps. It is favorable to implement automation when a high level of repeatability is requested. On the other hand it does not allow the same flexibility of manual welding and it also needs a high capital cost. For this reasons automation can be beneficial for repairing mold and die, where high weld quality and repeatability is requested, and at the same time high intrinsic value.

1.5 Additive Manufacturing tecniques

Metal additive manufacturing (AM) is the process of production of component layer by layer. According to (Tofail et al., 2018) AM processes can be classified in:

- Binder jetting (BJ);
- Directed energy deposition (DED);
- Material extrusion (ME);
- Material jetting (MJ);
- Powder bed fusion (PBF);
- Sheet lamination (SL);
- Vat photopolymerization (VP).

PBF and DED are the most used two class of AM processes . In the case of PBF thermal energy fuses locally the powder bed. This process is repeated layer by layer to build a solid component. According to the type of source different variants of the PBF are available. When laser is used the process is called selective laser melting (SLM), while electron beam melting (EBM) when an electron beam is utilized. In SLS and SLM the bonding thermal phenomena involved are different. In the case of SLS the powder particles are completely melted. This has an important influence on the temperature involved, material properties and presence of pores. The SLS/SLM and EBM need a protective environment, which in the case of the first can be an inert atmosphere while in the second vacuum is needed. The component is confined in a chamber, which acts as limitation for the maximum build volume. On the other hand the PBF processes have really high accuracy, resolution and material properties.

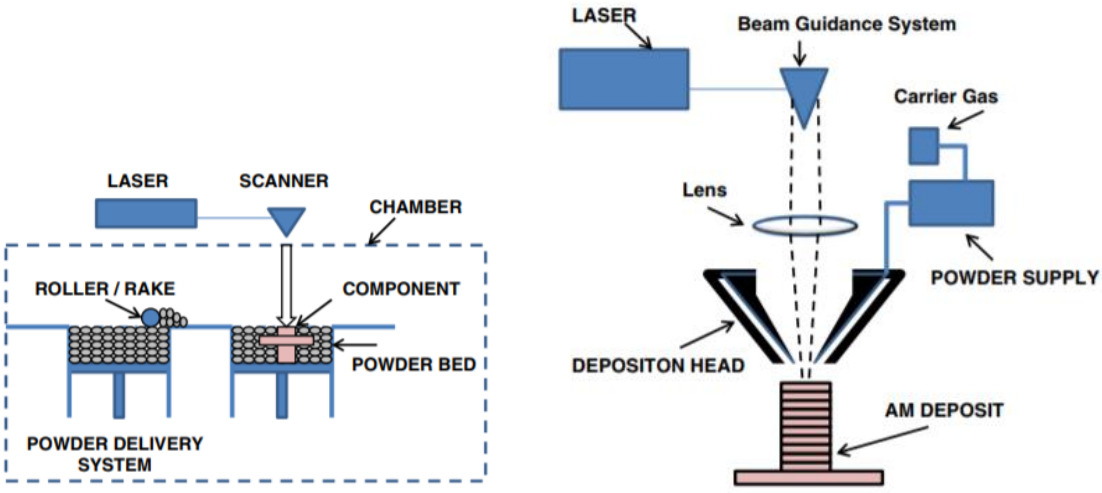

Figure 1.17 Illustration of the a) PBF process and b) DED process (Frazier, 2014)

During the DED process, thermal energy melts the material while it is deposited. The heat source can be an electron beam, a laser or a plasma arc. The DED process can be executed in open air environment or in closed chamber. The possibility to print in open air gives many advantages, such as higher build volume, higher deposition rate and no need for protective environment. The torch can also be attached to a robotic arm, this is the case of Wire Arc Additive Manufacturing. This solution has many degrees of freedom and it allows the printing of large components with shapes not possible to obtain with other techniques. On the other hand the accuracy of the DED processes is lower compared to the PBF, the heat conducted into the workpiece is higher leading to residual stresses and distortion.

The DED process can also be classified in wire feed systems and powder feed systems (Frazier, 2014). The main differences concern the quality of the deposition, cost and accuracy. The powder feed system is more costly due to the powder manufacturing. Another limitation can be the limited availability of metals compared to the wire feed system.

According to (Ngo et al., 2018) the DED process is more suitable to be used for repair application for several reasons:

- No size limitation;
- Fast deposition;
- Availability of wide range of alloy;
- Reduce of manufacturing cost and time;

Some disadvantages of the DED process can be the amount of residual stresses and distortions, low level of accuracy, low surface quality and limitation in complexity.

It is important to note that in literature when talking about DED process it refers to the powder feed system, which is much more established and studied technique. This technology is also

called LENS. In the next paragraph a presentation of the Wire Arc Additive Manufacturing (WAAM) process is proposed.

1.6 Wire Arc Additive Manufacturing

When an electric arc is coupled to a robotic arm, the welding process refers to Wire Arc Additive Manufacturing (WAAM) firstly patent by 1925 and better studied in the latest 90's. In the specific case of this study a MIG torch is attached to a robotic arm, where the wire is fed. The process consist of layer by layer deposition of overlapped welding beads to recreate the feature extent of the part. This process is particularly suitable for AM of large-scale components, thanks to high deposition rate, availability of different types of alloys and relative low capital cost (Williams et al., 2017). The main process parameters are current, voltage and torch speed, even though the variables that play an important role in the process are numerous: current, voltage, speed, shielding gas, cooling rate, stick out and complexity of the part. The disadvantages of the process are the presence of residual stresses, distortion, need of final machining to reach the final shape of the component, presence of porosity and part orientation.

During the deposition the consumable electrode is melted and deposited on the substrate, the rapid cooling rate (1000 °C/s) leads to solidification and non-equilibrium phase transformation of the phases. The heat is conducted from the bead to the neighboring material, inducing thermal cycles. The heat affection of the material has an important influence on the final microstructure and properties. The heat input is controlled by current, voltage and torch speed, that matches with the desired process parameter. The compromise between deposition rate and material properties does not always match, since most of the times higher heat input is needed, with bad effects on the microstructure.

The typical microstructure consists of columnar grains growing upwards from the solidification line, that follow the heat conduction. The deposition of each bead promotes treatment of part of the previous bead, that can be divided in: coarse grain heat affected zone (CGHAZ), fine grain heat affected zone (FGHAZ), tempered zone, unaffected zone. The CGHAZ is close to the fusion line, leading to presence of higher temperature. This promotes the formation of new grains and their coarsening. From the mechanical point of view this region has lower hardness. The FGHAZ is made of small grain, due to the fact that the heat is not high enough to let them growth but only capable to induce formation of new fine grains, this area present higher hardness. Following the HAZ the tempered zone is present, in this area the material is heated up to lower temperature, carbon diffusion, stress relief and precipitation of carbides are possible, with changes in the material properties. In the unaffected zone the material is not subjected to metallurgical modifications.

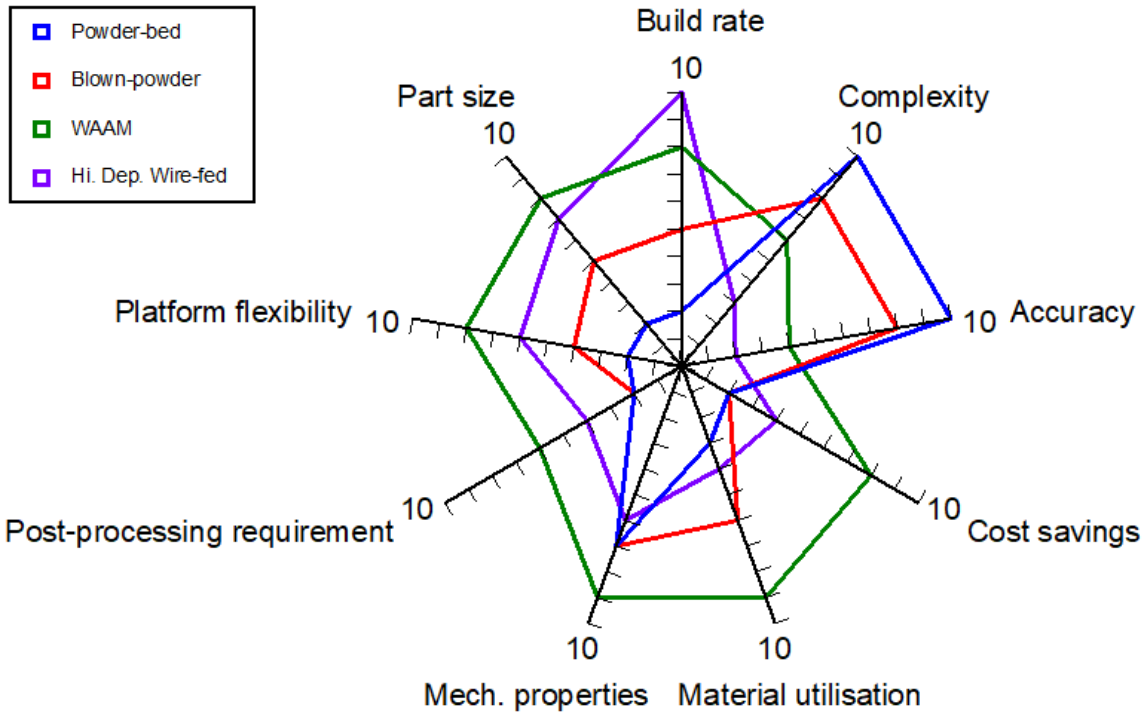

Figure 1.18 Benefits and limitation of different AM processes (Martina and Williams, 2015)

In Figure 1.18 a comparison of different AM processes is proposed. WAAM is advantageous when large-dimension components are needed. Compared to the other AM techniques WAAM gives also benefits in cost and material utilization. The platform used for the printing has high degree of freedom, and this is why it is considered as one of the more flexible techniques available. On the other hand, when talking about accuracy and complexity WAAM loses some points, due to the nature of the process. Post processing isalso required for heat treatment and also surface finishing. All these features must be considered in the case of repair. There is not a single solution which can be suitable for all the component. Thus each case should be analyzed to understand whereas AM can be applied for repairing and which of the AM process must be chosen.

Bibliography

Akhavan, M. *et al.* (2015) 'The influence of heat treatment on the microstructure and machinability of a prehardened mold steel', pp. 1007–1014.

ALMEIDA, P. M. S. (2012) 'Process Control and Development in Wire and Arc Additive Manufacturing', (April), pp. 1–467.

Archard, J. F. (1953) 'Contact and rubbing of flat surfaces', *Journal of Applied Physics*, 24(8), pp. 981–988. doi: 10.1063/1.1721448.

Bergstrom, J. *et al.* (2001) 'Wear of die materials in full scale plastic injection moulding of glass fibre reinforced polycarbonate', *Wear*. doi: 10.1016/S0043-1648(01)00787-6.

Boztepe, E. *et al.* (2018) 'A comparative investigation of the corrosion and tribocorrosion behaviour of nitrocarburized, gas nitrided, fluidized-bed nitrided, and plasma nitrided plastic mould steel', *Surface and Coatings Technology*. Elsevier, 334(October 2017), pp. 116–123. doi: 10.1016/j.surfcoat.2017.11.033.

Charter, M. and Gray, C. (2008) 'Remanufacturing and product design', *International Journal of Product Development*, 6(3/4), p. 375. doi: 10.1504/IJPD.2008.020406.

Chen, C. *et al.* (2014) 'A review on remanufacture of dies and moulds', *Journal of Cleaner Production*. Elsevier Ltd, 64, pp. 13–23. doi: 10.1016/j.jclepro.2013.09.014.

Chen, J., Xue and Lijue (2002) 'Microstructural Characteristics of Laser-Clad AISI P20 Tool Steel', *Surface Engineering Coatings and Heat Treatments*, (October 2002), pp. 198–205.

Firrao, D. *et al.* (2009) 'Effect of the heat treatment on the mechanical properties of a precipitation hardening steel for large plastic molds', *Metallurgia Italiana*, 101(4), pp. 1–10.

Firrao, D. *et al.* (2013) 'Influence of the microstructure on fatigue and fracture toughness properties of large heat-treated mold steels', *Materials Science and Engineering A*. Elsevier, 559, pp. 371–383. doi: 10.1016/j.msea.2012.08.113.

Frazier, W. E. (2014) 'Metal additive manufacturing: A review', *Journal of Materials Engineering and Performance*, 23(6), pp. 1917–1928. doi: 10.1007/s11665-014-0958-z.

Gahr, K.-H. Zum (1987) *Microstructure and wear of materials*. doi: 10.1016/S0898-6568(97)00193-9.

Grum, J. and Slabe, J. M. (2004) 'Possibility of introducing laser surfacing into maintenance service of die-casting dies', 181, pp. 596–602. doi: 10.1016/j.surfcoat.2003.10.101.

He, B. (2011) 'Reseach on the failure and material selection of plastic mold', *Procedia*

Engineering, 23, pp. 46–52. doi: 10.1016/j.proeng.2011.11.2463.

Jhavar, S. and Paul, C. P. (2016) 'Micro-Plasma Transferred Arc Additive Manufacturing for Die and Mold Surface Remanufacturing', 68(7), pp. 1801–1809. doi: 10.1007/s11837-016-1932-z.

Jhavar, S., Paul, C. P. and Jain, N. K. (2013) 'Causes of failure and repairing options for dies and molds: A review', *Engineering Failure Analysis*. Elsevier Ltd, 34, pp. 519–535. doi: 10.1016/j.engfailanal.2013.09.006.

Kato, K. (2002) *Classification of wear mechanisms and models*.

Lampman, S. (2016) 'ASM Handbook, Volume 04 - Heat Treating', *ASM International*, 4(17), pp. 259–267. doi: 10.1361/asmhba000.

Leino, M., Pekkarinen, J. and Soukka, R. (2016) 'The role of laser additive manufacturing methods of metals in repair, refurbishment and remanufacturing - Enabling circular economy', *Physics Procedia*, 83, pp. 752–760. doi: 10.1016/j.phpro.2016.08.077.

Lopes, H. S. M. *et al.* (2016) 'Micro Abrasive Wear Behaviour Study of Carburization and Ion Plasma Nitriding of P20 Steel', *Materials Research*, 19(3), pp. 686–694. doi: 10.1590/1980-5373-MR-2015-0721.

Lund, R. T. (1981) *Remanufacturing: The Experience of the United States and Implications for Developing Countries*.

Lund, R. T. and Hauser, W. M. (2010) 'Remanufacturing - An American Perspective', *Green Manufacturing*.

Luo, Y. *et al.* (2009) 'A comparative study on non-quenched and quenched prehardened steel for large section plastic mould', *Journal of Materials Processing Technology*, 209(14), pp. 5437–5442. doi: 10.1016/j.jmatprotec.2009.04.019.

Martina, F. and Williams, S. (2015) 'Wire+arc additive manufacturing vs. traditional machining from solid: a cost comparison', p. 27.

Martínez-Mateo, I. *et al.* (2011) 'Surface damage of mold steel and its influence on surface roughness of injection molded plastic parts', *Wear*, 271(9–10), pp. 2512–2516. doi: 10.1016/j.wear.2010.11.054.

May, N. (2016) 'The Properties of Random Surfaces of Significance in their Contact', 229(1178), pp. 281–316.

Ngo, T. D. *et al.* (2018) 'Additive manufacturing (3D printing): A review of materials , methods , applications and challenges', *Composites Part B*. Elsevier, 143(February), pp. 172–196. doi: 10.1016/j.compositesb.2018.02.012.

Norrish, J. (2009) 'Process control and automation developments in welding', *ASM Proceedings of the International Conference: Trends in Welding Research*, pp. 17–24. doi: 10.1361/cp2008twr017.

Pinkerton, A. J., Wang, W. and Li, L. (2008) 'Component repair using laser direct metal deposition', 222(September 2007), pp. 827–836. doi: 10.1243/09544054JEM1008.

Preciado, W. T. and Bohorquez, C. E. N. (2006) 'Repair welding of polymer injection molds manufactured in AISI P20 and VP50IM steels', *Journal of Materials Processing Technology*, 179(1–3), pp. 244–250. doi: 10.1016/j.jmatprotec.2006.03.101.

Roberts, G., Krauss, G. and Kennedy, R. (1998) 'Tool Steels', *ASM International*, p. 121. doi: 10.1361/t.

Sikorski, M. E. (1964) 'The adhesion of metals and factors that influence it', *Wear*, 7, pp. 144–162.

Silva, B., Pires, I. and Quintino, L. (2008) 'Welding Technologies For Repairing Plastic Injection Moulds', *Material Science Forum*, pp. 936–940.

Silva, F. J. G. *et al.* (2011) 'Increasing the wear resistance of molds for injection of glass fiber reinforced plastics', *Wear*. Elsevier B.V., 271(9–10), pp. 2494–2499. doi: 10.1016/j.wear.2011.01.074.

Stormvinter, A., Hedström, P. and Borgenstam, A. (2011) 'Investigation of Lath and Plate Martensite in a Carbon Steel', 174, pp. 61–66. doi: 10.4028/www.scientific.net/SSP.172-174.61.

Tofail, S. A. M. *et al.* (2018) 'Additive manufacturing : scientific and technological challenges , market uptake and opportunities', *Materials Today*, 21(1), pp. 22–37. doi: 10.1016/j.mattod.2017.07.001.

Wen, D. C. (2009a) 'Erosion-corrosion behavior of plastic mold steel in solid/aqueous slurry', *Journal of Materials Science*, 44(23), pp. 6363–6371. doi: 10.1007/s10853-009-3877-x.

Wen, D. C. (2009b) 'Plasma nitriding of plastic mold steel to increase wear- and corrosion properties', *Surface and Coatings Technology*. Elsevier B.V., 204(4), pp. 511–519. doi: 10.1016/j.surfcoat.2009.08.023.

Williams, S. W. *et al.* (2017) 'Wire + Arc Additive Manufacturing Wire þ Arc Additive Manufacturing', (December), pp. 1–35. doi: 10.1179/1743284715Y.0000000073doi.org/10.1179/1743284715Y.0000000073.

Zhang, M. *et al.* (2010) 'The discussion of the principle and application about remanufacturing of covered mold welding', *2010 International Conference on Mechanic Automation and Control*

Engineering, MACE2010, (figure 1), pp. 3868–3870. doi: 10.1109/MACE.2010.5536522.

Zhang, W. *et al.* (2011) 'Research of microstructure and property of laser alloying on the surface of P20 steel compared with nitriding', *Advanced Materials Research*, 217–218, pp. 1629–1632. doi: 10.4028/www.scientific.net/AMR.217-218.1629.

2 Microstructure evolution of P20 steel during WAAM

2.1 Literature review

2.1.1 Single Bead Deposition

A single bead-on-plate welding is the starting point to investigate the material behavior during the WAAM process. Different features have to be studied in order to ensure optimal conditions during welding, they can be divided in quantitative and qualitative features. The first are related with height and width of the bead, the second with quality of the surface, arc stability, presence of silicates and spatter. The control of the process parameters, such as voltage (V), current (I) and torch speed (S), is fundamental in order to ensure best results from quantitative and qualitative point of view. Besides process parameters, gas composition, gas flow rate and preheating temperature are important in the quality of the build. The composition of the gas mixture is related with the stability of the arc, porosity, depth of penetration, spatter and cooling of the melt pool. The gas flow rate contribute to the protection of the melt metal, thus enough flow has to be present to have the best quality of the bead.

The pre-heating temperature is important for reduction of residual stresses and distortions (Ding et al., 2015) hot cracking and hydrogen cracking. Porosity can be reduced if the component is kept at a minimum background temperature during the deposition.

Donghong et al. (Ding et al., 2015a) proposed a model to predict the shape of the bead in function of the process parameters. There are mainly three different types of model to describe the shape of the single bead: parabola model, cosine model and arc model. The mathematical expression of the three model is function of model parameters, that are calculated experimentally.

Models	Model function
Parabola model	$y = ax^2 + c$
Cosine model	$y = a\ \cos(bx)$
Arc model	$y = \sqrt{a^2 - x^2} + b$

Figure 2.1 Mathematical expression of the parabola model, cosine model and arc model (Ding et al., 2015a)

2.1.1.1 Microstructure evolution during welding

The microstructure evolution during welding represents an important topic to evaluate the final properties of the deposited material. To understand the development of microstructure during WAAM is important to define the base theory of microstructure evolution during simple MIG/MAG welding. In a welded metal the microstructure can be divided in three main types: primary, secondary and tertiary structure.

The primary structure is the result of the solidification of the deposited material, that reminds to the casting microstructure. The morphology of grains is related to the maximum heat extraction

direction that is perpendicular to the solid/liquid interface and to the preferential growth direction (direction where the energy barrier for grain growth is minimal). This two solidification conditions determine the structure of the grains that grow from the fusion line to the centerline of the melt pool, where the boundary condition can vary substantially.

The two main solidification parameters are the temperature gradient G and the growth rate R. The temperature gradient is function of the heat input applied, defined as:

$$HI = \frac{\eta * VI}{S} \tag{2.1}$$

Where η is an efficiency term that takes into account the heat losses during welding, V is the voltage, I the current and S is the heat source speed. The growth rate G is function of the speed of the heat source and the shape of the melt pool. In particular, during welding the shape of the melt pool can be modified changing the speed of the heat source, the two main types of shape are elliptical and tear-drop melt pool (Figure 2.2). At low or moderate heat source speed the melt pool shape results in an elliptical shape, where grains grow from the fusion line to the centerline. Due to the motion of the solid/liquid interface and the fact that it's shape is curved, the preferable growth direction can become un-favorable, and new grains can grow. In the case of higher heat source speed the shape of the melt pool becomes elongated to form a tear drop tail. The reason is related to the fact that the grain growth is higher when the speed of the heat source is increased, and the same time also the release heat latent is high. The gradient at the centerline are low, avoiding extraction of heat, causing the presence of melt metal at the tip. The fact that the melt pool is elongated causes the presence of a flat solid/liquid interface that helps the grains to grow in their preferential direction.

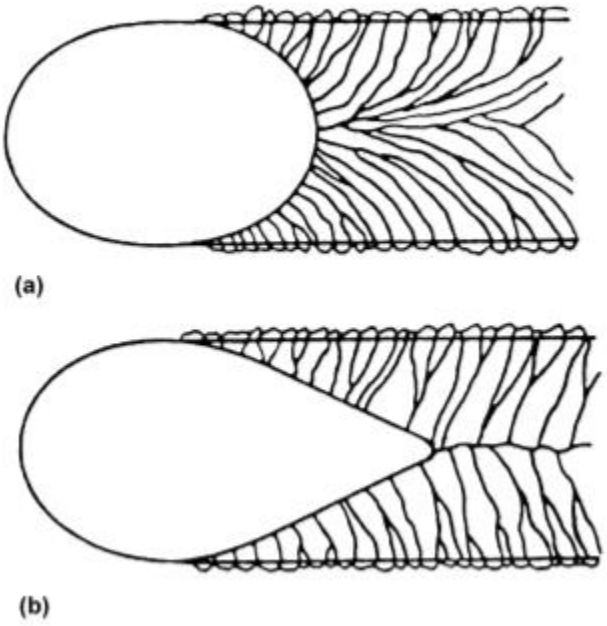

Figure 2.2 Type of melt pool shape: a) elliptical and b) tear drop shape (Solomon, 1993)

At the fusion, the temperature gradients are the steepest, since the material is in contact with the colder metal, and the growth rate is minimum. In the centerline the gradient are the lowest due to the lower heat extraction, and at the same time the growth rate is the highest. This difference leads to special diversification of the microstructure in melt pool.

The secondary microstructure depends on the segregation of alloying elements at the solid/liquid interface. Following the solidification in the equilibrium phase diagram the liquid is enriched in solute. During welding, non-equilibrium must be taken into account, since rapid growth rate and large thermal gradients are involved. Thus, the solute rejected into the liquid cannot be transported efficiently, leading to an accumulation of solute close to the interface and a concentration gradient in the liquid. In Figure 2.3 a) the solidus and liquidus on the equilibrium condition is proposed. The solute distribution when non-equilibrium conditions are considered is shown in Figure 2.3 b). The change in composition along the distance from the interface creates also a liquidus temperature distribution (Figure 2.3c), that has importance in the evaluation of the development of the secondary structure.

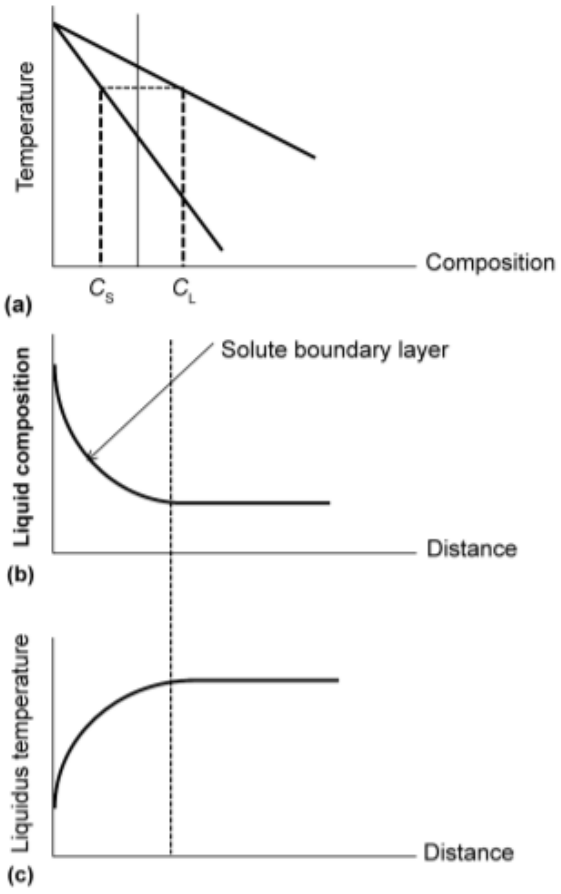

Figure 2.3 a) Solidus and liquidus curves in general phase diagram, b) solute distribution in the liquid and c) liquidus temperature distribution in the liquid (Solomon, 1993)

Assuming a linear solute gradient in the liquid, the mass balance of the solute segregation from the solid to the liquid is given by:

$$R(C_L - C_0) = D_L \frac{dC_L}{dx} \tag{2.2}$$

Where C_L is the liquid composition at solid/liquid interface, C_0 is the nominal alloy composition and D_L is the diffusivity coefficient of the solute in the liquid. Assuming a linear liquidus line in the phase diagram at steady-state, the solute gradient induces a temperature gradient given by:

$$\frac{dT_L}{dx} = m_L \frac{dC_L}{dx} \tag{2.3}$$

where $\frac{dT_L}{dx}$ is the change in liquidus temperature and m_L is the slope of the liquidus line. Rearranging equation 2.2 and substituting $\frac{dC_L}{dx}$ in equation 2.3, the following equation is obtained:

$$\frac{dT_L}{dx} = \frac{m_L R(C_L - C_0)}{D_L} \tag{2.4}$$

If T_a is the actual temperature of the liquid, the condition to have constitutional supercooling is given by:

$$\frac{dT_a}{dx} < \frac{dT_L}{dx} = \frac{m_L R(C_L - C_0)}{D_L} \tag{2.5}$$

The term $\frac{dT_a}{dx}$ is known as G (already mentioned in the previously), it represent the real temperature gradient in the liquid. The concentration of liquid at the interface (C_L) can be expressed as $C_L = C_0/k$, where k is the distribution coefficient (also called segregation coefficient), defined as $k = C_s/C_L$, where C_s is the concentration of the solute in the solid.

The expression for the constitutional supercooling can be given by:

$$\frac{G}{R} < \frac{m_L(C_L - C_0)}{kD_L} \tag{2.6}$$

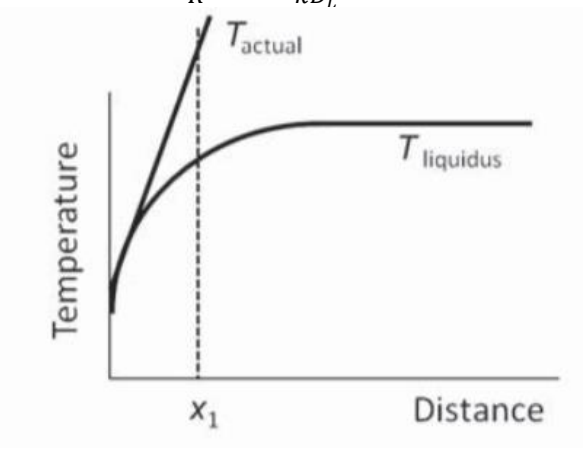

Figure 2.4 Temperature distribution in the liquid with breakdown of the planar interface growth occurs (Solomon, 1993)

The ratio $\frac{G}{R}$ determines the type of microstructure that evolves during the solidification when breakdown of the planar interface growth occurs. In general, at low undercoolings, expression 2.6

refers to formation of cellular dendrites. When the planar region surface between cellular dendrites experiences higher undercooling columnar dendrites can form. Further undercooling lead to a decrease of the temperature of the liquid ahead of the tip of the dendrites, allowing solidification of equiaxed dendrites. The effect of G and R on the microstructure obtained during solidification is presented in Figure 6:

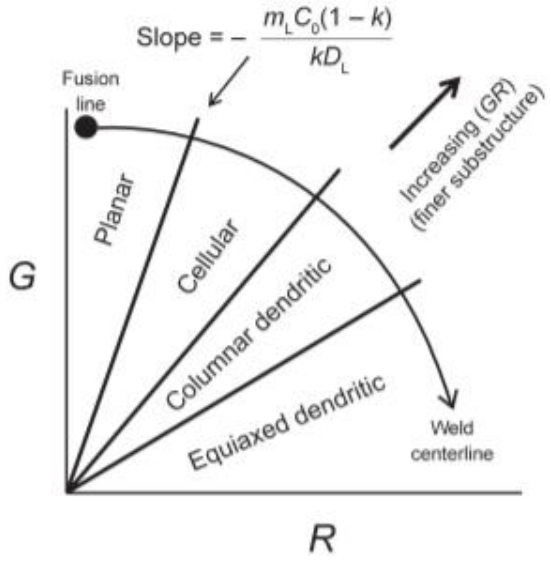

Figure 2.5 Effect of G and R on the microstructure evolution during solidification under supercooling condition (Solomon, 1993)

The formation of the tertiary microstructure is caused by the effect of the heat flux diffusing through the already deposited beads during the printing. This causes the creation of the Heat Affected Zone (HAZ).

In the HAZ different zone can be recognized:

- Corse Grain Heat Affected Zone (CGHAZ), characterized by coarse grains, which are recrystallized and grown;
- Fine Grain Heat Affected Zone (FGHAZ), characterized by fine grains. The conducted heat is no enough to promote the grain growth, but it favors only recrystallization;

Below the heat affected zone the material is subjected to thermal treatment below the recrystallization temperature, phenomena such as diffusion, carbide precipitation, annealing and tempering can take place, according to the type of material and chemical composition. It is important to have in mind that the time in this case has not to be considered as conventional heat treatment. The peak temperature is only reached for few seconds, followed by rapid cooling.

2.1.1.2 Temperature distribution

The heat conduction problem during welding has been resolved in the 1935 by Rosenthal (Rosenthal, 2017) . The description of the 3D temperature distribution is given by equation 2.7:

$$T = T_0 + \frac{H}{2\pi kR} e^{-\frac{s(\xi+R)}{2a}} \quad (2.7)$$

Where T_0 is the starting temperature, H is the heat input, k is the thermal conductivity, s is the speed of the heat source, ξ is the distance in the relative coordinate system of the heat source ($\xi = x - vt$), R ($\sqrt{\xi^2 + y^2 + z^2}$) is the distance from the heat source and a the thermal diffusivity defined as $k/\rho c_p$.

In this model several assumption are taken:

- Heat source is a point source;
- Material properties are not temperature dependent;
- The solid is semi-infinite (applicable for thick walls);
- The net heat input into the weld is $H = \eta VI/s$;

The main limitations of this model are:

- Temperature goes to infinite at the heat source;
- Phase transformation are not taken into account;
- Not applicable for all the geometry;

Improvements have been achieved with the double gaussian heat source (Goldak, Chakravarti and Bibby, 1984). This model considers a volumetric heat source which offers better prediction of the temperature distribution during welding.

2.1.2 Multi-bead deposition

During WAAM, several beads are deposited one next to the other in each layer. To ensure good surface accuracy, flat surface and avoid presence of gap, the distance between the center of two neighboring beads is crucial. Different model are available to predict which is the critical distance that ensure optimal overlap, the most used are the flat/top overlapping model (FOM) and the tangential overlapping model (TOM) (Ding et al., 2015a) . The first is based on the assumption that two areas can be identified when two beads are overlapped: the area of valley and the overlapped area, both of are depicted in Figure 2.6. This model states that a flat surface is obtained when the area of valley equals the overlapping area. Experimental studies have demonstrated that is impossible to achieve a flat surface, thus the FOM model is not adapt to predict the overlapping of two bead.

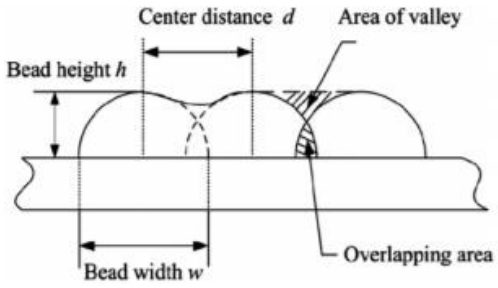

Figure 2.6 Scheme of overlapped beads, according to the FOM model (Ding et al., 2015a)

The TOM model considered the beads as parabolic curves. This approach defines a different valley area S_{BEC}, as shown in Figure 2.7. The valley area is defined as the area confined between point E (interception of the two beads) and line BC. Point B is the point on the surface of the Bead 1 which shares the same abscissa of point A. While line BC is tangential to Bead 2. The overlapping area S_{AED} is defined are before. The distance between the center of the beads is d. When the valley area and the overlapping area are equal the distance d is equal to the critical distance d^*. The value of this distance is given by:

$$d = 0.738w \tag{2.8}$$

Where d is the overlapping distance and w is the bead width.

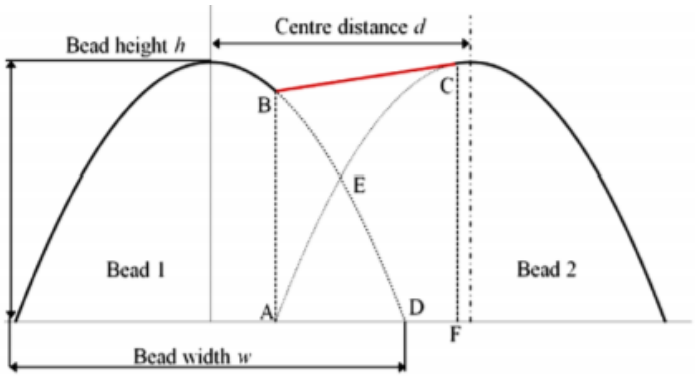

Figure 2.7 Scheme of the TOM model (Ding et al., 2015a)

When multiple beads are deposited also the step-up, defined as the vertical distance between two subsequent layers, is fundamental. In principle the distance should be the height of the bead. During deposition the bead geometry and shape can change. Several reason are addressed:

- Temperature modifies the bead geometry and favors molten metal flow;
- Non-flat surface affects the building-up;
- Small errors from measurement can accumulate and become macroscopic when more layers are printed;

This change in bead geometry/shape causes modification in the wire to substrate distance, with alteration of the process parameters. The error of the step-up height can be estimated as follow:

$$\Delta h = \frac{(n * h_b - h)}{n} = h_b - \frac{h}{n} \tag{2.9}$$

Where n is the number of layers, h_b is the height of the single bead, h is the real height of the printed part. By subtracting Δh to the bead height it is possible to obtain the correct step-up distance.

2.1.2.1 Thermal cycle

During WAAM the repeated material deposition induces heat cycles. Temperature distribution has an effect on phase transformation, microstructure, material properties, residual stresses and distortion. Thus is an important topic which is widely discussed in literature (Graf et al., 2018) (Hu, Qin and Shao, 2017)

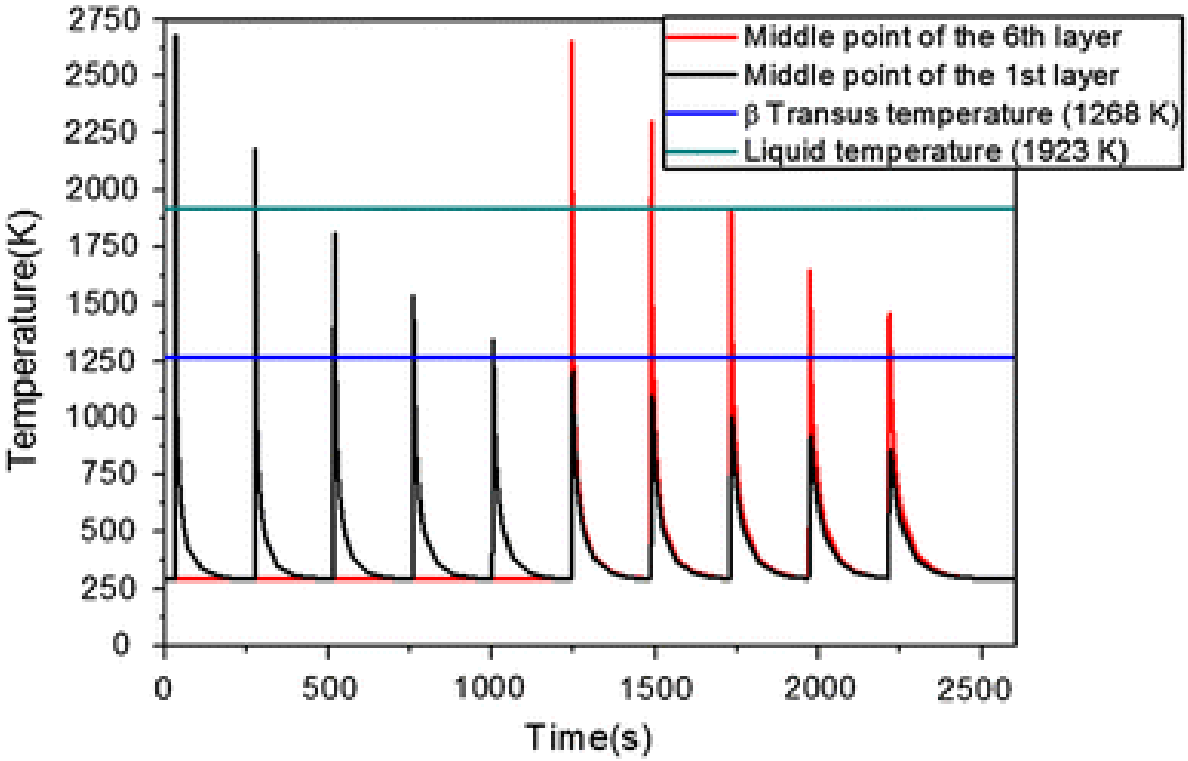

Figure 2.8 Thermal cycle during WAAM (Wang et al., 2013)

In Figure 2.8 an example of thermal cycle during printing of Ti-6Al-4V is proposed. The black and red line represent two different position in the material: 1st and 6th layers respectively. The material is heated up several time above the melting temperature and further reheating above solid state transformation temperature.

2.1.2.2 Microstructure evolution during WAAM

During WAAM multiple weld beads are superimposed. Each of them is subjected to several thermal cycles, which modify the as-deposited microstructure. Understanding the effect of the thermal cycles on the microstructure and the resulting bead geometry is far from straight-forward. Each cycle is unique, since each individual cycle depends on the process parameters and the process execution planning.

The process planning considers the toolpath design and their sequences during the deposition. The toolpath design involved toolpath length, shape and inter-pass time. The sequence of the toolpaths is more related to the area that will be subjected to the deposition. This is important for the minimization of residual stress and geometrical distortions (Ding et al., 2015c)

In the description of the thermal cycle during WAAM the following process features has to be taken into account:

- Heat Input: is the actual power per unit of length that is actually used to produce the weld. The efficiency term takes into account how much power is transferred to weld, and how much is consumed by the electric arc;
- Torch Speed: is the velocity of the heat source;
- Length and shape of the toolpath: the length of the toolpath influences the location where the heat is transferred. Also the shape of the toolpath affects the heat transfer during deposition. A detailed description is proposed in the next section;
- Air cuts: they represent the path, which the robot will follow when the deposition is not taking place. Their importance is linked with the safety distance from the product, in order to avoid collision of the torch, but they also affect the cooling of the workpiece. This is because air cuts require time, at which the component is cooling. Thus, planning the air cuts is crucial to determine a precise interpass temperature between subsequent deposition, avoid over-heating of the metal and ensure a minimum background temperature that is always beneficial for the welding;
- Delay: it is the actual delay time before the deposition of the following layer.

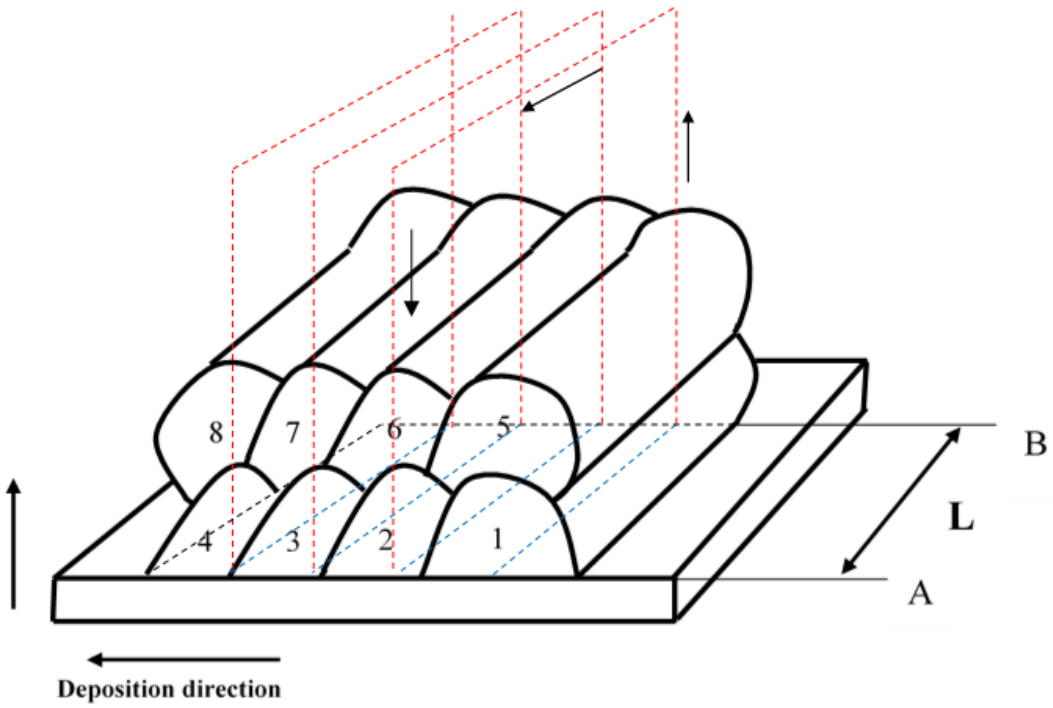

Figure 2.9 Scheme of a double layer wall deposited with WAAM

In Figure 2.9 a simple two-layer wall is presented. During the deposition of bead 1, the metal is transferred from the consumable wire to the base plate. Melting and rapid solidification lead to formation of the primary and secondary structure already described in the previous section. The typical microstructure is characterized by columnar grains that follow the maximum heat extraction direction. The torch moves from the point A towards point B along the welding line represented by a blue dashed segment. Afterwards the torch follows the air cut path from point 1B to the point 2A. During the time that the torch moves towards the point 2A, the bead 1 cools down (in reality the point 1A has already started to cool down during the deposition of the bead 1, leading to the presence of a thermal gradient along the length of the bead). The actual time that the torch requires to reach point 2B will determine the interpass temperature between subsequent depositions. This temperature is really important for possible solid-state transformation, mechanical properties, residual stresses and distortions. Once point 2A is reached, the process restart. While bead 2 is deposited, bead 1 experience partial re-melting and thermal treatment, that leads to the creation of the heat affected zone (HAZ). During the deposition of bead 3 and 4, bead 1 continues to experience thermal cycles, which decrease in peak temperature. The amount of cycles are function of the number of beads that has been deposited in the proximity of the first one (on the top but also sideways).

Once the deposition of the first layer is finished, before starting with deposition of the second layer (bead 5, 6, 7 and 8) a delay time is imposed in order to let the material to cool down. The inter-pass time is correlated with the interpass temperature, function of the material, process and desired

final properties of the component. During the printing of the second layer, each bead below the deposited one is subjected to partial re-melting and formation of HAZ (has previously described for the deposition of bead 2). The effect of the thermal cycle related with the second layer, is a modification in the microstructure and HAZ formed during the deposition of the first layer, with creation of a new one. In the practice of WAAM this phenomenon is repeated an amount of time equal to the number of layers that are printed.

Figure 2.10 is representative of the thermal cycle during the deposition of layer 1. The measured temperature refers to the side surface of bead 1. Even though it does not give the peak temperature in the material, it is useful for a better understanding of the microstructure evolution. From the analysis of the thermal cycle the following observations can be done:

- The thermal cycle can be divided in two regions: solid state transformation region and tempering region;
- The temperature distribution on the surface can be useful to understand the temperature cycle but it does not give direct information on the core regions. This means that partial solid phase transformation can occurs in the inner regions;
- The as-deposited microstructure is the result of the overall process;

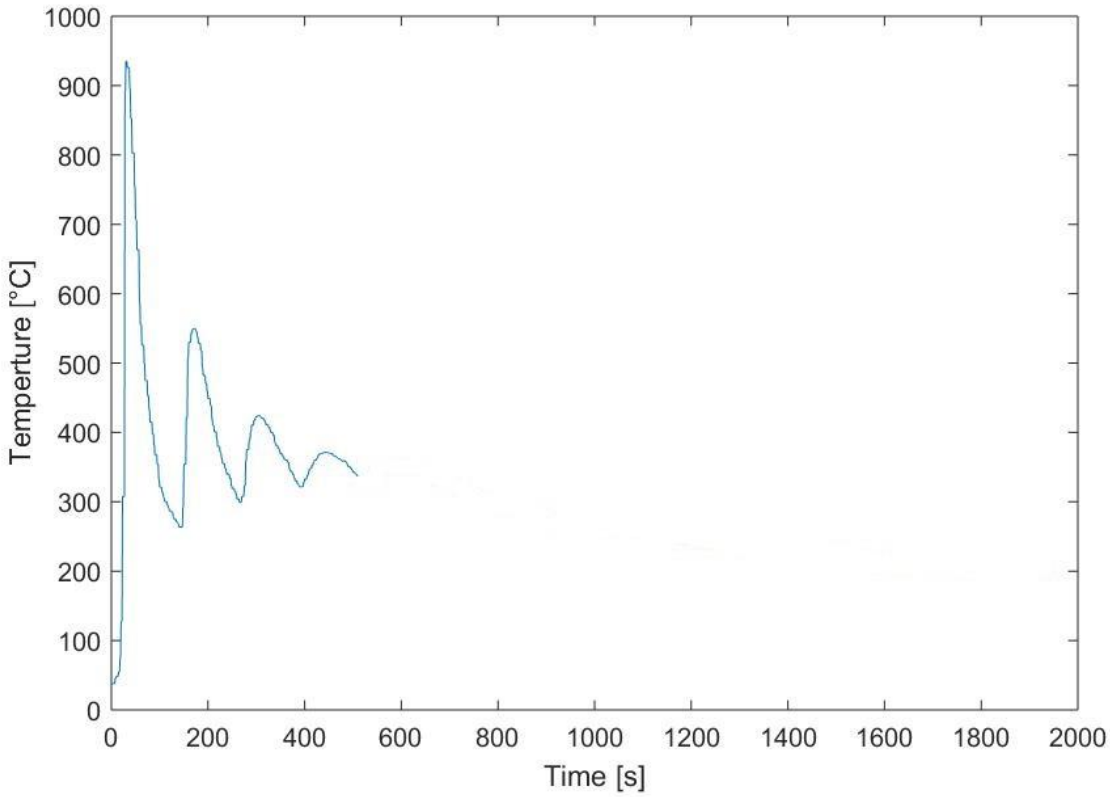

Figure 2.10 Example of thermal cycle experienced by the bead 1 during the printing of 1 layer made of 5 beads

2.1.2.3 Toolpath planning

As mentioned in the previous sections, toolpath planning is fundamental for the resulting materials properties, accuracy of the workpiece, residual stresses and distortions. Currently many groups are studying the effect of toolpath on the deposition of the component. (Ding et al., 2015b) gives a general description of the state of the art about toolpath planning. In Figure 2.11 the main used toolpaths are proposed. Raster is the simplest type of toolpath, the main features is the presence of parallel lines. This strategy is used for simple geometry where low accuracy is needed. The main disadvantage is the presence of many starts and stops, always not likely to be present. An improvement of the raster is the zig-zag deposition (Figure 2.11 b). The process results in lower time and less start/stops, leading to continuous deposition. The main concern regards the low accuracy of the strategy when curved profiles are requested.

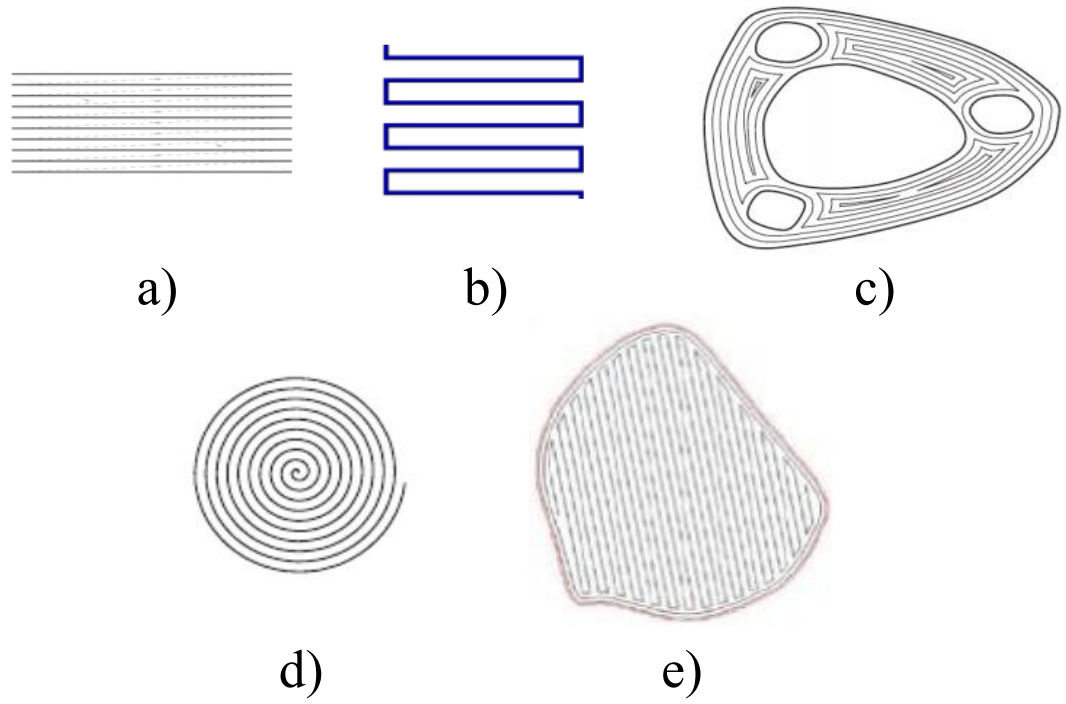

Figure 2.11 different types of toolpath: a) raster, b) zig-zag, c) contour, d) spiral, e) hybrid (Ding et al., 2015b)

This has been resolved with the introduction of the contour strategy (Figure 2.11c)), that simply offsets the contour of the component from outside to inside or vice versa. This offers the possibility to have higher accuracy on the final geometry. Also the spiral in Figure 2.11d has been widely used for specific shapes.

High attentions has been focused on the hybrid toolpath, this strategy combine the possibility to fill the internal part of the component with zig-zag toolpath and the outside with contour. The main

advantage is related with the high deposition rate and small number of starts/stops of the zig-zag and the high level of accuracy that is possible to reach with contour toolpath.

Besides the importance of shape accuracy, toolpath are also related with the effect of the heat flow on the final material properties. Thus during the deposition the heat should be spread homogeneously in the workpiece and the accumulation of the heat in a narrow zone should be avoided. Since toolpaths regulate how the heat is conducted into the workpiece, it represents a way to control the thermal cycle, residual stresses and distortion.

2.1.2.4 Corrosion resistance

Corrosion resistance of 3D printed components has been investigated by different authors. The corrosion resistance is influenced by material properties and process conditions. Microstructure is the one of the main factors in determining the corrosion performance of the material.

Phase composition, grains, precipitates and chemical composition determine the propensity to corrode (Ralston and Birbilis, 2010) (Nishimoto and Ogawa, 2016). At the same time all these factors are controlled by the process condition. During WAAM thermal cycle determines the microstructure and phase composition in the material. Moreover segregation of alloying elements and partial redistribution occur during printing. Thermal cycle induces phase transformation and heat treatment which can lead to precipitation. All these phenomena in WAAM are not uniform, the material is haet treated from the bottom to the top, thus a non-uniform microstructure is present (Xu et al., 2017). Schmidt et al. (Schmidt et al., 2015) reported a uniform corrosion performance for AISI 4340 printed with SLM.

Li et al. (Li et al., 2018) have investigated the corrosion resistance of P20 tool steel manufactured with SLM process. They compared the results with as-supplied samples and tempered sample at different temperatures. The printed material shows slightly lower corrosion resistance compared to the others. This can be attributed to the AM process features. Presence of pores and voids can cause of crevice corrosion. Rapid solidification is non-equilibrium, under which phases are strained, promoting corrosion. Tempering favor stress relief, improving the corrosion resistance.

2.2 Experimental apparatus

The 3D printing of P20 tool steel has been conducted using a Panasonic TM1400 MIG Welding robotic system from Valk Welding. The set-up is proposed in Figure 2.12.

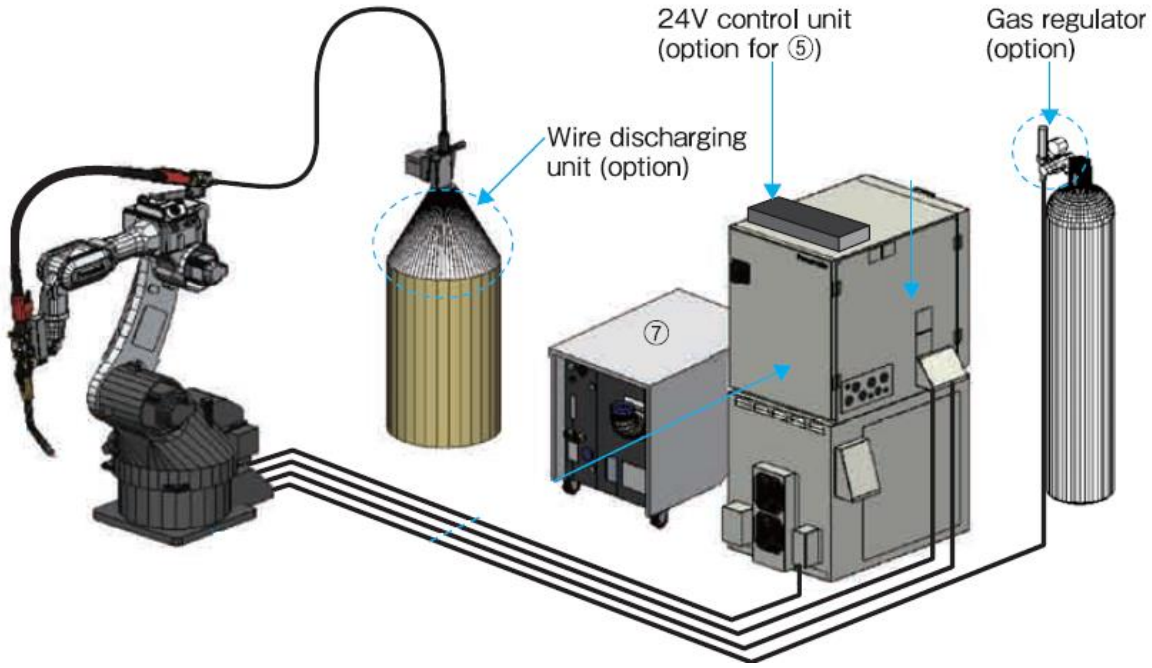

Figure 2.12 WAAM set-up

Two types of gas mixture have been used: 80:20 Argon/CO_2 and Ferromaxx® Plus 68:20:12 (Ar:He:CO_2). The consumable wire is provided by "Weld Mold Company", a 0.9 mm diameter wire for MIG welding with chemical composition in Table 2.1.

Table 2.1 Chemical composition P20 MIG welding consumable

El.	Fe [wt%]	C [wt%]	Cr [wt%]	Mn [wt%]	Mo [wt%]	Si [wt%]	Cu [wt%]	Al [wt%]	Ni [wt%]	P [wt%]	Ta [wt%]
Conc.	96.028	0.37	1.63	0.61	0.39	0.32	0.35	0.025	0.15	0.012	0.115

The experiments were conducted on a plate of 250x60x10 mm^3 made of plain carbon steel. The plate clamped on the static table in order to avoid distortions during the depositions and movement of the piece.

2.3 Experimental procedure

2.3.1 Optimization of process parameters

In order to investigate the suitable process parameters for the deposition of P20 steel, current voltage and torch speed have been modified. The ramping technique has been used, it consists of

four steps where energy input, speed, current, and voltage are changes selectively to study the effect on the resulting bead geometry and quality. The stick-out (distance between wire and the metal substrate) is kept constant to 15 mm.

Table 2.2 Parameters used for energy ramping at different speeds.

	V [Volts]	Current [I]	Speed [m/min]		
1	18	120	0.5	0.75	1
2	19.3	160	0.5	0.75	1
3	20.8	220	0.5	0.75	1
4	24.4	280	0.5	0.75	1
5	20.8	220	0.5	0.75	1
6	19.3	160	0.5	0.75	1
7	18	120	0.5	0.75	1

Table 2.3 Parameters for current ramping

	V [Volts]	Current [I]	Speed [m/min]
1	19.3	140	0.75
2	19.3	145	0.75
3	19.3	150	0.75
4	19.3	155	0.75
5	19.3	160	0.75
6	19.3	165	0.75
7	19.3	175	0.75
8	19.3	180	0.75

Table 2.4 Parameters for voltage ramping

	V [Volts]	Current [I]	Speed [m/min]
1	15.3	160	0.75
2	16.3	160	0.75
3	17.3	160	0.75
4	18.3	160	0.75
5	19.3	160	0.75
6	20.3	160	0.75
7	21.3	160	0.75
8	22.3	160	0.75
9	23.3	160	0.75
10	24.3	160	0.75

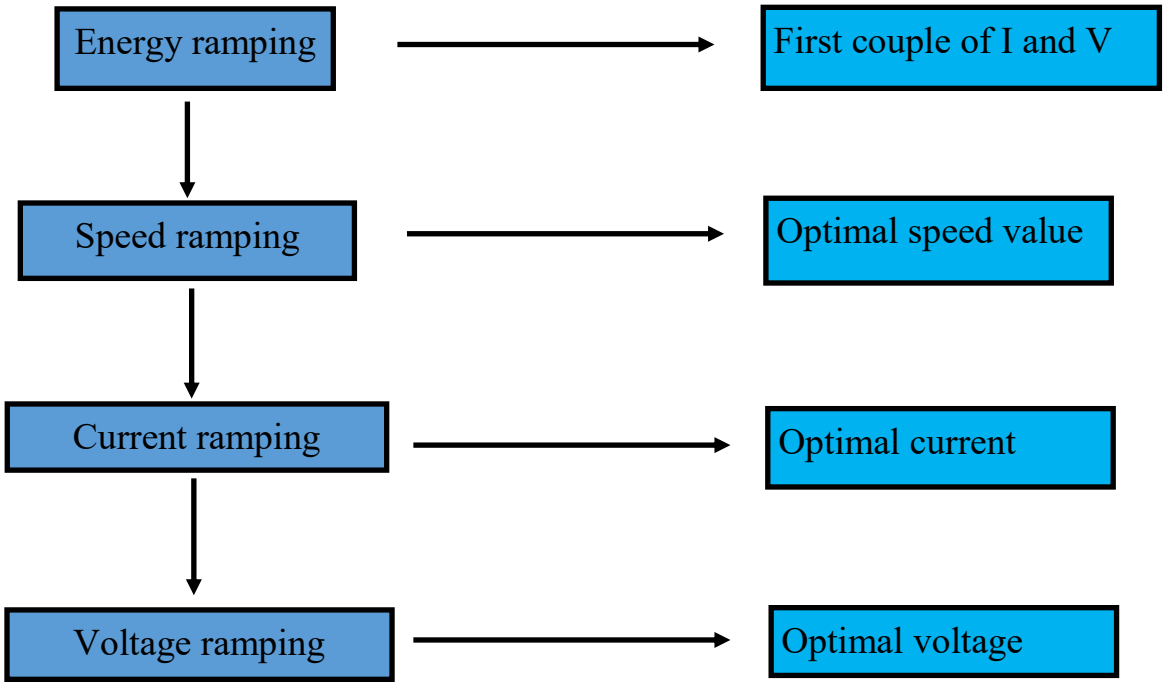

Figure 2.13 Scheme Ramping experiment

The experiment is schematically shown in Figure 2.13. During the energy ramping, the objective is to find a suitable couple of I and V, at constant speed. The parameters that have been used are illustrated in Table 2.2. In the second step the ramp in Table 2.2 is used with a different speeds: 0.75 m/min, 1 m/min and 1.5 m/min. During current and voltage ramping the parameters are changed in the range: 120-240 Amps with steps of 20 Amps and 14 – 26 Amps with steps of 2 Volts.

In each step the optimal set of parameters is found by checking the surface quality of the bead, the presence of spatter, arc stability, width and height. Once the set of parameters is found, it is kept constant in the following steps. In this way it is possible to see the effect of each parameter on the deposition. At the end of the experimental process it is possible to introduce small modification to optimize the deposition.

2.3.2 Multi-bead deposition

Multi bead experiment is important to define the deposition features of the selected material. The first step is to study the behavior of beads during overlap test. In this case different types of overlaps have been tried (30%, 40%, 50% of the total width W) and then compared with the TOM model.

One single layer is deposited, flatness and surface roughness are checked to maximize the accuracy of the final component and avoid presence of voids. In the second step multiple layers are printed one on top of the previous, with a layer height equal to the height of the bead. The final

height, the flatness, the stick-out and the surface roughness are checked. The scheme of the overall experiment is presented in Figure 2.14.

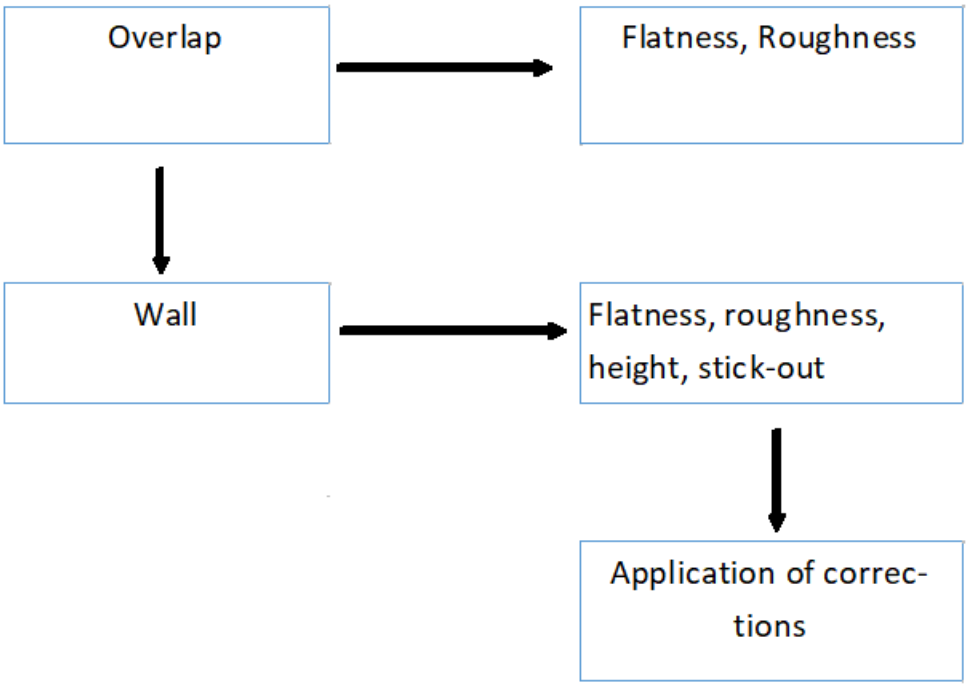

Figure 2.14 Scheme Multi-Bead experiment

2.3.3 Production of the reference sample

A reference sample was printed in order to investigate the microstructure of P20 steel. A wall of 7 layers each of them made by 6 beads was deposited on a plain carbon steel substrate clamped on a working table. The sample was produced using the optimized process parameters in Table 2.5.

Between following layers the order of deposition of the beads is reversed. This strategy increases the flatness of the component.

2.3.4 Temperature measurement

The objective of this experiment is to simulate which is the heat cycle in a specific point at the surface during printing. A sample equivalent to the reference sample has been manufactured to perform the temperature measurement. The sample has been manufactured with the optimized process parameters. A thermocouple T1 was installed on the side of the last printed layer at a distance of 2 mm from the surface and at half of the wall length. A second thermocouple T2 has been installed close to T1 at the same height to have a second measurement for confirmation. Another thermocouple T3 was placed on the substrate to have a reference temperature. Figure 2.15a) shows a general overview of the set-up of the experiment. Figure 2.15b) shows the cross section of the sample which is subjected to the experiment. The last layer is marked in blue. It represents the layer at which the material (in grey) have been added.

The substrate is clamped on a static table to minimize distortions.

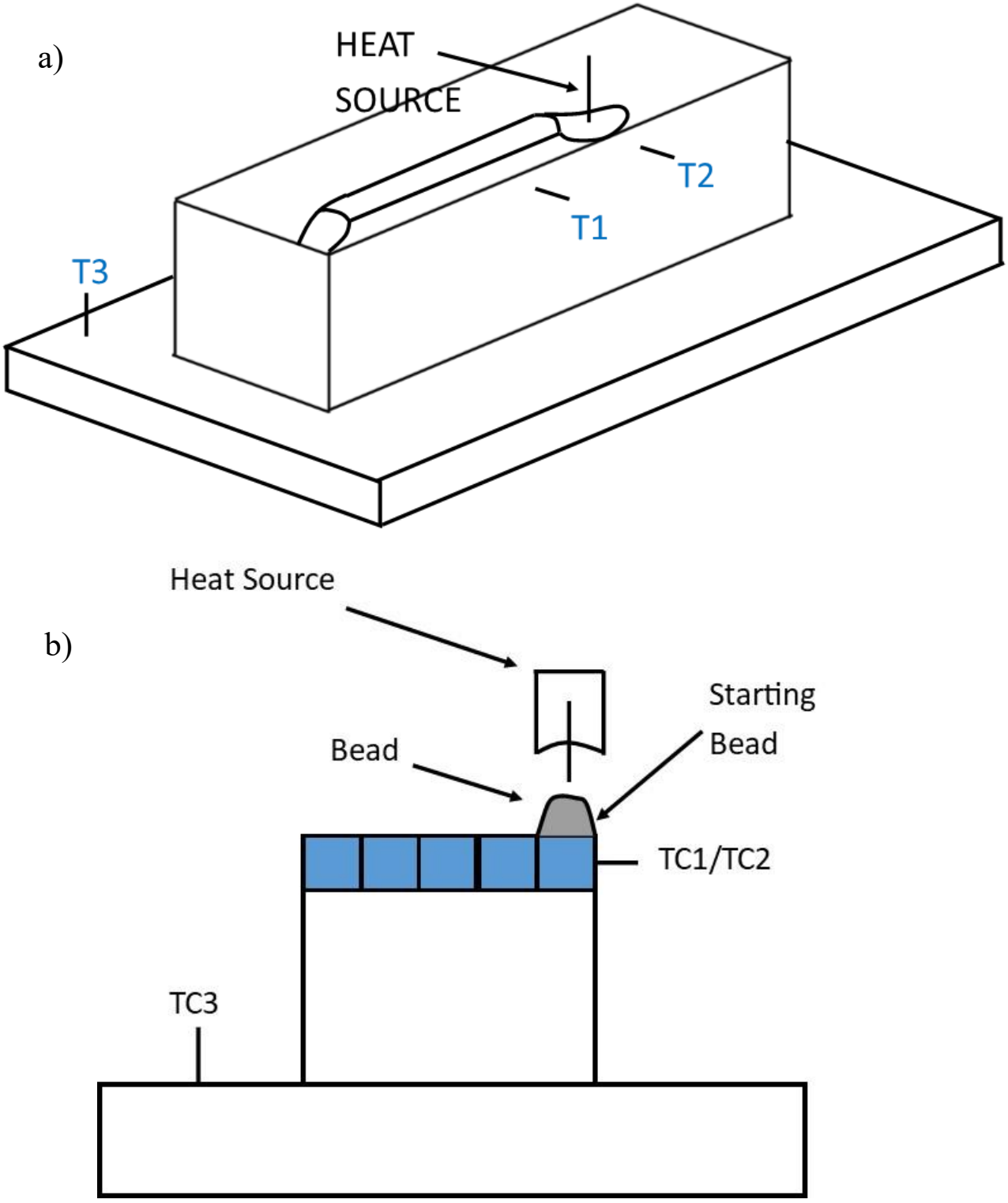

2.15 a) Scheme of the temperature measurement set-up. b) Cross section of the experimental set-up.

2.3.5 Dilatometry

Dilatometry tests were performed in order to confirm the correlation between the thermal cycles and microstructure. The machine used to perform the test is Bahr 805 Quench dilatometer. Cylindric samples with a diameter of 4 mm and length of 10 mm, were obtained by Wire Electric Discharge Machining (wire EDM) from a wall of P20 steel printed with the optimized process parameters. The initial microstructure of P20 steel before the dilatometer analysis shows dendrites. Since the samples were cut from a printed wall, the microstructure of the samples could varies in grain size, due to the fact that they could be taken by areas with different thermal history.

The objectives of the dilatometry are:

- To study the solid state phase transformations of the material;
- To simulate the heat cycle;
- To investigate material properties under different heat cycles;

The influence of grain size on solid state phase transformation has been neglected (Yang and Bhadeshia, 2009).

The samples were subjected to austenitization at 860 °C for 4 min and cooled down at room temperature with 3 different cooling rates: quenching (100°C/s), 5 °C/s and 1°C/s. The thermal cycles are presented in Figure 2.16.

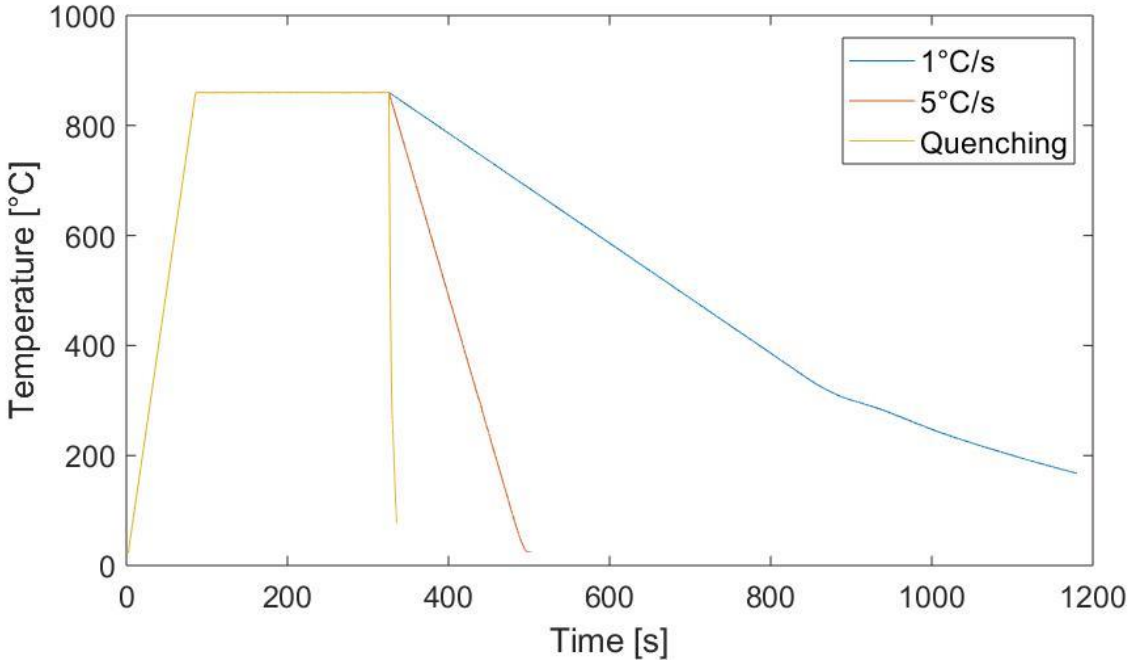

2.16 Heat treatment cycle during dilatometric analysis

A dilatometric test was performed at 900°C for 4 min, quenching to room temperature and following tempering at 600°C for different times: the sample T60 has been treated for 60 minutes,

while the sample T5 only for 5 minutes. The heating rate to the tempering temperature is 10°C/s and the final cooling rate is 20°C.

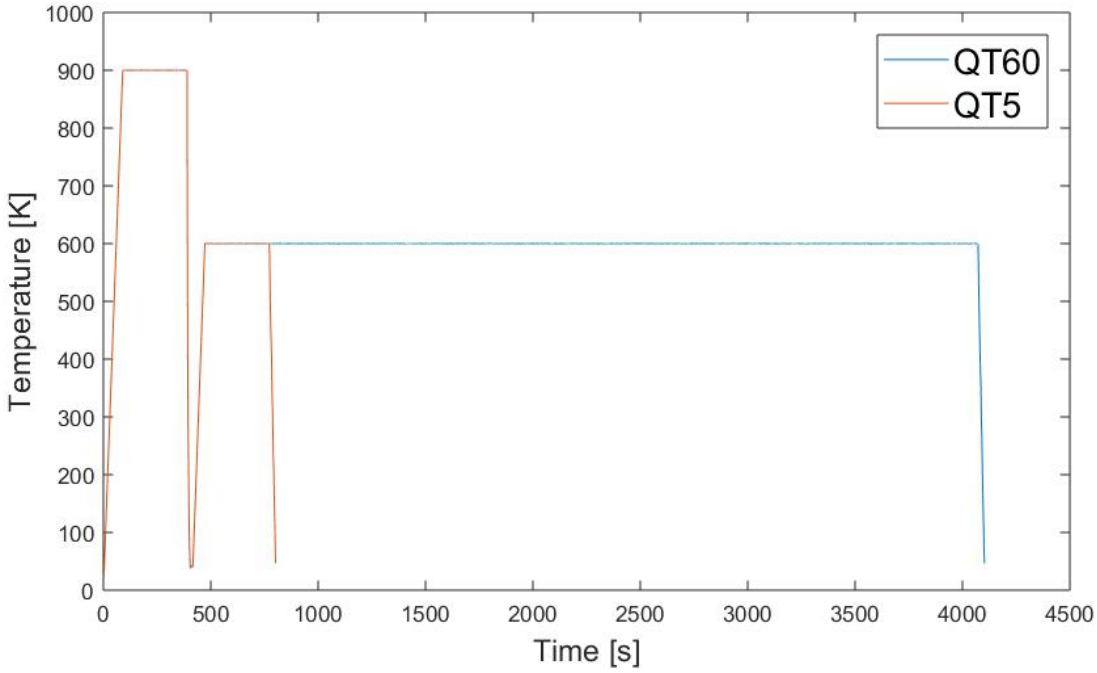

Figure 2.17 Thermal cycle of the QT60 and QT5 sample

In order to compare the as deposited microstructure of WAAM produced P20 steel, a comparison with QT P20 steel has been performed. Figure 2.17 shows the two heat treatments conducted on the sample. The first is the traditional QT heat treatment. The material is austenitized at 900 °C for 5 min, quenched and tempered ad 600°C for 60 minutes. In the second heat treatment, the material has been tempered for 5 minutes.

2.3.6 Chemical analysis

During solidification alloying elements segregate at the liquid-solid interface. The extent of segregation creates heterogeneities which affect the material properties. A WDS analysis has been conducted to evaluate the amount of segregation. The analysis was performed with a JEOL JXA 8900R micro probe with an electron beam of 10 eV.

A line scan of 170 µm was performed across the dendrites to measure the segregation at the boundary. The content C, Cr, Mn, Si and Mo was determined.

2.3.7 Sample preparation and etching technique

In order to reveal the microstructure evolution during WAAM the reference sample has been used. Metallographic samples of the cross sectional surface of wall were prepared using the standard procedure and final etching.

Two different types of etching solution have been used to investigate the microstructure:

- Nital: 2% of HNO_3 in ethanol. It shows prior austenite grain boundaries. Ferrite, perlite and bainite react to the etching. Martensite remains un-etched (Erisir, Gümüs and Bilir, 2013);
- LePera: 1g of metabisulfite in 100 mL of distilled water and 4g picric acid in 100 mL ethanol. This etchant allows distinction between ferrite, bainite and martensite (Erisir, Gümüs and Bilir, 2013);

The phases and microstructure were investigated with an optical microscope Olymus UTV1X. Macro of the samples were obtained with the microscope VHX Keyence.

2.3.8 Hardness

The study of the hardness profile has an important role in the investigation of material properties, especially in the case of steel used for plastic mold. Vickers hardness test was performed with an hardness machine Struers Durascan. The applied load was set to 0.5 kg. The point measurements were taken along a line which starts from the bottom of the wall towards the top, perpendicular to the base plate. A second line measurement is taken in the last layer to compare hardness value with the first. The points are spaced by a distance of 0.5 mm in order to take into account possible variations of the hardness due to the presence of different types of grain structures. Figure 2.18 shows the two line measurements.

2.3.9 Polarization test

Three rectangular samples TM1, TM2 and TM3 of 15x15x3 mm^3 (LxWxT) were taken from the longitudinal cross section of the bulk. The specimen were taken from the layers beneath, were tempered martensite is present.

The samples were ground with 80-, 180-, 320, 800-, 1200-, 2000-grit SiC paper in order to obtain a smooth surface. Ultrasonic bath in ethanol was used to clean the surface. The samples were then masked leaving a circular area of 0.28 cm^2 exposed to the electrochemical experiment. It was ensured that no air was entrapped around the hole. Scratches on the mask were not present. Copper tape was attached on the bottom surface of the specimen in order to establish electrical contact with the specimen. A solution of 3.5 % in weight of NaCl in distilled water was prepared.

The polarization measurements were performed using a three-electrodes cell. The cell is composed of the working electrode (WE, which corresponds to the specimen), reference electrode (RE) and counter electrode (CE). The three electrode were immersed in a beker (making sure that the copper tape of the WE was not immersed) where 130 ml of solution was poured. The OCP potential was monitored for 30 minutes until a stable OCP was achieved. Polarization measurements were performed from – 0.25 to 1 mV (vs. OCP). After each measurement the solution was changed and the samples were observed with naked eyes to ensure an homogenous corrosion and no presence of corrosion beneath the mask.

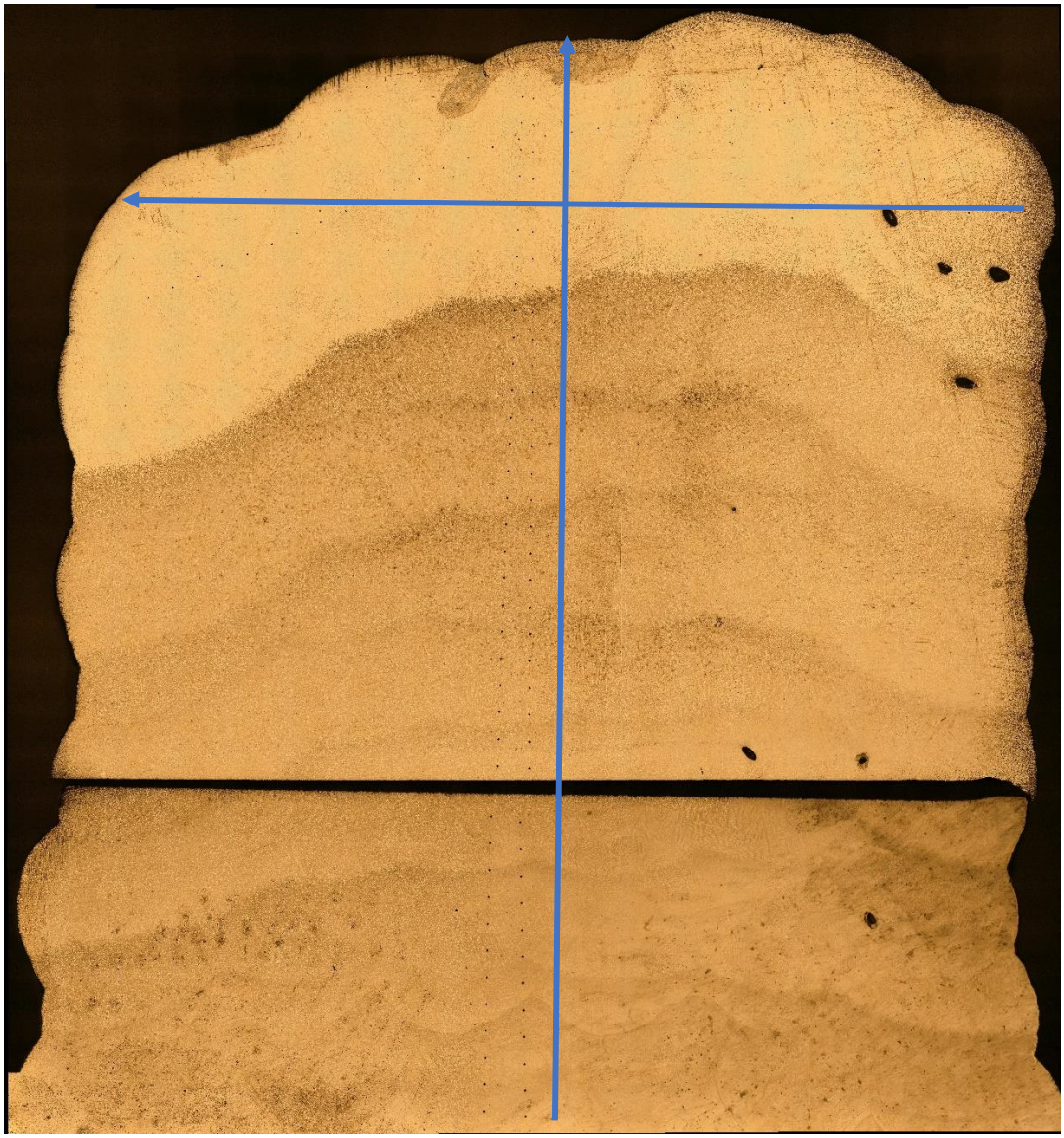

Figure 2.18 Macrograph of the deposited wall showing the two line measurements

2.4 Results of the experimental study

2.4.1 Optimization of process parameters

The outcome of the ramping technique is the optimized process parameters and, as a consequence, the bead geometry. The optimal process parameters are shown in Table 2.5.

Table 2.5 Optimized process parameters

I [Amps]	V [Volts]	S [m/min]
150	18.8	0.6

The height and width of the bead are 2.5 mm and 5.2 mm respectively. The overlap is 3 mm (40 % of the bead width) and the step up is taken as the bead height. The Ferromaxx plus ® mixture gives better results in terms of reduction of lack of fusion and macro-porosity. The delay time is set to 2 minutes, which allows cooling between 200°C and 250°C.

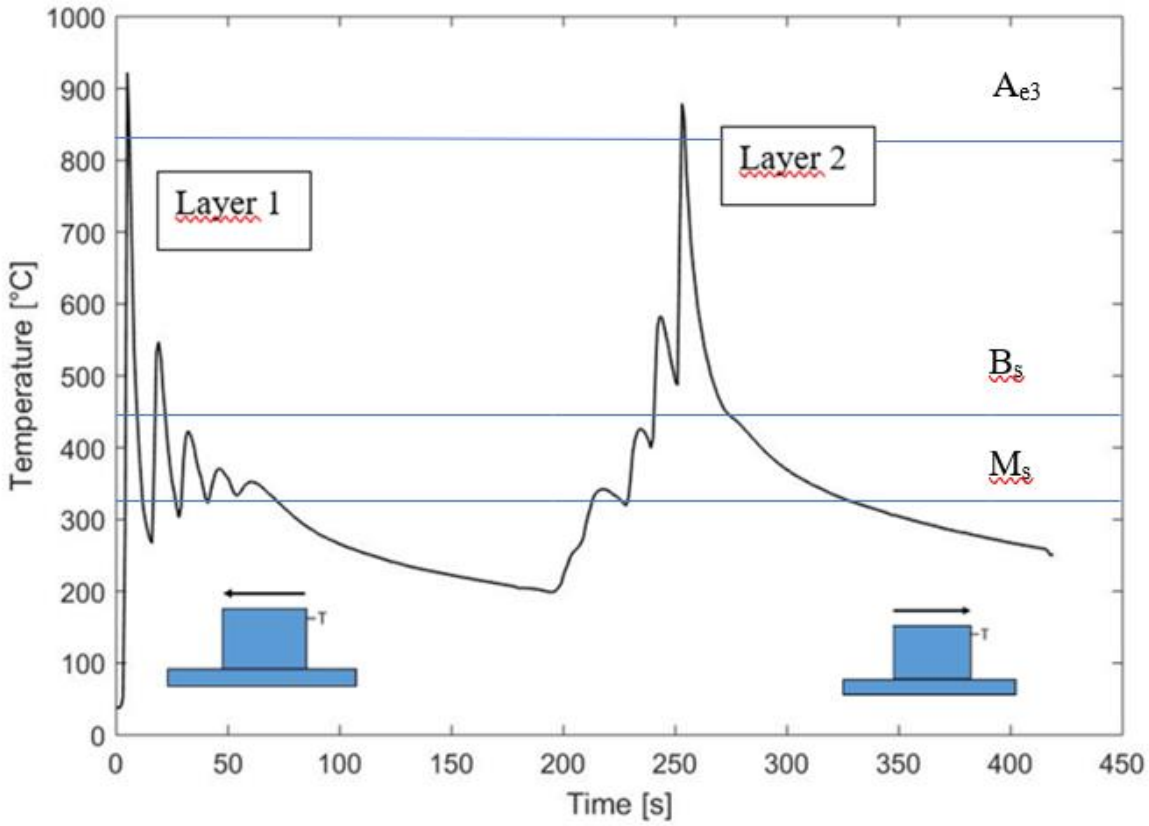

Figure 2.19 Therma cycle of the first two layers

2.4.2 Temperature measurement

The thermal cycle during the deposition of the first two layers is proposed in Figure 2.19. The observation of the temperature profile gives the following information:

- The temperature profile can be split in two blocks: first layer and second layer, separated by the delay time;
- The peak temperatures can be sorted in: γ-peak, tempering peak and pre-heating peaks. The first refers to those peaks which induce complete austenitization during heating (T> 820°C) and the second to those peaks which promote tempering;

As can be seen in Figure 2.19 the temperature distribution changes for the second layer. This is due to the reversing of the bead sequence. In the first block the bead cools down during the deposition while in the second block is pre-heated.

In the first block the main features of the plot that must be taken in consideration are:

- Peak temperature: controls the austenitization;
- Valley temperature: regulates the fraction which transforms during cooling;
- Cooling rates: determines the solid state transformation during cooling;

The peak temperature decreases during the printing because the torch moves away from the measurement point. After the peak temperature is reached, cooling occurs. The cooling rate tends to decrease because of the effect of pre-heating which leads to accumulation of heat. As a consequence the valley temperature increases.

In the second block this fact is not true because the last peak controls the transformation since is the highest. In fact, the initial 4 peaks act as a pre-heating and the fifth induce the phase transformation. The main information to consider as valuable is the fact that reversing the layers the previously deposited microstructure is the effect of sequence of deposition on the heat cycle. Here, it must be remarked that the temperature profile refers to a point on the surface, while the core the situation can be different.

Figure 2.20 shows the complete thermal cycle when the entire block is printed. After the printing of the first and second layers the material starts to cool down. It is still subject to a descendent heat cycle. Even though the torch moves faraway, the temperature remains around 400 °C for some time. In Figure 2.21 a table of the tempering parametes of P20 steel is proposed. Hardness, strenght and resilience are measured in function of the tempering table. As can been seen between 400°C and 450°C there is a minimum in the resilience. This must be taken into account for a possible application.

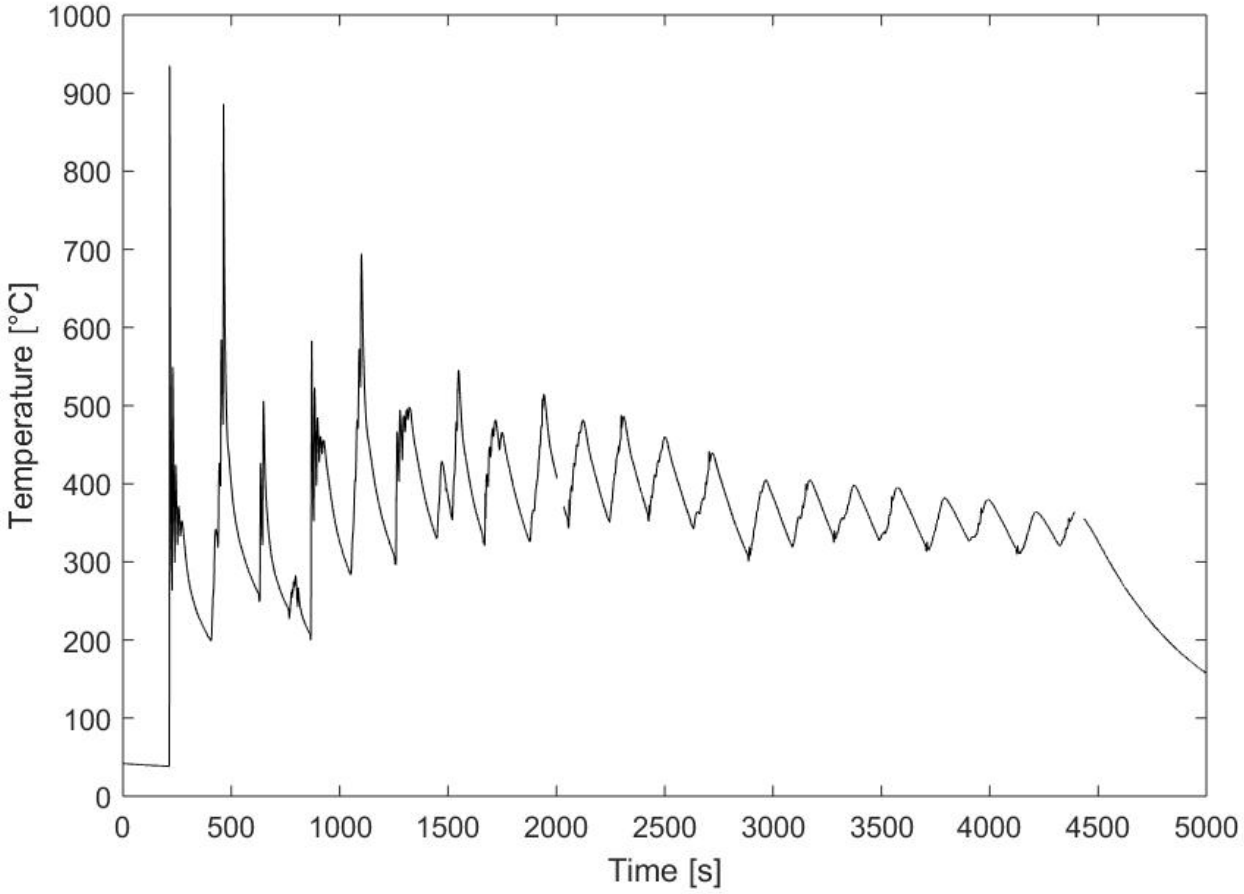

Figure 2.20 Complete thermal cycle

Tempering table after quenching at 860 °C in oil															
HB		496	496	489	482	468	455	442	432	409	390	353	336	271	240
HRC		51	51	50.5	50	49	48	47	46	44	42	38	36	28	21
R	N/mm²	1820	1820	1790	1760	1700	1640	1580	1520	1430	1340	1180	1110	900	800
Kv	J						8	8	8	7	9	14	20	30	
Tempering at **°C**		**50**	**100**	**150**	**200**	**250**	**300**	**350**	**400**	**450**	**500**	**550**	**600**	**650**	**700**

Figure 2.21 Tempering table of P20 tool steel

2.4.3 Microstructure

A macrograph of the cross section of the deposited wall is proposed in Figure 2.22. The first characteristic is the presence of a layered structure that recall the deposition of the layers. Distinction between the single beads is more difficult to note, due to the repeated thermal cycles which caused the homogenization of the microstructure. Along the different layers the microstructure is characterized by columnar dendrites, even though some localized morphological

heterogeneities are present: the dendrites can vary locally from cellular to columnar, and either equiaxed, due to the different thermal gradients and rate of growth.

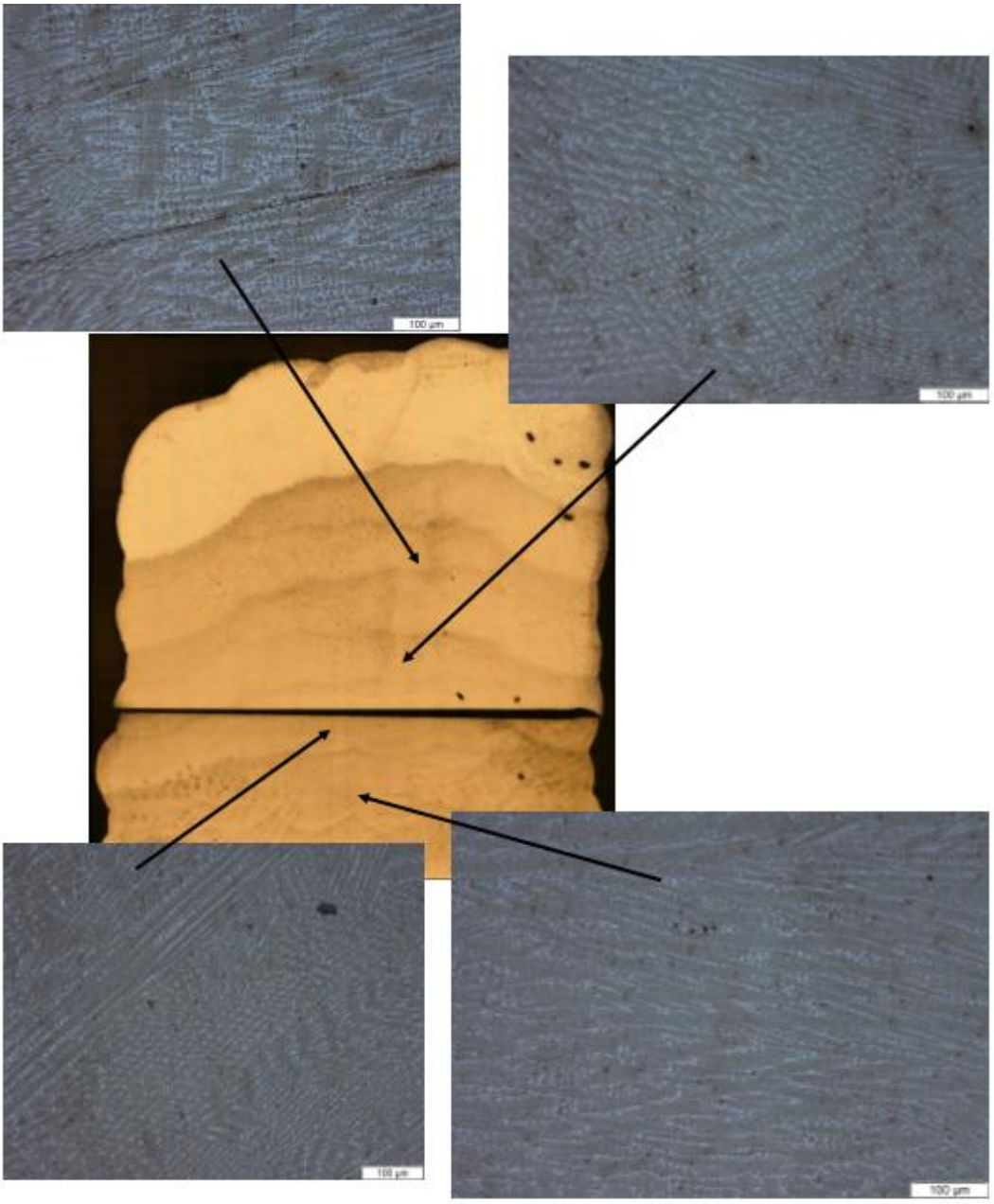

Figure 2.22 Microstructure on different level of the wall

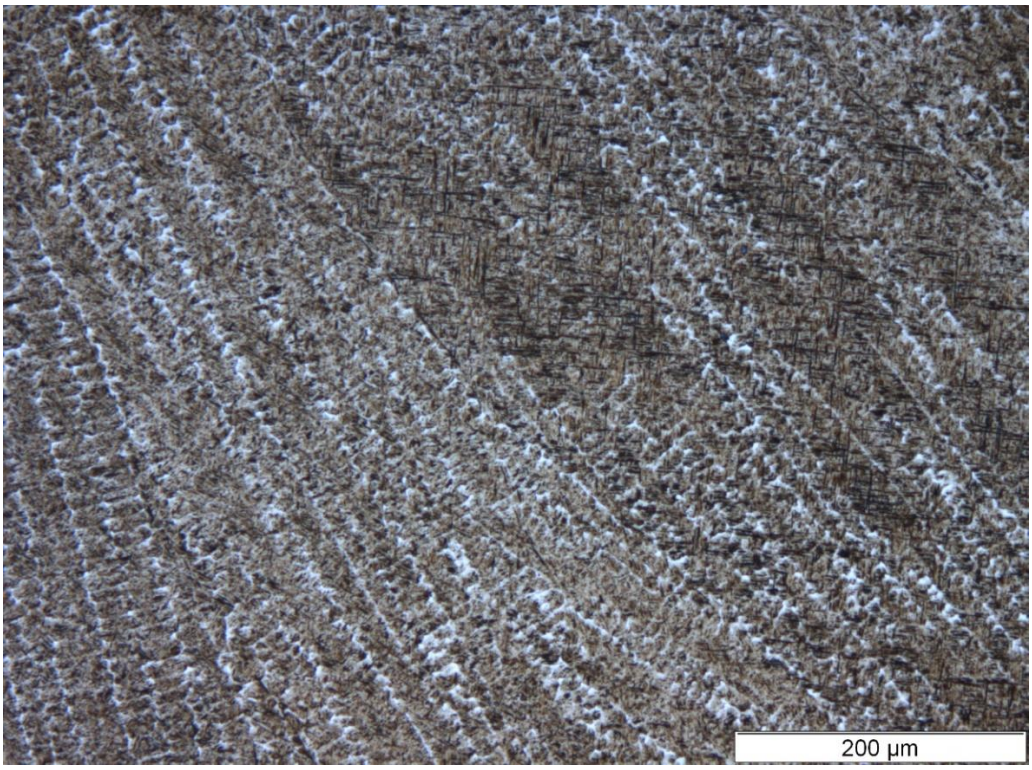

Figure 2.23 Microstructure of the last deposited layer

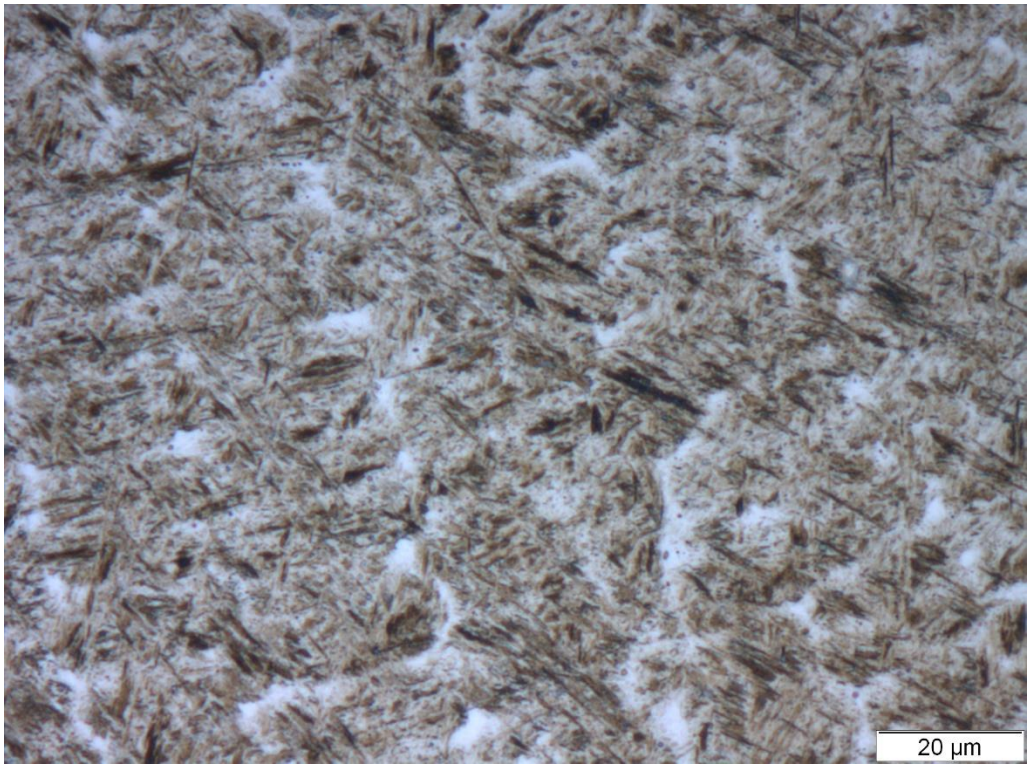

Figure 2.24 Microstructure of the last deposited bead at 1000x

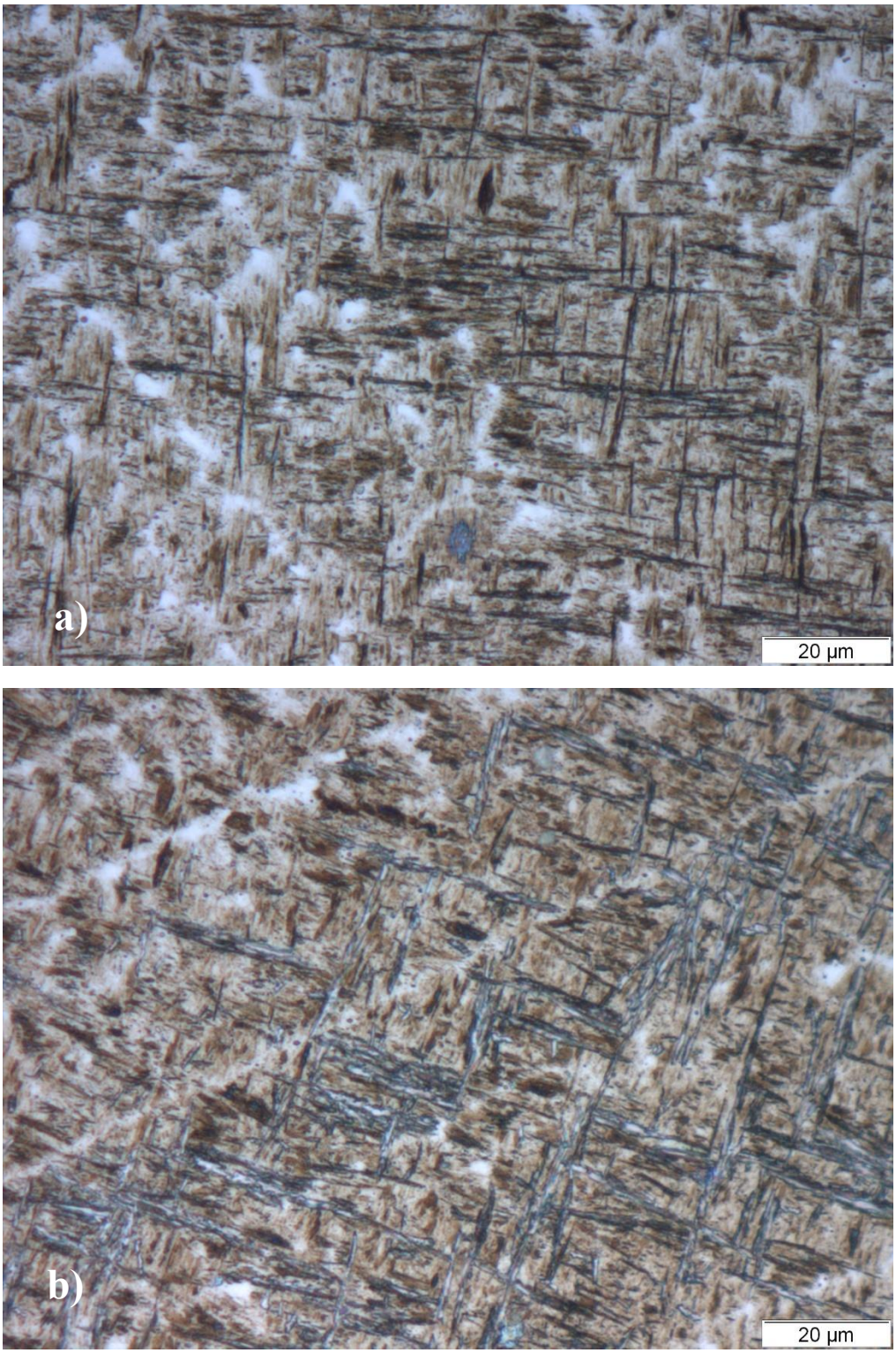

Figure 2.25 Higher magnification of the acicular constituent: a) last deposited bead and b) first deposited bead of the same layer

In Figure 2.22 it is possible to note that the last two layers appear with a different color compared to the previous. This is associated with the different response to the etchant on different types of microstructural constituents. In fact the last layers undergo a different thermal cycle compared to the one at the bottom, with generation of diverse microstructures. One can consider that the last layer is the only one that was not re-heated, thus provides the real as built unaffected microstructure. On the contrary, independently by the layer location segregation of alloying elements occurs during solidification, promoting the formation of a banded structure (detectable in each layer of the wall). The deposited wall does not show lack of fusion, meaning that a full bonding between following layers has been reached. Some porosities are visible in the last layer, that is the most defect affected one.

Figure 2.23 shows the microstructure of the last deposited bead. An higher magnification is proposed in Figure 2.24. Three microstructural constituents can be detected:

- A: characterized by a white color. Mainly present at the dendrite boundary and in minor quantity inside the dendrite;
- B: characterized by a dark/brown color;
- C: acicular constituent with an apparent black color (Figure 2.25a)). In Figure 2.25b) the same microstructural constituent appears white, the needles thicker and in higher fraction. In some cases the needles seem to nucleate from inclusions and growth preferentially along two perpendicular direction;

The comparison of the two microstructure revealed by the Nital etching and LePera etching are proposed in Figure 2.26. When etching with LePera the constituent A has a white color, B brown and C light blue.

Figure 2.27 shows the microstructure of the bottom layers. The dendrites are visible, with a smaller amount of A constituents at the dendrite boundary. The acicular constituent C is still visible with a white color. The dendrite is characterized by a dark matrix which shows sub-constituents.

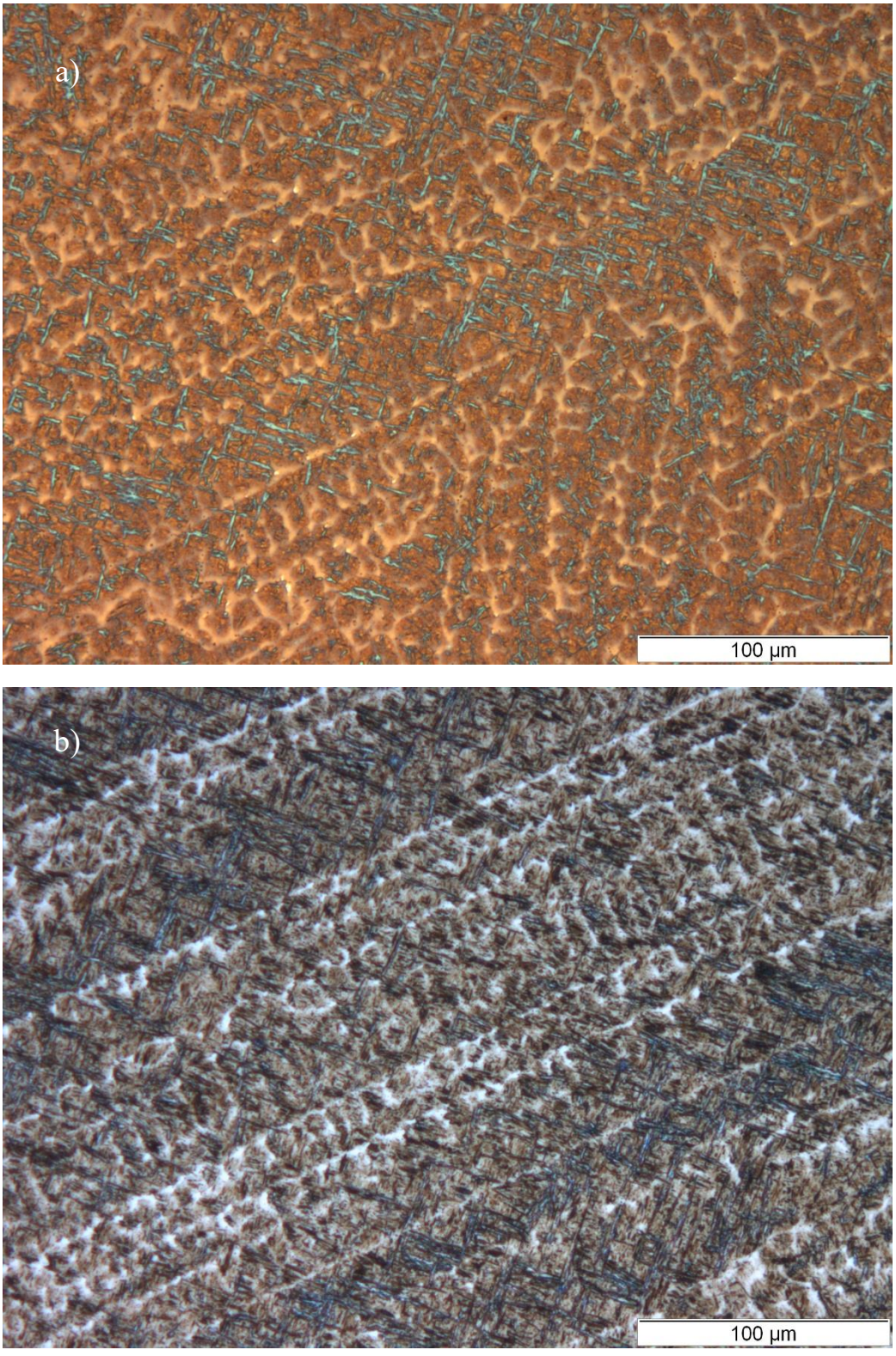

Figure 2.26 a) LePera etching and b) Nital etching

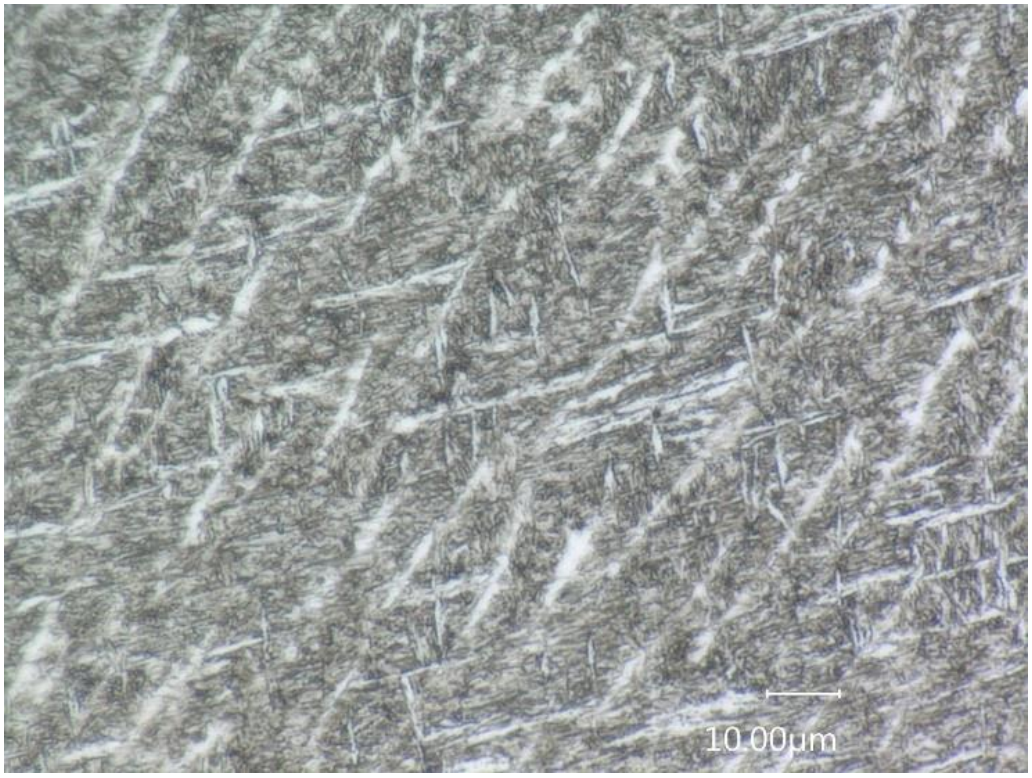

Figure 2.27 Microstructure of the 5th layer of the wall

2.4.4 Chemical analysis

The amount of C, Si, Cr, Mo and Mn along the line measurements is shown in Figure 2.28.

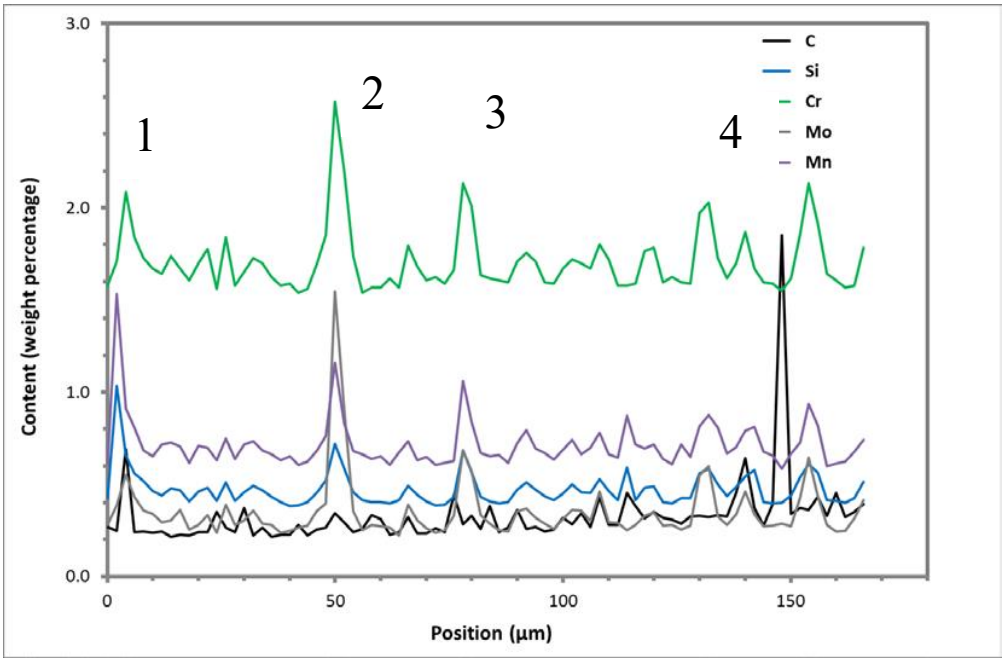

Figure 2.28 EPMA analysis for C, Si, Cr, Mo and Mn

Figure 2.28 suggests the presence of two type of segregation: intra-dendrite and inter-dendrite segregation. For this study inter-dendrite segregation is addressed to be more influent on the microstructure.

The peaks considered in this study marked with numbers (1,2,3 and 4) in Figure 2.28. Peak number 2 will be considered for further study on the effect of segregation on the microstructure.

2.4.5 Dilatometry study

Different cooling rates have been studied, from quenching to 5°C/s, and finally 1 °C/s. The wide range of cooling rates chosen can be justified by the fact that the material is designed to form easily martensite during cooling, thus investigation on the critical cooling rate for the formation of other phases is also interesting for the purpose of this study.

The dilatometric curve for the quenched samples, cooled down at 5 °C/s and 1°C/s is proposed in Figure 2.29, 2.30 and 2.31. For all the samples the austenitization occurs in the same temperature range, between 760 °C and 820°C.

During cooling the quenched sample shows a linear contraction, at around 320 °C the martensite transformation starts. With cooling rate of 5 °C/s the martensite transformation is shifted at 330°C, showing the effect of the cooling rate on the transformation. This change in the Ms can be also related with the different grain size between samples (Hanamura et al., 2013) as well as to the different cooling rate.

Regarding the sample cooled down at 1 °C/s the dilatometric curve appears slightly different compared to the others two, this can be related with the bainitic transformation. The dilatometric curve in Figure 2.31 suggests that after part of the austenite transformation in bainite, the rest is converted almost entirely in martensite. The transformation starts around 450 °C.

The dilatation curve of the QT60 and QT5 sample is shown in Figure 2.32. The two samples show the same behavior upon quenching: martensite transformation in the aforementioned temperature range. Above 300 °C both the curves show an increase in the dilatation, which refers to decomposition of retained austenite due to its instability at higher temperatures (Vieira et al., 2017). The following drop in the dilatation can be assigned to the precipitation of carbides (Vieira et al., 2017). From the point of view of the dilatometric experiment the two samples does not show any remarkable difference.

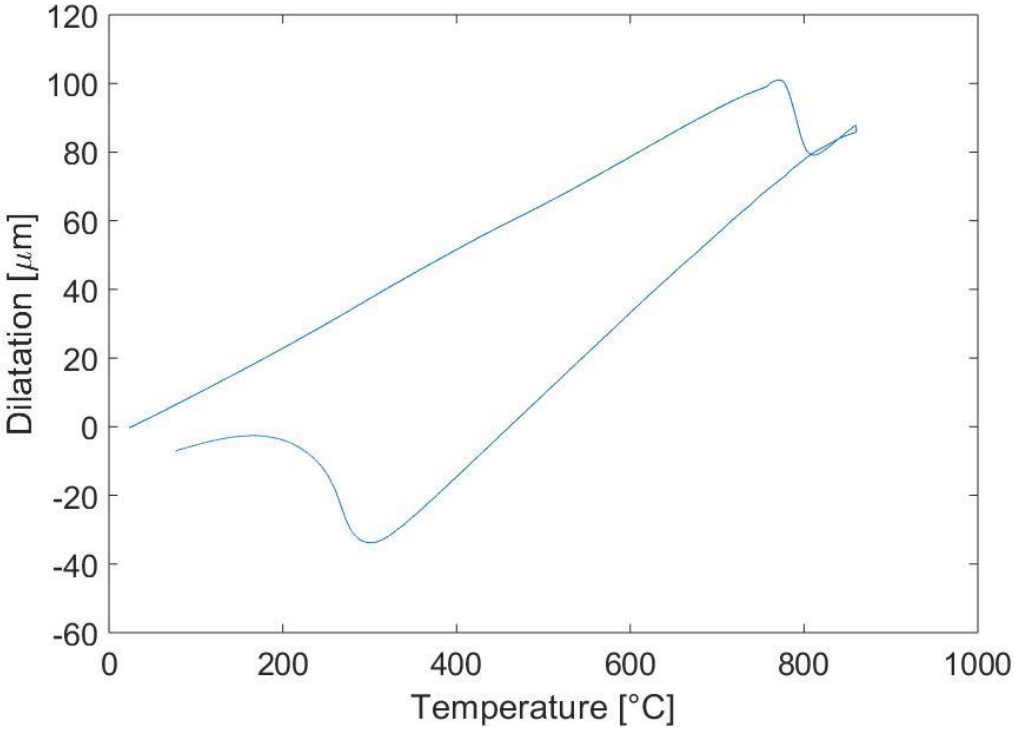

Figure 2.29 Dilatation curve of the quenched sample

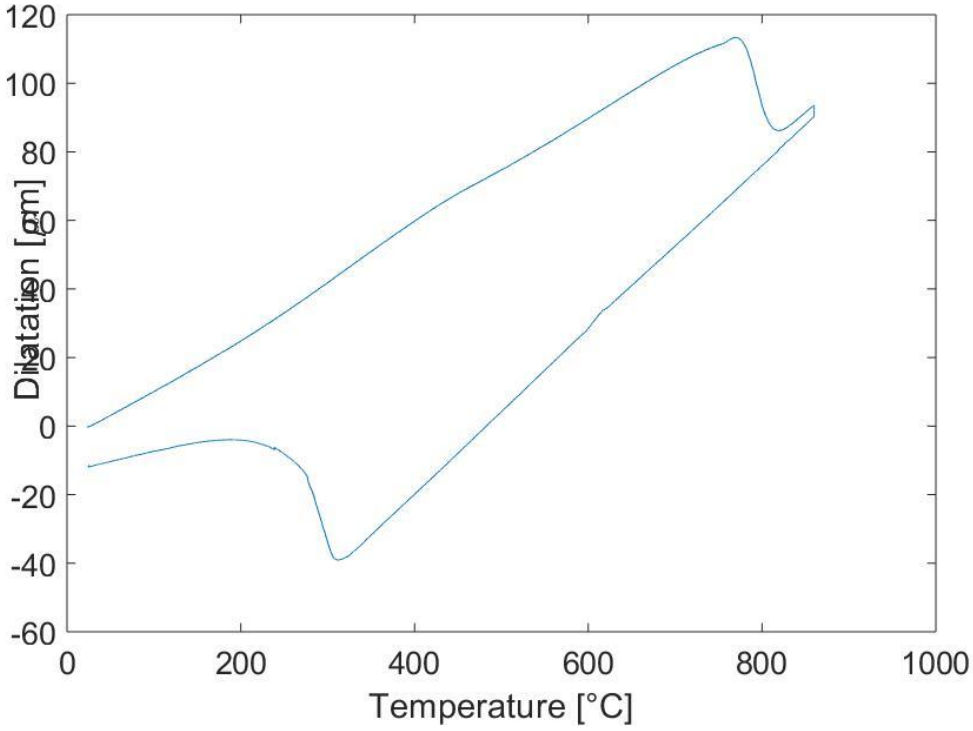

Figure 2.30 Dilatation curve of the sample cooled at 5°C/s

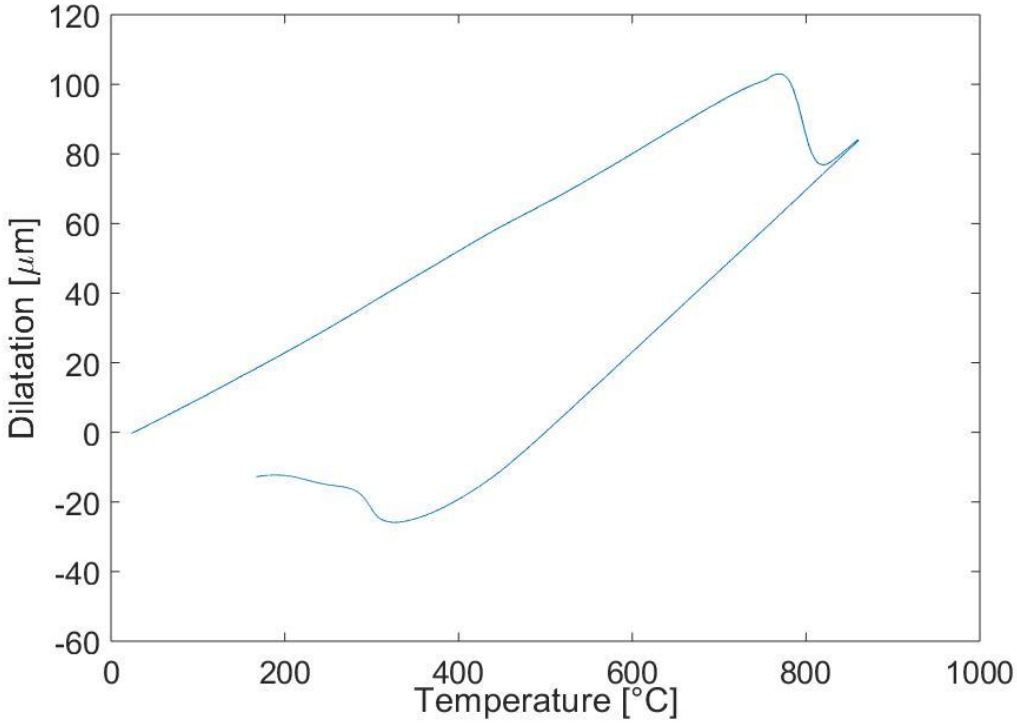

Figure 2.31 Dilatation curve of the sample cooled at 1°C/s

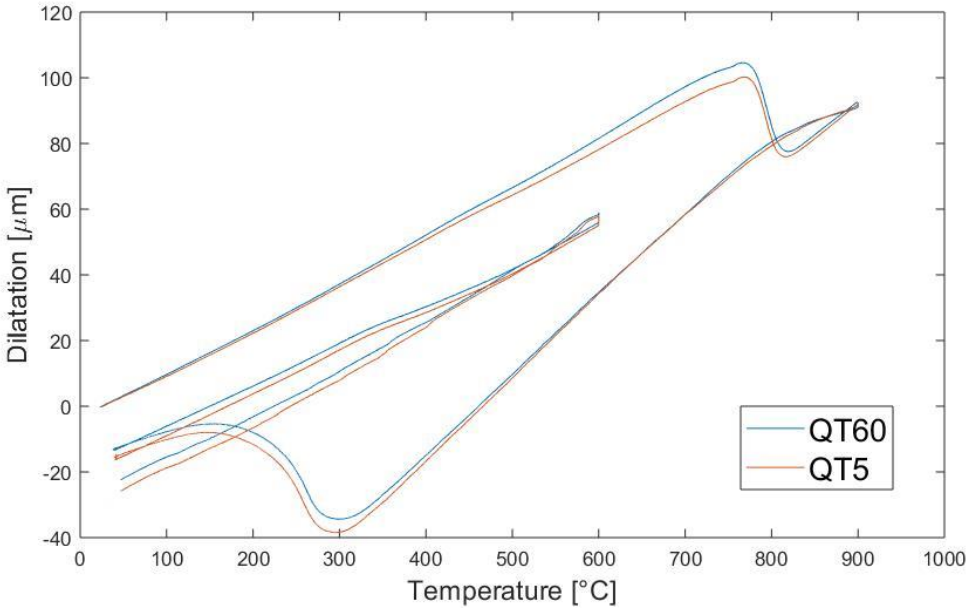

Figure 2.32 Dilatation curve for the QT60 and QT5 samples

2.4.6 Hardness profile

In Table 2.6 the hardness value along the wall cross-section is proposed. The hardness values show a scatter within the range 410 HV and 527 HV in the first 7 layers, while in the 8th layer the material

reaches 746 HV. Figure 2.33 shows the hardness profile along the wall height and Figure 2.34 along the last deposited layer. In Figure 2.33 and 2.34 the beads and layers are listed in the order of deposition. It means that the vertical trend line goes with the wall height, while for the case of the last layer the trend has to be read on the contrary.

Table 2.6 Results of the hardness values along the cross section of the Wall

Point number	Distance from the substrate [mm]	HV 0.5	
1	-0.50	450	Substrate
2	0.00	411	First Layer
3	0.50	458	
4	1.00	448	
5	1.50	427	
6	2.00	433	Second Layer
7	2.50	463	
8	3.00	485	
9	3.50	453	
10	4.00	410	
11	4.50	503	Third Layer
12	5.00	478	
13	6.10	469	
14	6.60	441	
15	7.10	527	Fourth Layer
16	7.60	489	
17	8.10	461	
18	8.60	434	
19	9.10	439	Fifth Layer
20	9.60	463	
21	10.10	474	
22	10.60	413	
23	11.10	527	Sixth Layer
24	11.60	521	
25	12.10	487	
26	12.60	468	
27	13.10	431	
28	13.60	465	Seventh Layer
29	14.10	451	
30	14.60	420	
31	15.10	724	Eight Layer
32	15.60	746	
33	16.10	688	

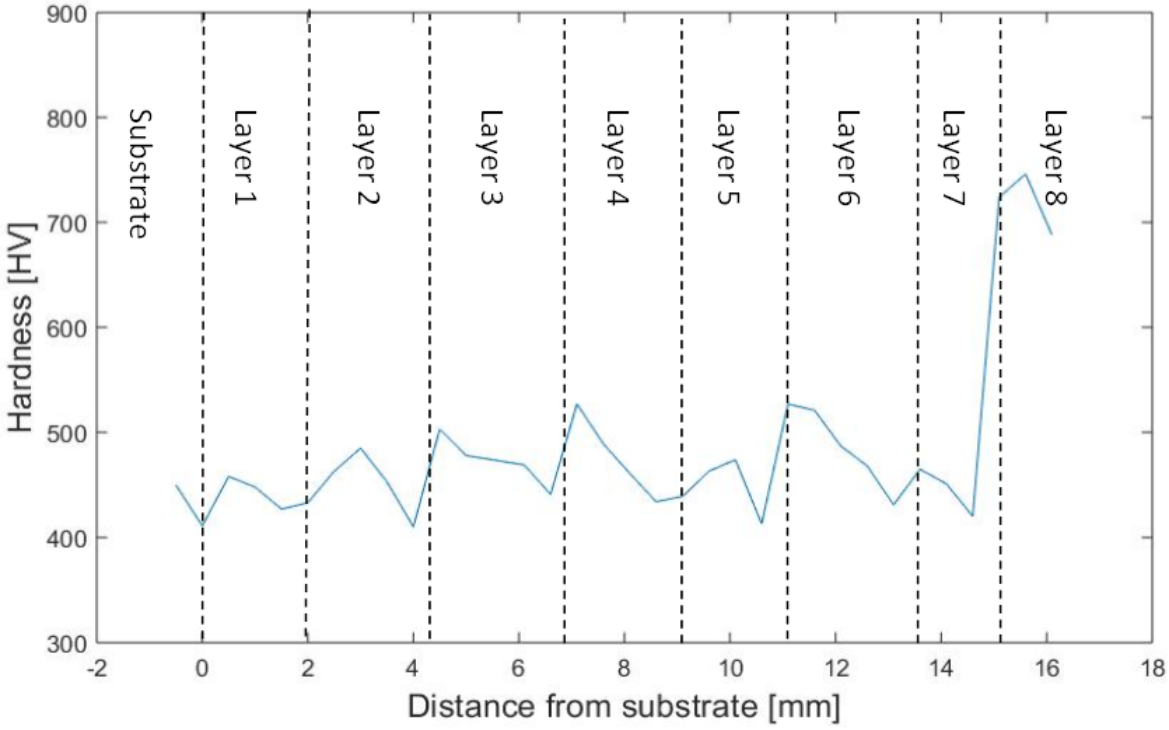

Figure 2.33 Hardness trend along the Wall cross section

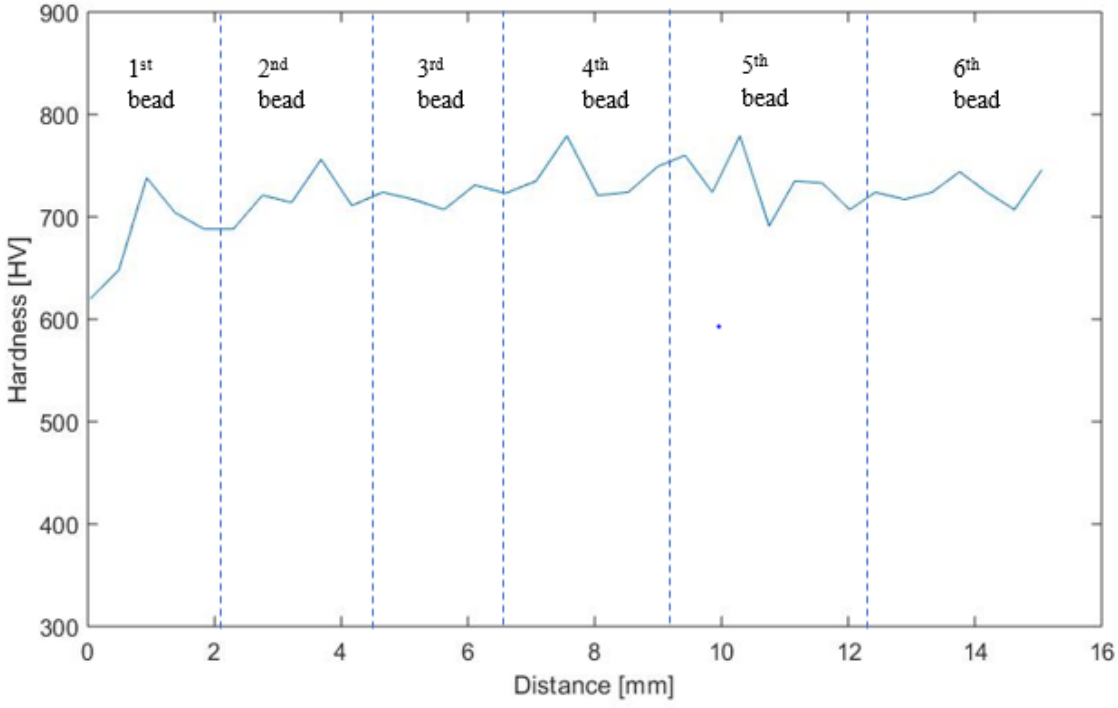

Figure 2.34 Hardness trend along the last layer

2.4.7 Polarization test

The polarization curves of the three tempered martensite samples (TM) are shown in Figure 2.35. In order to calculate the corrosion rate the Tafel method (Mccafferty, 2005) was applied. According to this method the corrosion current density can be calculated as the intersection of the linear parts of the anodic and cathodic polarizations curves. A schematization of the Tafel extrapolation method is proposed in Figure 2.36. The corrosion current density is extracted from the polarization curve. From the corrosion current density the corrosion rate can calculated. The corrosion rates and the corrosion potential are shown in Table 2.7.

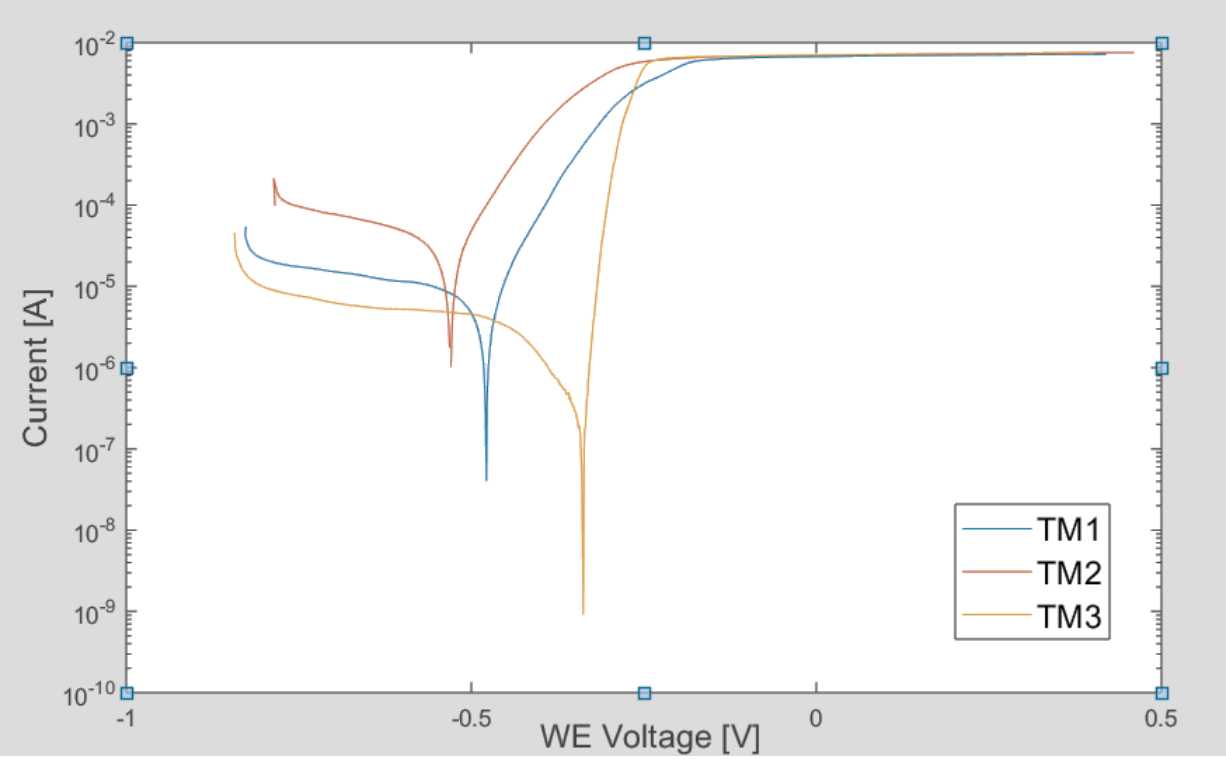

Figure 2.35 Polarization curves for the TM1, TM2 and TM3 samples

The corrosion rate is given by:

$$R_c = \frac{M}{nF\rho} * i_{corr} \qquad (2.10)$$

where M is the equivalent weight, n is the number of electron exchanges during the reaction, F is the Faraday constant, ρ and i_{corr} the corrosion density.

Table 2.7 Corrosion rates calculated with the Tafel model and corrosion potential for the specimens TM1, TM2 and TM3.

Specimen	Corrosion rate [mm/year]	Corrosion density [A/cm^2]	E_{corr} [V]	$\|b_a\|$ [V/dec]	$\|b_c\|$ [V/dec]
TM1	0.035934	3.09E-06	-0.4792	0.062399	0.078081
TM2	0.18959	0.000016316	-0.53135	0.07839	0.09058
TM3	0.010295	8.8599E-07	-0.33885	0.012423	0.012423

The corrosion rate for TM1, TM2 and TM3 is respectively 0.035934 mm/year, 0.18959 mm/year and -0.010295 mm/year. The corrosion potential for TM1, TM2 and TM3 is respectively -0.4792 V, -0.53135 V and -0.33885 V.

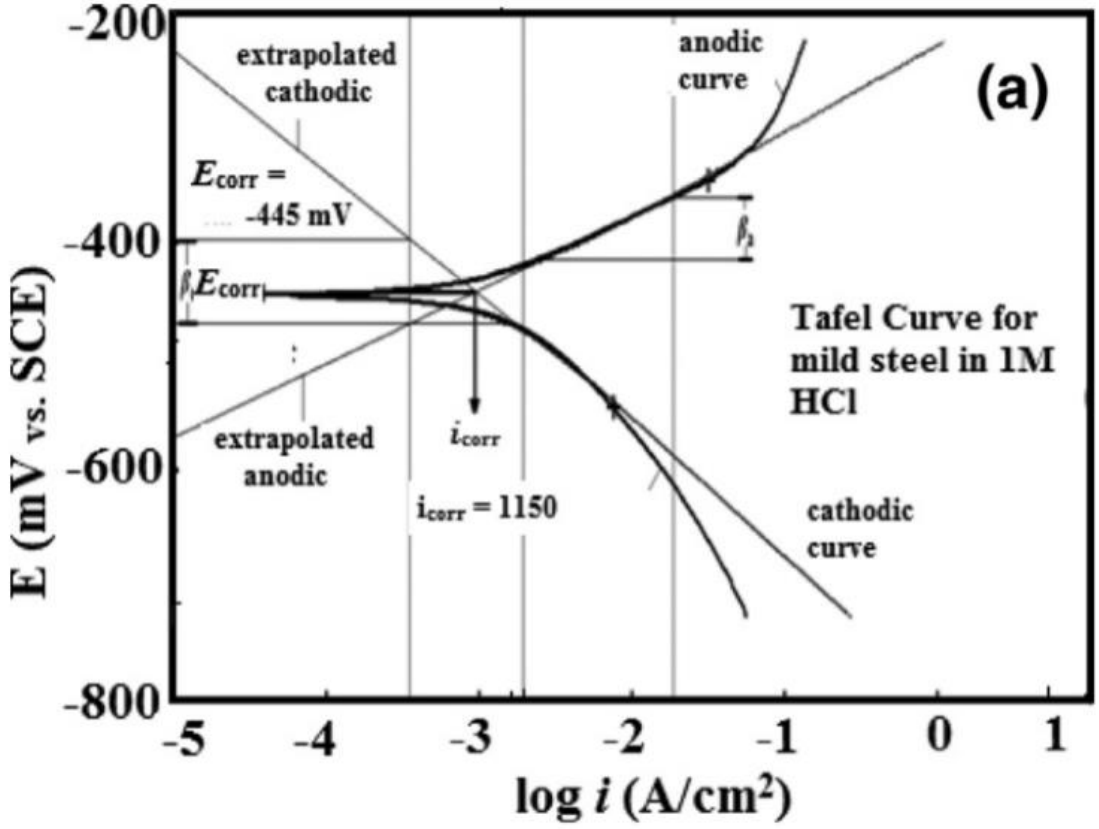

Figure 2.36 Schematization of the Tafel method (Bhan, Quraishi and Singh, 2014)

2.5 Discussion of the experimental results

2.5.1 Temperature measurement

The thermal cycle in Figure 2.19 is the starting point for the investigation on the microstructure of P20 steel. The schematization of the thermal cycle proposed in the section "Temperature measurement" must be reconsidered. To simplify the description, the system can be divided in beads and layers. The beads are the single tracks and the layer is the level in which the beads share the same z in a xyz coordinate system. Cooling rates, valley temperature, analysis of segregation and dilatometric data are key factors to understand the phase transformation during WAAM.

The valley and peak temperature related with the thermal cycle in Figure 2.19 are listed in Table 2.8.

Table 2.8 List of peak and valley temperatures for each deposited bead

# deposited bead	Peak T [°C]	Valley [°C]
Bead 1	910	260
Bead 2	550	300
Bead 3	420	320
Bead 4	370	330
Bead 5	350	200 [delay]

Table 2.9 shows the solid state transformation temperatures of the material.

Table 2.9 Solid state transformation temperature of the material

A_{c1} [°C]	A_{c3} [°C]	M_s [°C]	B_s [°C]
760	820	320	450

Analyzing the first block of the thermal cycle it can be seen that during the first heating the material undergoes complete austenitization at rapid cooling below the M_s. The amount of transformed austenite is function of the undercooling and it can be calculated with equation 2.11

$$1 - V_{\alpha'} = e^{\{\beta(M_s - T)\}} \qquad 2.11$$

Where $V_{\alpha'}$ is the fraction of martensite, β is a constant equal to -0.011, M_s is the martensite start temperature and T the temperature. According to this formula when the valley temperature is 260 °C the amount martensite is 0.49% and at 300 °C only 0.20%. For the discussion of the thermal cycle is important to take into account that the effect on the microstructure is controlled by the highest peak. In the case of the thermal cycle proposed in this study the second peak has a tempering effect on the martensite deposited during the first peak.

In this study it was not possible to provide CCT curve, thus TTT curves have been used. In Figure 2.37 the TTT curve is proposed. Cooling curves after each peak are also added to the diagram to study the phase transformation. It can be noticed that the cooling rates decrease as the heat source goes away from the measuring spot. By linear approximation of the cooling curve it is possible to

obtain the cooling rates listed in Table 2.10. The first cooling leads to the martensite transformation, afterwards the peaks act as tempering. The retained austenite can transform to martensite during the following cooling.

The problem is more complicated when thinking about each single bead. The thermal cycle described until now refers to the first bead of the layers. Looking at the second, third etc … the layout of the cycle changes completely.

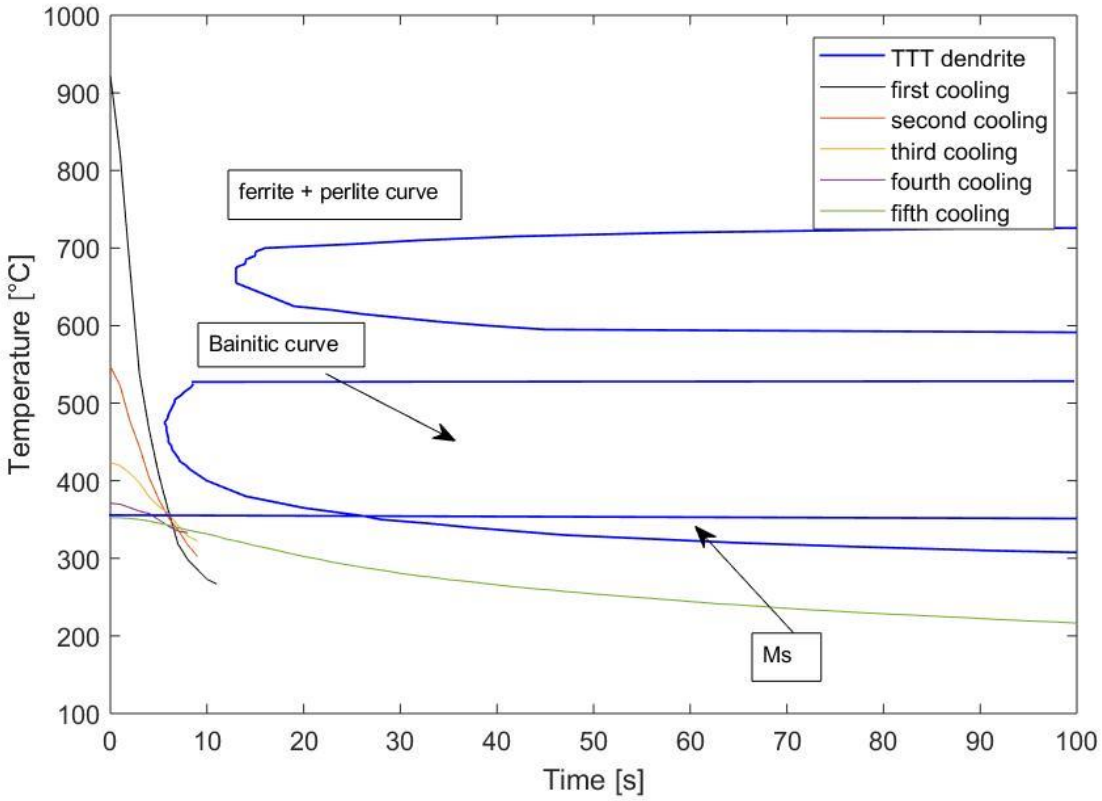

Figure 2.37 TTT diagram and cooling rates evolution during printing

Table 2.10 Cooling rates after each peak

# peak	Cooling rate [°C/s]
1	59.7
2	27.17
3	11.2
4	4.75
5	1.13

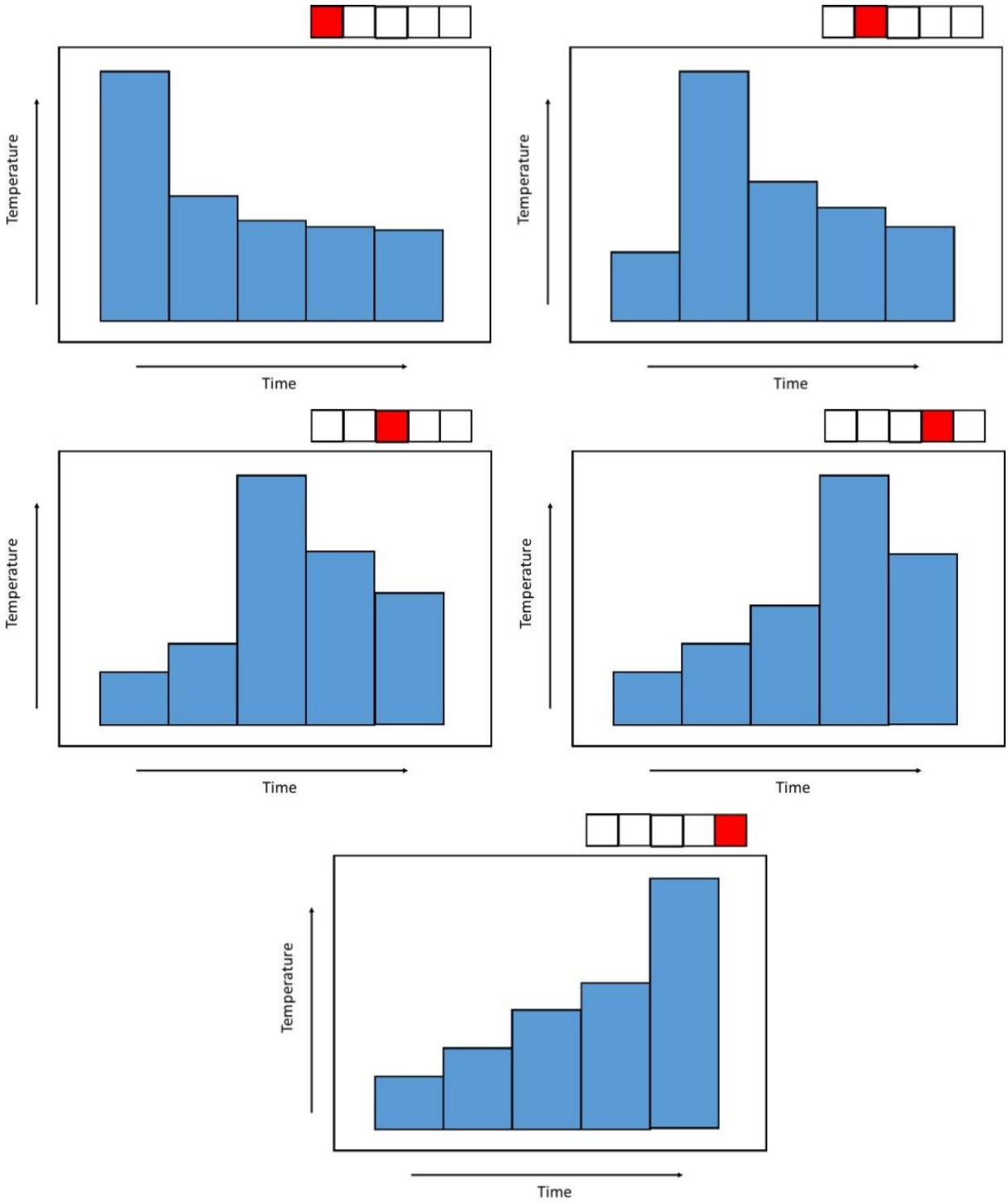

Figure 2.38 Schematization of the thermal cycle for a) first bead, b) second bead, c) third bead, d) fourth bead and e) fifth bead

Figure 2.38 is schematic representation of the thermal cycle based on the experimental results of the temperature measurement. Although it does not have any experimental value, it gives an idea of what could happen for the other beads. The peak temperature shifts to the right in the time axis and the cooling rate can also significantly change for each case because the material is already hot when the deposition re-starts.

The problem becomes much more complicated when printing the second layer. Deposition of the second layer start from the opposite direction compared to the previous one. This is done to increase the flatness of the surface. As can be seen in Figure 2.19 the heat cycle is affected by this strategy.

The second block is different from the first one, since it can basically be summarized by a pre-heating and final austenitization. The peak temperature is lower compared to the highest peak temperature in the first block, but the austenitization can favor recrystallization and transformation to the austenite phase. Figure 2.39 shows the TTT diagram of the material with the cooling after the final peak of the second layer. The other peaks are not reported in Figure 2.39 because their effect is covered by the complete austenitization of the final peak. As it can be seen the cooling curve is different from what has been seen in the first block and it intercepts the bainitic transformation.

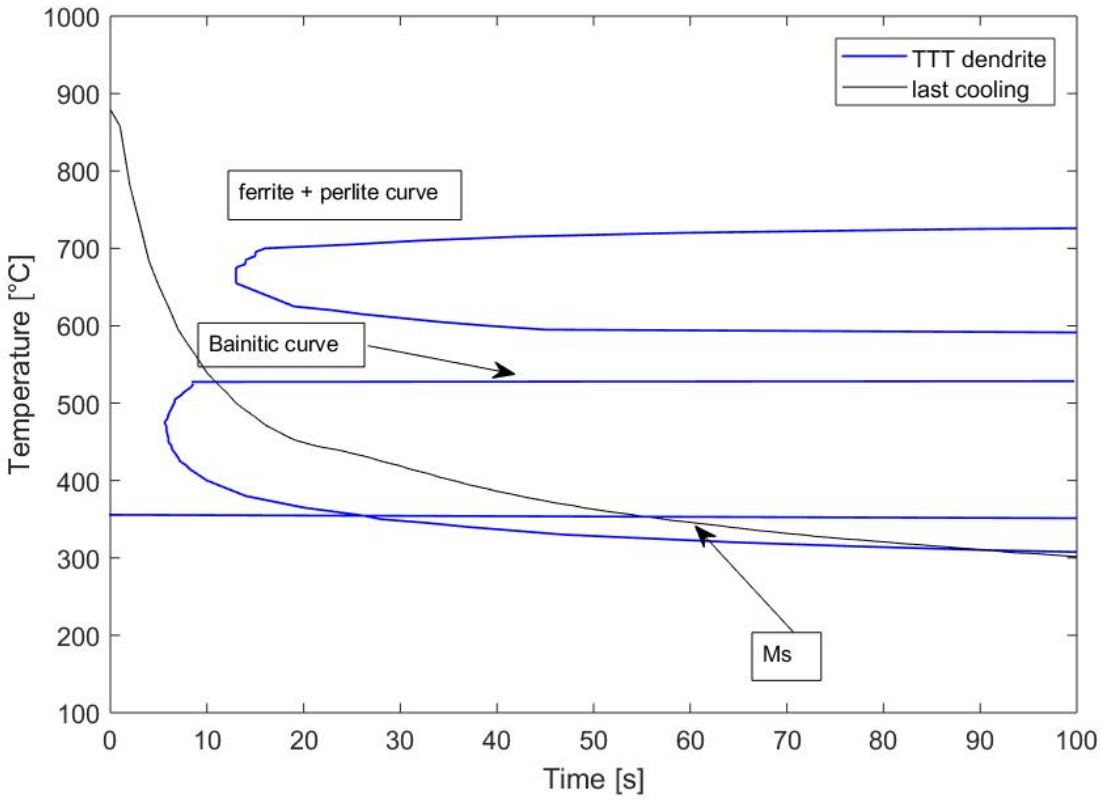

Figure 2.39 TTT diagram of P20 steel with cooling rate after final peak temperature of the second layer

2.5.2 Dilatometry

The microstructure of the quenched sample, cooled at 5°C/s and 1°C/s is proposed in Figure 2.40, 2.41 and 2.42 respectively. There is a gradual change in the microstructure. The dilatometric curve of the quenched sample shows evidence of martensitic transformation. The microstructure shows a martensitic microstructure colored in light brown. The dendrites are contoured by a white constituent which can be addressed to martensite/austenite island. The different behavior of the material at the dendrite boundary is due to segregation of alloying elements. Segregation of alloying elements such us Cr, Mo and Mn promote the shift of the M_s at lower temperature.

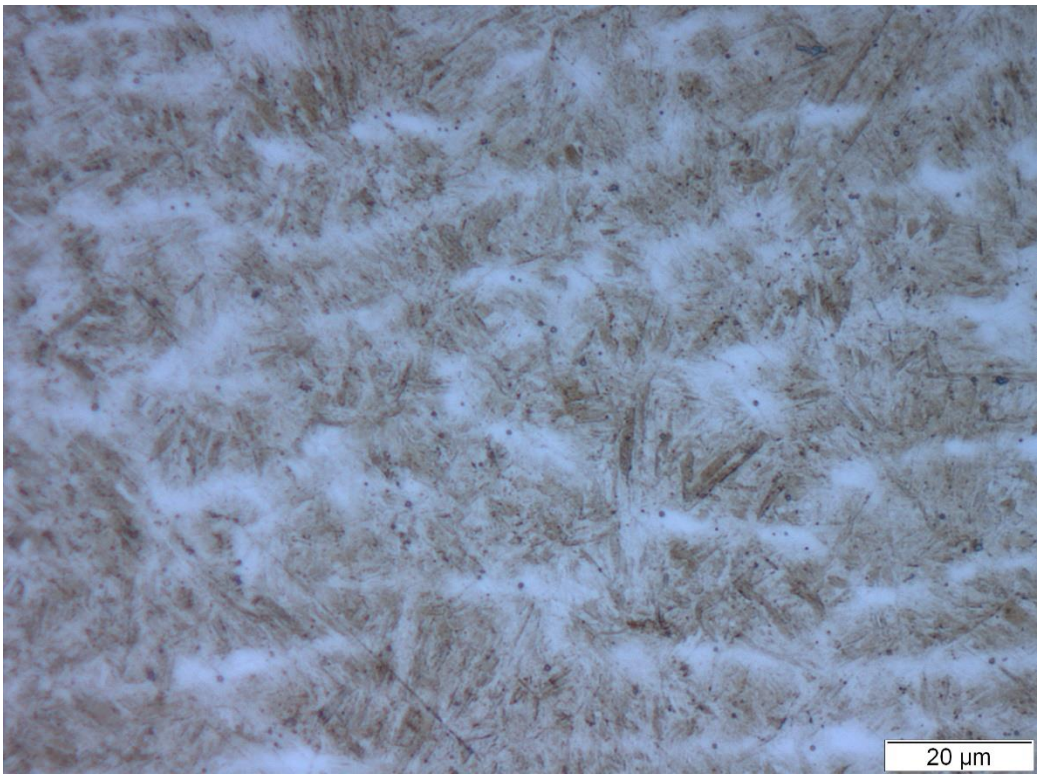

Figure 2.40 Microstructure of the quenched sample at 500X

The martensitic transformation takes place in two steps:

- STEP 1: Martensitic transformation occurs first in the low solute regions (intra-dendritic);
- STEP 2: Martensitic transformation occurs in the high solute regions (inter-dendritic). During this step auto-tempering of intra-dendritic martensite occurs. This causes the difference in color which can be noted in Figure 2.40;

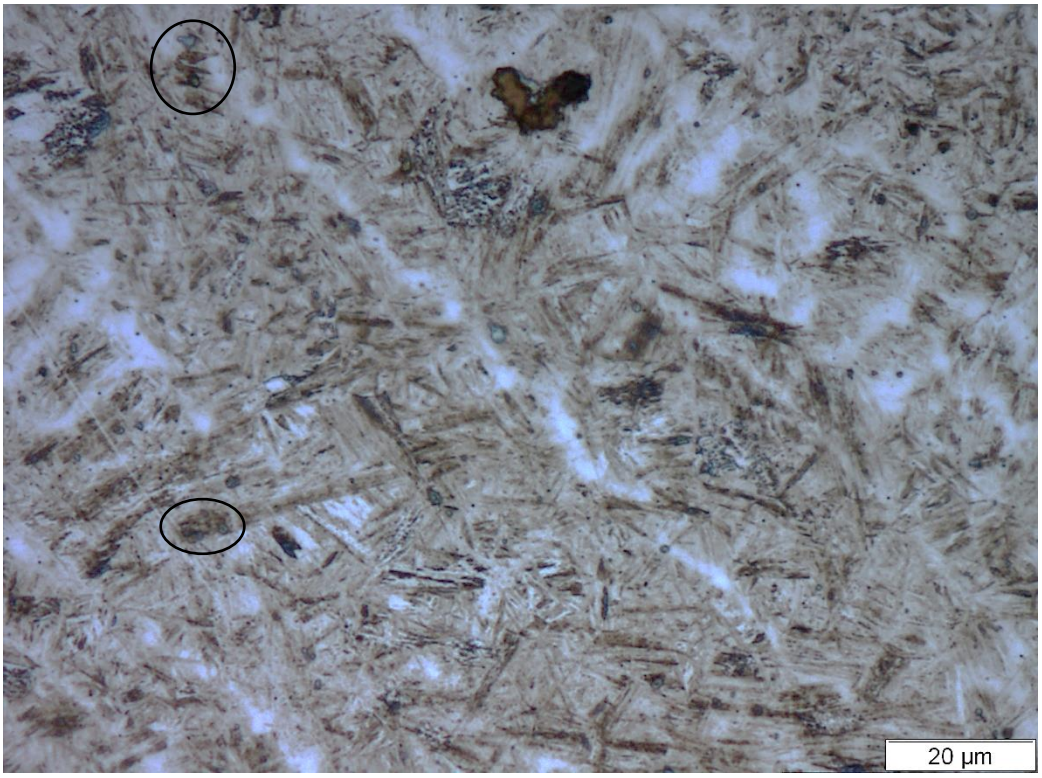

Figure 2.41 Microstructure of the sample cool at 5°C/s at 500X

The microstructure of the sample cooled at 5°C/s is proposed in Figure 2.41. The curve shows again evidence of martensitic microstructure. The microstructure observed is in agreement with dilatometry results. Some needles are detected, which were not present after quenching. Probably at some point the bainitic transformation started but its effect could not be resolved by the dilatometry. It needs to be considered that the temperature measurement refers to the surface, thus the cooling rates in the core of the sample can be lower. This can cause the formation of some bainitic needles (Yin, 2017).

In Figure 2.42 the situation is different. The microstructure seems to be a mixture of martensite and bainite. Higher fraction of dark needles are present. Another difference is that the dendrite boundary shows some sub-structures. In the case of the quenched sample and cooled at 5°C/s the dendrite is contoured by a white phase with no evident sub-morphologies. At higher magnification the bainitic needles are easier to distinguish. In Figure 2.42b) the martensitic matrix is evident as well as the bainite.

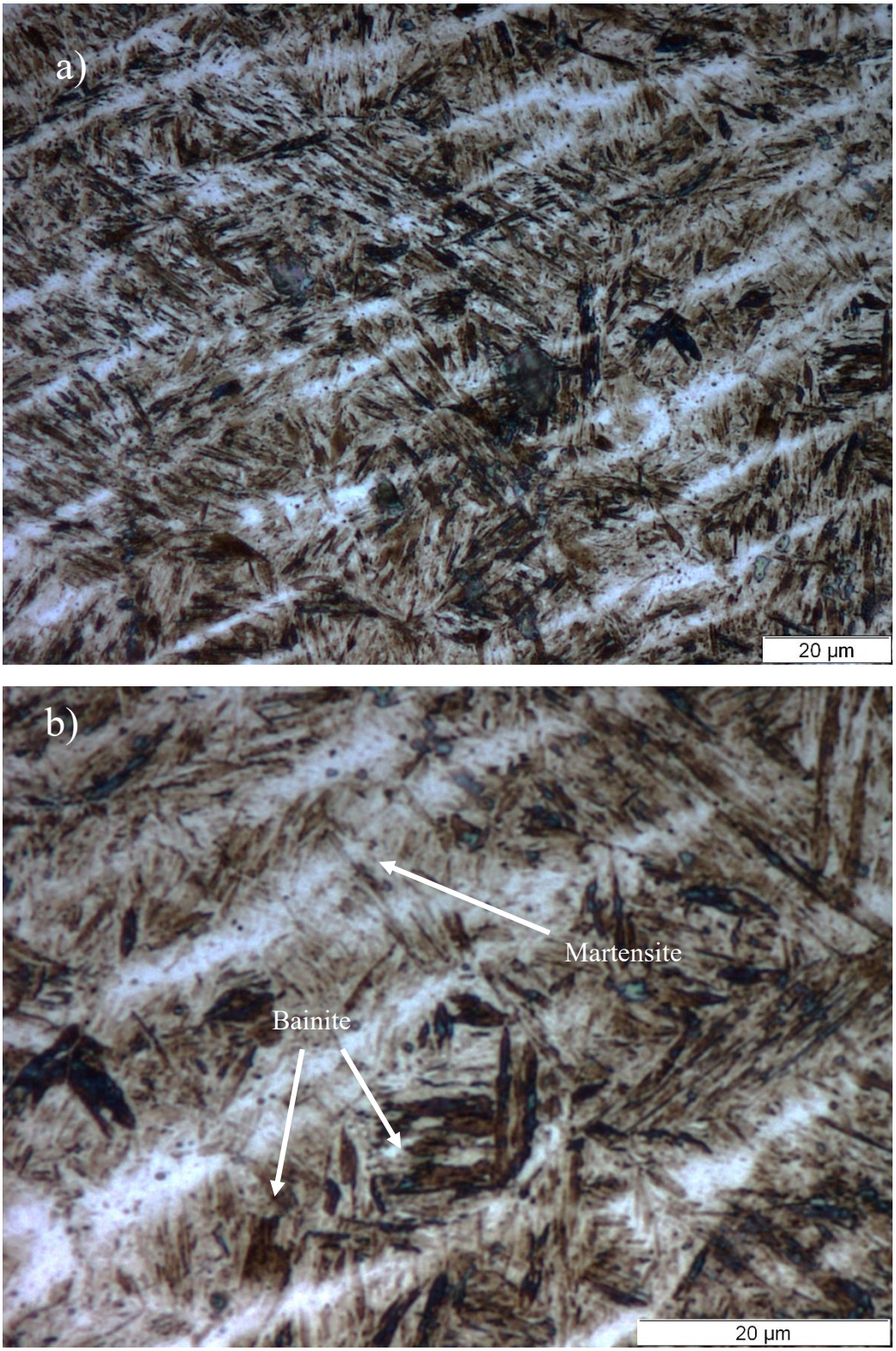

Figure 2.42 Microstructure of the sample cool at 1°C/s at a)500X and b)1000X

2.5.3 Effect of segregation on the microstructure

The chemical composition taken as reference for the study un segregation is given in Table 2.11.

Table 2.11 Chemical composition of the center of the dendrite and for segregation.

Element	C [wt%]	Cr [wt%]	Mn [wt%]	Mo [wt%]	Si [wt%]	Cu [wt%]	Al [wt%]	Ni [wt%]	P [wt%]	Ta [wt%]
Dendrite	0.263	1.755	0.718	0.327	0.476	0.35	0.025	0.15	0.012	0.115
Segregation peak #2	0.342	2.573	1.161	1.546	0.719	0.35	0.025	0.15	0.012	0.115

As can be seen for both cases, the carbon content is lower than the chemical composition of the raw material. This can be attributed to errors in the measurements.

Figure 2.43 shows the TTT curve for the measured segregation. It can be seen that the alloying elements have an effect on TTT curves. The ferrite/pearlite curve disappears at really high temperature which are not important for this case. The bainitic curve has a shift on the right, while the M_s moves towards a lower temperature.

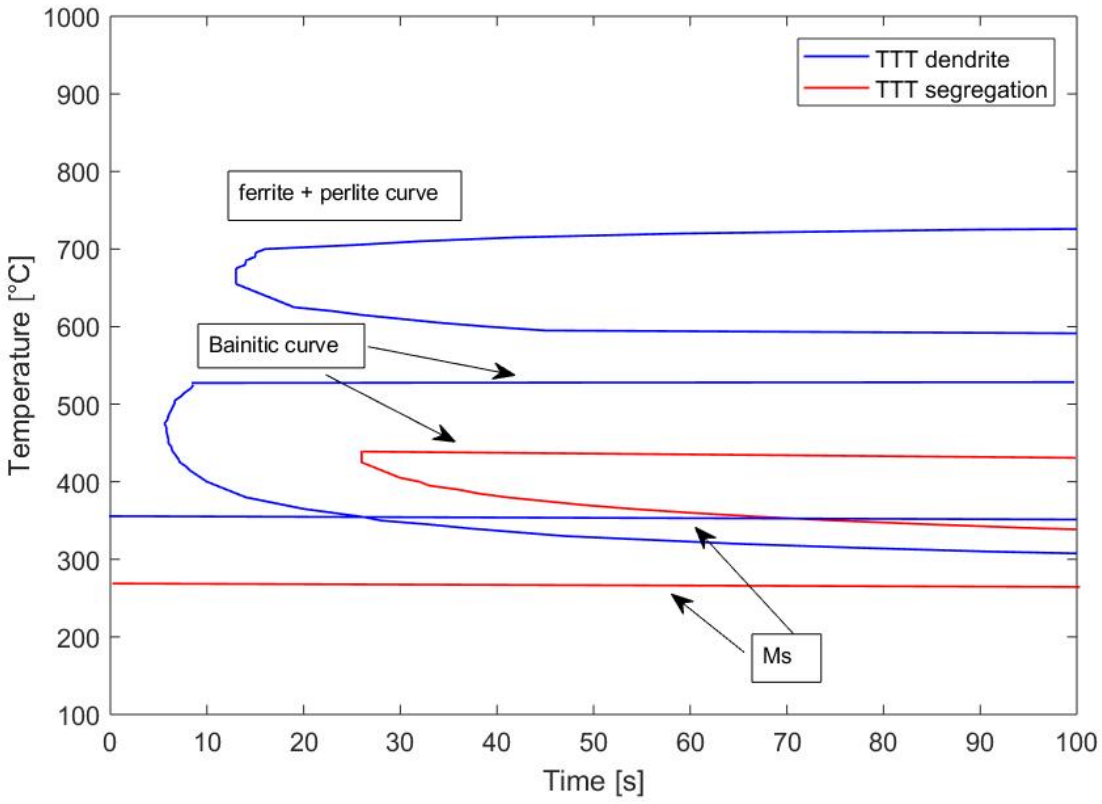

Figure 2.43 TTT curve for segregation of alloying elements

This explain why the microstructure has a white phase at the dendrite boundary after etching. During printing the boundary of the dendrite is characterized by a lower M_s temperature, thus the martensitic transformation starts following the center of the dendrite. As can be seen in figure 2.43 the center of the dendrite has smaller field where austenite is stable.

The thermal cycle in Figure 2.19 has been used to investigate the effect of segregation on the microstructure. For the first block and second block, the cooling curve after the austenitization peak have been added to the TTT diagram for both dendrite center and segregation, Figure 2.44 and 2.45 respectively. As can be seen in Figure 2.44 the boundary of the dendrite is prone to transform at lower temperature. This can increase the probability to have fresh M/A (martensite/austenite) constituents at the dendrite boundary, while in the center the martensite can be subjected to auto-tempering (Krupp et al., 2018).

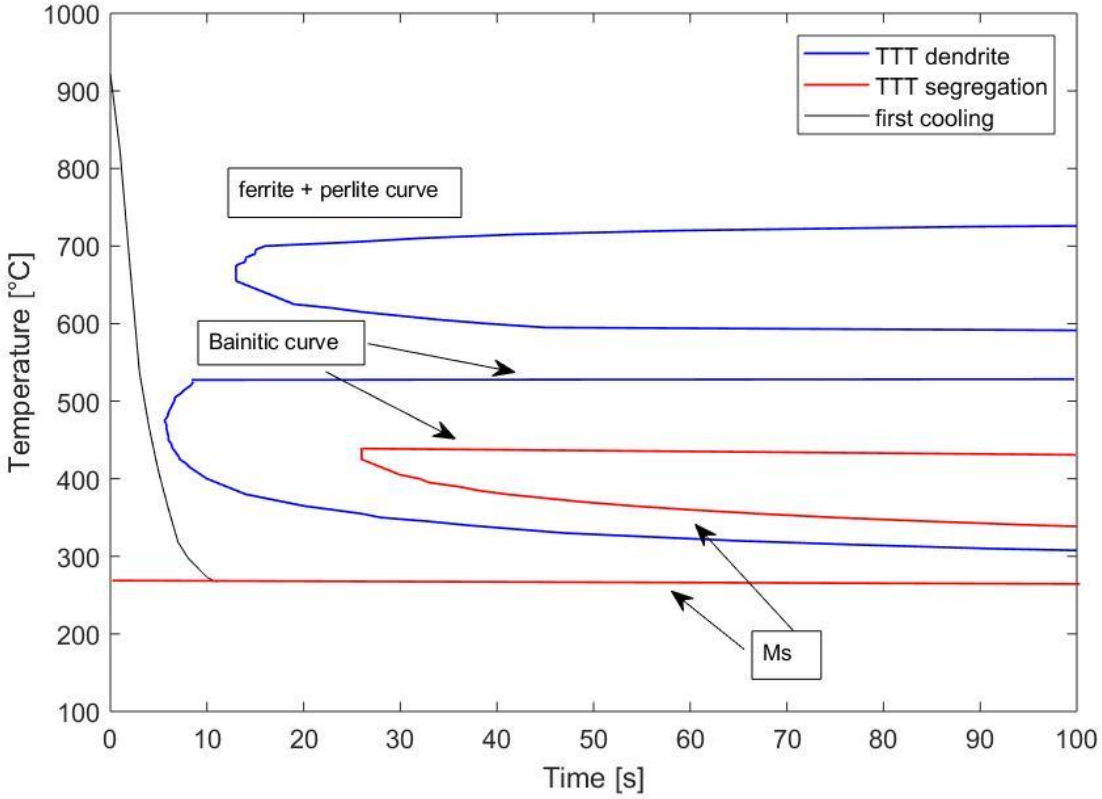

Figure 2.44 TTT curve for the center of the dendrite in blue and for the dendrite boundary in red. In black the cooling curve from the thermal cycle measurement after the last austenitization peak of the first block

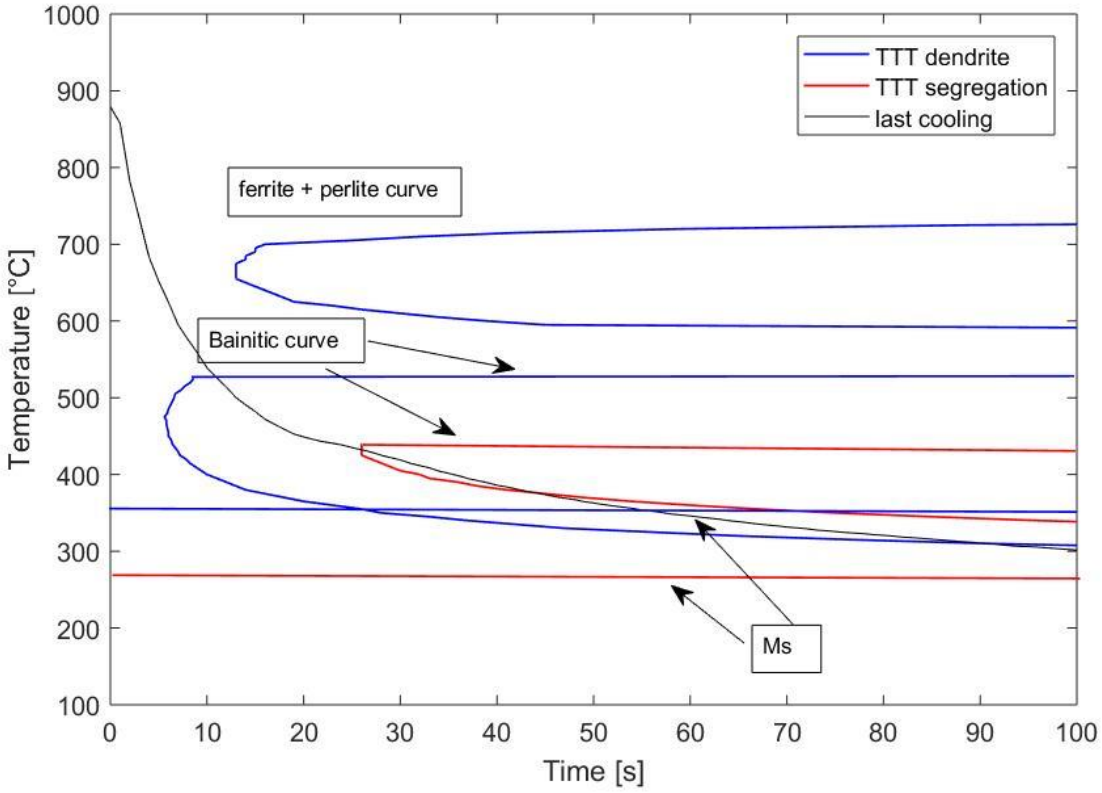

Figure 2.45 TTT curve for the center of the dendrite in blue and for the dendrite boundary in red. In black the cooling curve from the thermal cycle measurement after the last austenitization peak of the second block

In Figure 2.45 the situation is completely different. The cooling curve intercepts the bainitic transformation for both the TTT diagrams. During the deposition of the second layer the microstructure obtained in the first layer is transformed with different boundary conditions.

In conclusion it can be said that segregation has an effect on the microstructural constituents present in the material. It has been demonstrated that the different color in the martensite matrix can be attributed to area with different chemical composition which transforms in martensite upon cooling at different temperatures. The center is favored to form martensite (which self-tempers during cooling) and bainite. This behavior has already been reports in others works (Khan and Bhadeshia, 1990).

2.5.4 Microstructural investigation

The microstructure can be better analyzed after the discussion on the thermal cycle, dilatometry and effect of segregation. The microstructure was divided in constituents A, B and C. The microstructure is re-proposed in Figure 2.46 with all the constituents.

With the support of the segregation results and the TTT diagram is possible to say that the constituents A is the result of the martensitic transformation. The different color is determined by the presence of solute segregated at the dendrite boundary. In particular the white phase is fresh martensite and retained austenite, also called M/A constituents. The light brown constituents

martensite which is subject to self-tempering during cooling. The self-tempering occurs when the cooling rate under the M_s slows down, thus promoting partial tempering during the cooling.

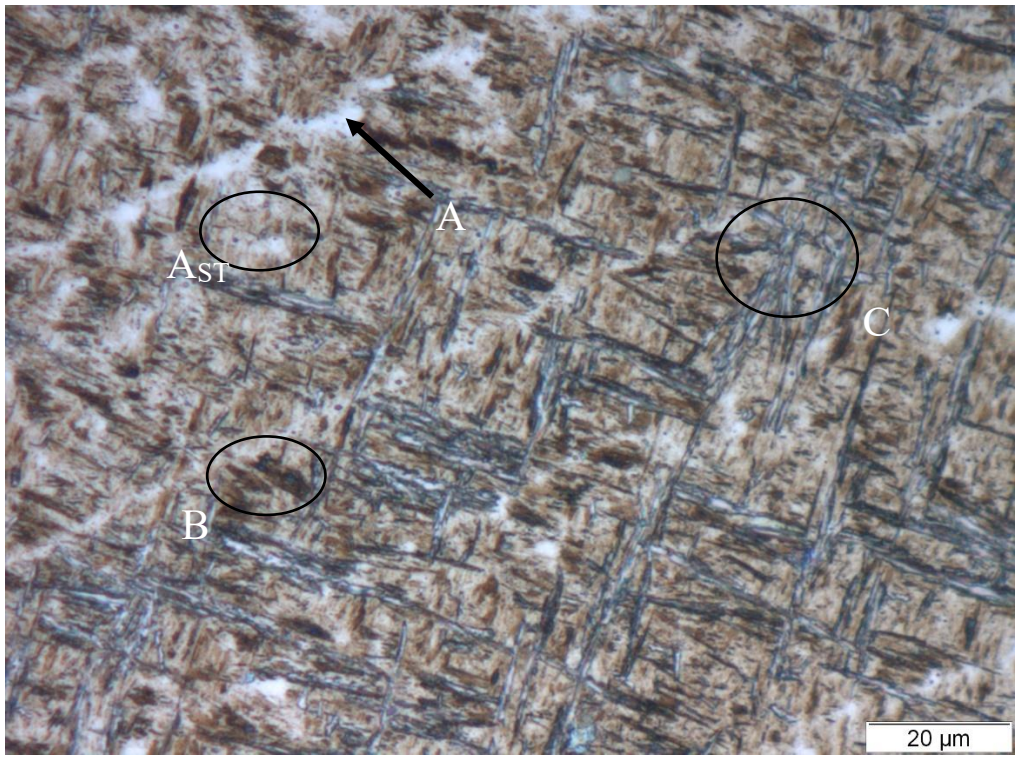

Figure 2.46 Microstructure indicative for all the constituents

The constituents B refers to bainite for the following reasons:

- The color addressed to bainite when etching with Nital is brown (Hairer et al., 2008);
- The morphology of lower bainite needles are similar to the B constituents (Yin, 2017);
- The study on the thermal cycle and its application on the TTT diagrams suggests the possibility to form a mixture of martensite and bainite;

The constituents C has not be revealed by the discussion of the thermal cycles, dilatometry and segregation. The metallurgical study using different etching technique gives some indication. According to (Erisir, Gümüs and Bilir, 2013) when using LePera etching the constituents are colored in different ways: ferrite is blue, bainite dark/brown and martensite is white. In Figure 2.47 the microstructure after LePera etching is shown. The microstructure reveals all the color typical of LePera etchant. White at the dendrite boundary, brown in the dendrite and blue for the acicular constituent. According to LePera the white constituent at the dendrite boundary is M/A islands, the brown bainite and the blue is ferrite. For the first two this is partially in line with what discussed. The brown constituent is a mixture of bainite and self-tempered martensite. Actually looking at the center of the dendrite the brown color is not uniform and some inhomogeneities are visible. For the white phase, it is in agreement with what stated.

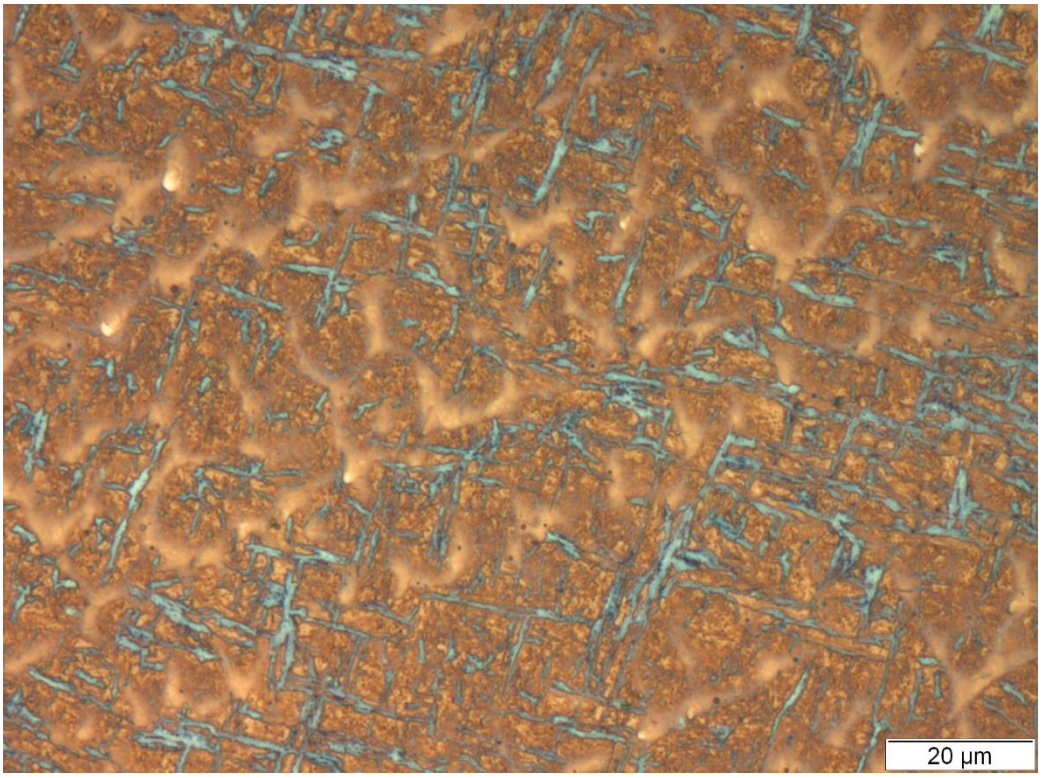

Figure 2.47 Microstructure of the last layer after etching with LePera

According to LePera the constituent C is ferrite. Ferrite can be present in weldments as acicular ferrite. This type of ferrite nucleated preferential at inclusions. The mechanism of growth of the ferrite is similar to the bainite (Bhadeshia and Honeycombe, 2017).

The amount of constituent markedly changes in the deposited material due to the different thermal cycles. A transition line is possible to detect between the uniformly treated microstructure and the partially treated one. Figure 2.48 shows a macro of the transition line between the two areas. The light colored microstructure refers to the upper layers, while the darkest to the bottom layers. This image is important because it shows how the microstructure starts to be uniformly treated after two layers.

Figure 2.49 shows the tempered microstructure for different layers. It can be seen that the amount of M/A constituents at the dendrite boundary is reduced and it's discontinuous, meaning that some of the martensite was subjected to tempering. The mixture of self-tempered martensite and bainite transformed in tempered structure where distinction between the two is not possible at the optic microscope. The ferrite plates change their color in white, but it seems they keep their morphology. This is reasonable because ferrite should not undergo any visible modification during tempering.

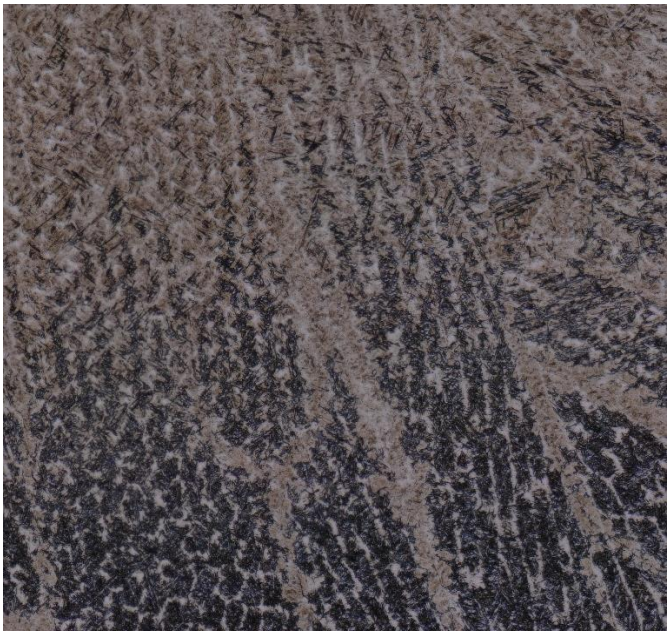

Figure 2.48 Transition line between the upper layers and the bottom layers

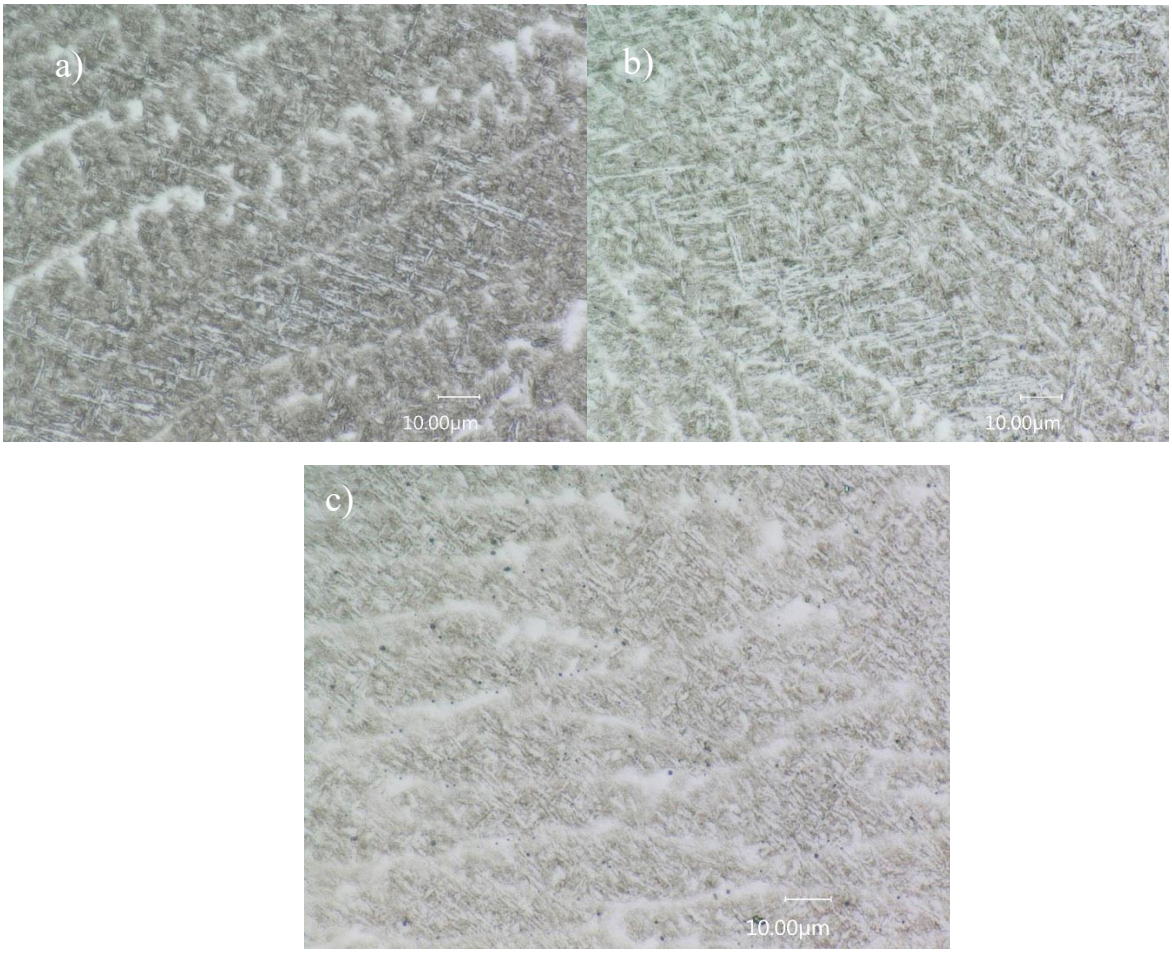

Figure 2.49 Microstructure of the tempered region in three different areas

2.5.5 Mechanical properties

The different mechanical behavior of the upper part of the wall and the bottom part is caused by the different thermal cycle that enhances solid-state phase transformations and further heat treatment of the beads beneath. The last layer is made of a complex microstructure with local different constituents in function of the process strategy and heat cycle. This microstructure is not homogenous in the last layers due to the thermal cycle. In Figure 2.50 a summary of the microstructure contained in the wall is proposed. It can be seen that the microstructure evolution during printing is in line with the hardness results in Figure 2.33 and 2.34. In fact in the last layer where the mixed microstructure is present the hardness is slightly lower and it reaches a value of 628 HV. This can be related to the effect of the repeated thermal cycle as well as for the presence of bainite and acicular ferrite which have lower hardness compared to martensite.

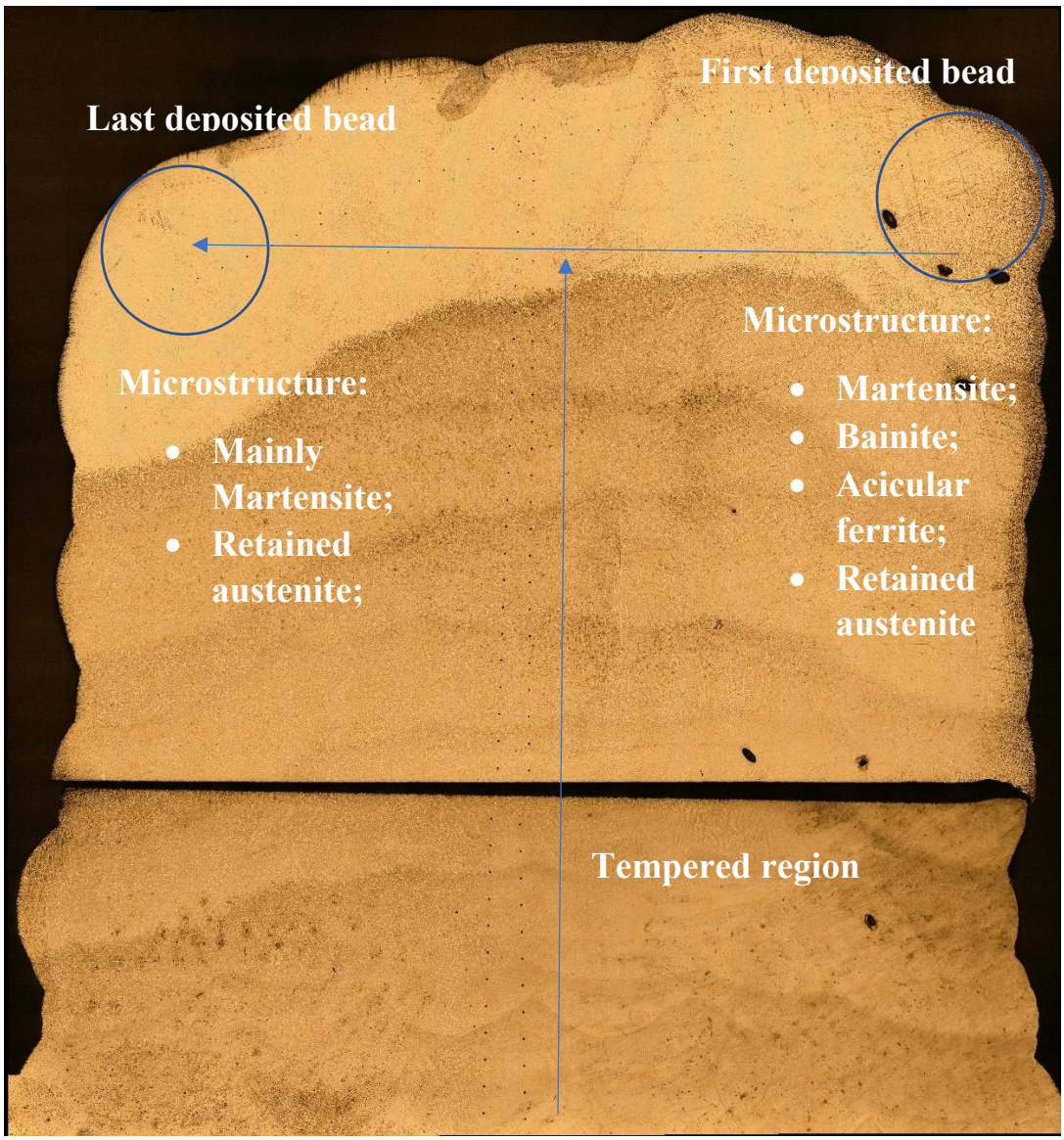

Figure 2.50 Illustration of the local microstructure of the wall

In the last deposited bead the microstructure is mainly martensitic, even if some small amounts of bainite and acicular ferrite have been detected. The hardness reaches 720 HV, higher than the first deposited bead of the layer. This proves what has been seen in the study of the thermal cycle and during the investigation on the microstructure. The microstructure is variegated and the effect of the process strategy is really influencing.

The decrease in hardness in the bottom layers can be attributed to the effect of tempering during the deposition. The hardness profile in Figure 2.33 depicts the tempering process of the microstructure. The trend is quite homogeneous and it shows some oscillations probably due to the several HAZ zones.

Other studies recognizes the modification of hardness behavior of this material (Chen et al., 2010). Short-time tempering can explain the observed decrease in hardness when the material is exposed to cyclic thermal treatment. (Chen et al., 2010) demonstrated that during short-time tempering most of the hardness drop occurs during the first seconds. In Figure 2.51 is proposed the hardness decrease in function of time at three different temperatures: 500°C, 600 °C and 700°C. In the case of the 700°C the as quenched hardness drops to less than the 55% after 0.05 s. Decreasing the temperature more time is needed to achieve the same tempering effect.

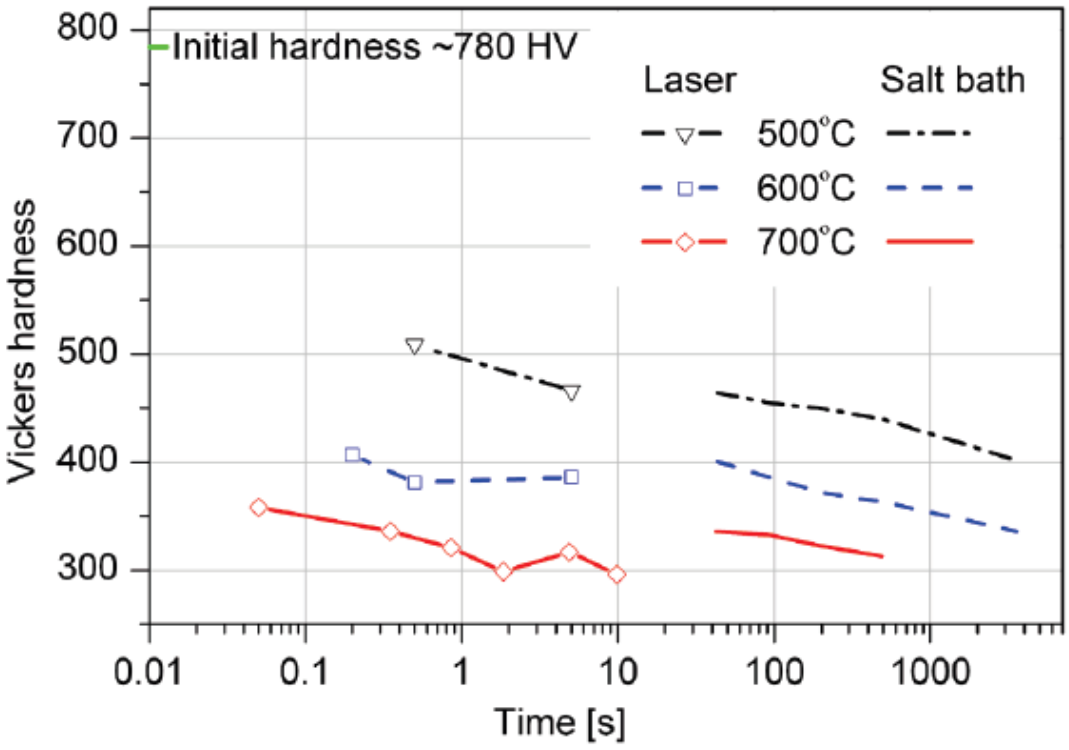

Figure 2.51 Effect of short time tempering on hardness of SURA B82 (Ahlström et al., 2010)

The decrease in hardness can be correlated with the tempering parameter defined as:

$$TP = T(logt + C) \quad 2.9$$

Where TP is the tempering parameter, T is the tempering temperature in Kelvin, t is the time and C is a constant that depend on the chemical composition of the alloy. Equation 2.10 is derived by Hollomon and Jaffe, assuming that during two different tempering condition TP_1 and TP_2 the hardness does not change:

$$T_1(logt_1 + C) = T_2(logt_2 + C) \quad 2.10$$

The concept is better explained in Figure 2.52. It can be seen that the same hardness value can be obtained with different set of tempering temperature T and holding time t. The main drawback of this model is the fact that it does not consider the microstructural changes that occur. In fact at higher temperature recrystallization and grain grow can occur, despite what happen at lower temperature when diffusion is less intense.

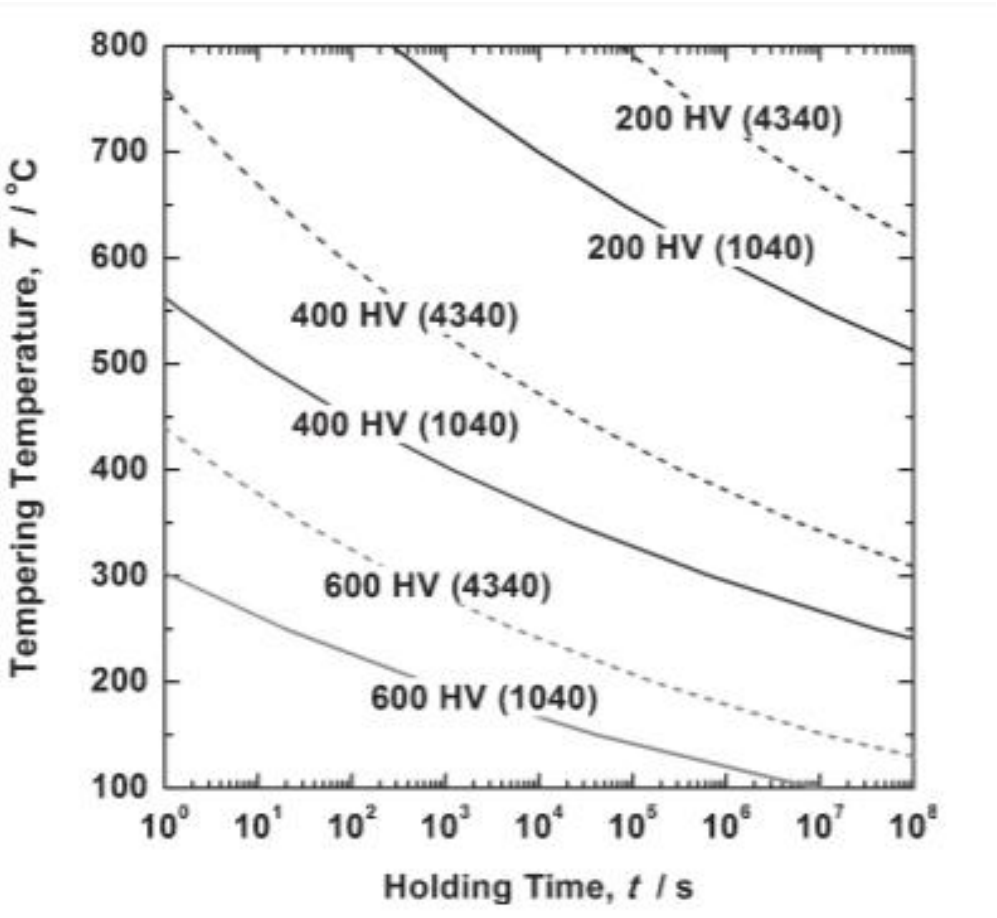

Figure 2.52 Iso-hardness curves as a fuction of tempering temperature and holding time (Ahlström et al., 2010)

In order to compare the obtained hardness values in the tempered region, hardness measurement have been performed also on the QT60 and QT5. The results are displayed in Table 2.12. The QT60 shows an higher decrease in the hardness due to the higher holding time. Different phenomena take place during the tempering stage. In particular for higher holding time, coarsening of the carbides and clustering can occur, inducing the hardness to drop. In the case of QT5 the holding time is less and it is possible that the tempering is only partial, thus it shows higher hardness.

Table 2.12 Hardness values of the two differently tempered dilatometric samples

Sample	Test Point	HV 0.5
TQ60	1	382
TQ60	2	383
TQ60	3	375
TQ5	1	443
TQ5	2	468
TQ5	3	446

2.5.6 Polarization test

The three analysed samples show no presence of passivation. The anodic part of the polarization curve increases with the applied voltage until it the current density reaches a plateau. The three curves in Figure 2.35 show different corrosion behaviour. The polarization curve for TM1 and TM2 have the same shape, suggesting that the corrosion mechanism is similar.

The specimen TM1 shows lower corrosion rate and higher corrosion potential compared to TM2. The sample TM3 has remarkable difference in the shape of the polarization curve. In particular, the anodic part of the curve has higher dissolution rate compared to TM1 and TM2. The corrosion rate is lower and the corrosion potential is shifted on the right.

Corrosion in weldments can be addressed to segregation of alloying elements, coupling of regions with different electrochemical activity, pitting, crevice, fretting corrosion, stress-corrosion and corrosion fatigue. In this case crevice, fretting, stress-corrosion and corrosion fatigue are not present.

The type of corrosion in the case of the polarization is considered as uniform corrosion, even though at the micro scale segregation of alloying elements and microstructure can induce different localized corrosion behaviour. During solidification the material experiences segregation of alloying elements between dendrites. Moreover each bead is heated up leading to:

- Partial re-melting;
- Recrystallization and grain growth (CGHAZ and FGHAZ);
- Phase transformation;
- Heat treatment;

During WAAM the aforementioned phenomena occur repetitively leading to complex microstructures. AISI P20 has a complex microstructure composed of martensite, bainite, acicular ferrite and retained austenite. The heat cycle leads to tempering of the microstructure. From the microstructural investigation it was recognized a vast precipitation of carbides in the martensite/bainite matrix and the acicular ferrite crossing the dendrite.

Along the height the material experiences different thermal history. In Figure 2.53 a scheme is proposed. Layer 7 is the last deposited layer and layer 1 is the first deposited layer. Along the z-axis the treatment time t_t decreases, thus the first printed layer experience longer thermal treatment.

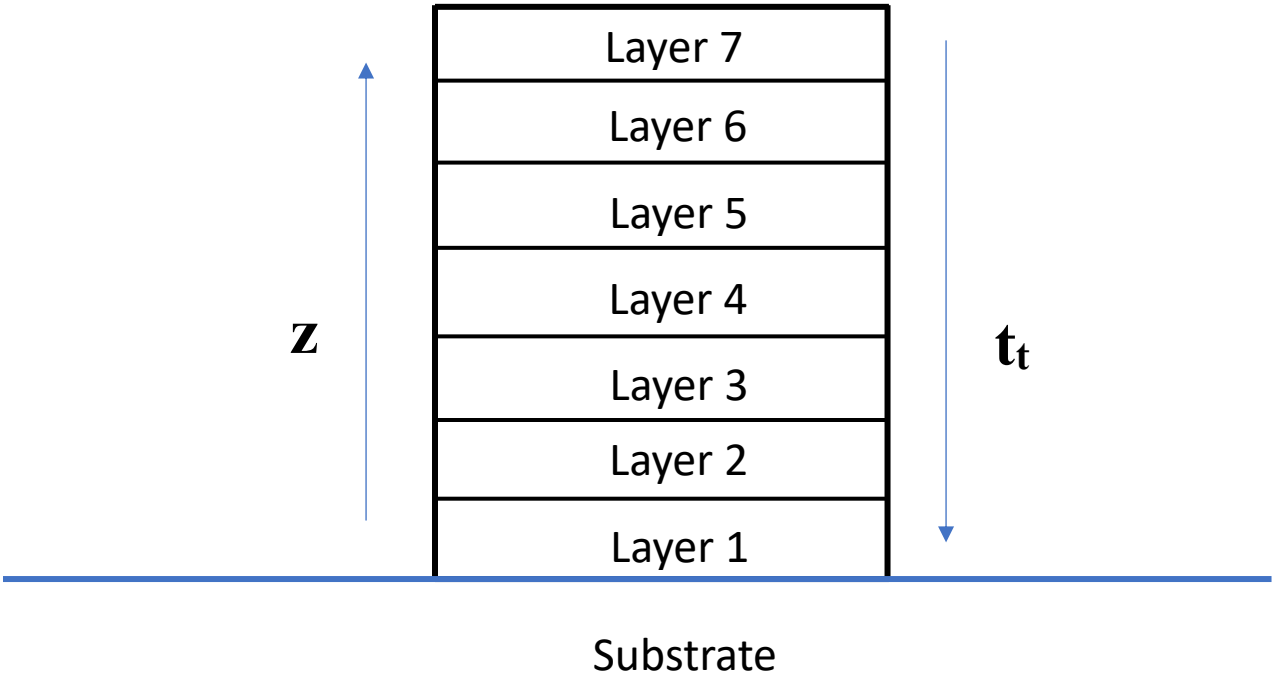

Figure 2.53 Scheme of the deposition process of a WAAM wall showing the trend of the time treatment along the z-axis

This z-dependant thermal history behaviour can affect the extent of segregation of the alloying elements and different microstructural features along the z-axis. Which causes differences in terms of corrosion performances.

Although the three samples presented different corrosion behaviour the results are comparable with what reported by Li et al. In Figure 2.54 the characteristic values of the polarization test on the AISI P20 printed with the SLM process are summarized. For the as-printed condition it can be seen that the value of corrosion potential and corrosion current density are comparable with the value in Table 2.7

Material	Ecorr vs. SCE (mV)	Icorr (μA cm^{-2})	ba (mV/ dec)	bc (mV/ dec)
As-printed	−494.9	12.86	55.87	−1100
450	−427.3	10.99	27.60	−943.9
550	−399.8	5.559	195.2	−331.0
As-supplied	−426.1	10.54	37.34	−916.6

Figure 2.54 Corrosion potential, corrosion density and Tafel cathodic and anodic slop of the AISI P20 printed with SLM process (Li et al., 2018)

In Figure 2.55 the polarization curve of the AISI P20 printed with the SLM technique. As it can be seen the polarization curve are comparable with the curves obtained in this study. It is also possible to note which is the effect of different post-process heat treatment to the corrosion performance. The samples were treated at 450°C and 550°C for 2 h. The heat treatment tends to increase the corrosion resistance of the material.

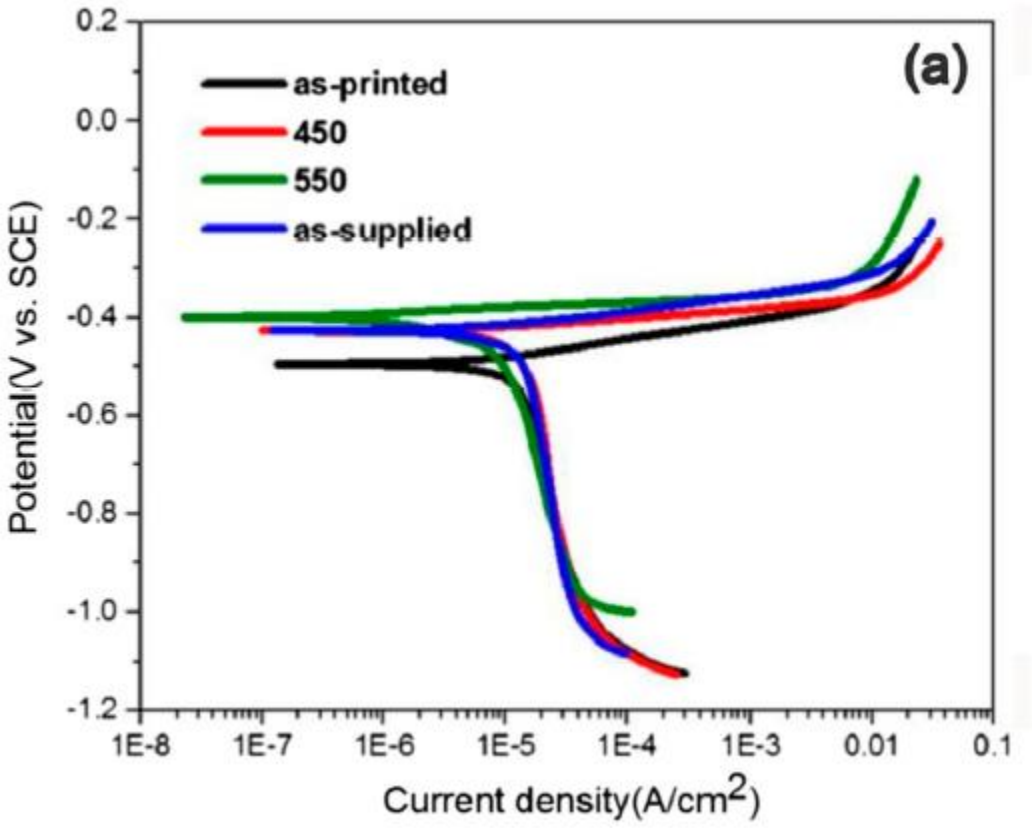

Figure 2.55 Polarization curve of the SLM printed AISI P20 steel and other counterparts (Li et al., 2018)

Conclusions

In this study an investigation on the microstructure, mechanical properties and corrosion resistance of AISI P20 steel has been proposed. The work answered some of the questions posed by the author. Using the information from the thermal cycle was possible to understand how the temperature evolves during and which is the influence of the deposition strategy. Measurement on the segregation with the EPMA analysis helps quantifying the amount of segregation and with the contribution of TTT diagram it was possible to identify the scenario upon cooling. The application of Nital and LePera etchants, with the support of the aforementioned experiments, it was possible to identify the microstructural constituents in the as-deposited microstructure: martensite, bainite, acicular ferrite and retained austenite. The quantification of these constituents varies locally due to the effect of the thermal cycle. In the layers beneath the situation is slightly different because the microstructure tempers due to the heat conducted into the workpiece during the printing. The microstructural difference between the bottom and upper layers brings to diversification in mechanical and corrosion properties.

It was questioned whereas the material could be used in the as-printed condition without the application of heat treatment. This study demonstrated that it is practically impossible to avoid post deposition heat treatment for this material. Even though the material performances are comparable to the data in literature the process does not have control on the microstructure.

Further improvement on this topic could be achieved with application of this study on a thermal simulation of the WAAM process. Afterwards it could be applied to the CCT diagram, yielding better quantification on the microstructural constituents upon cooling.

Bibliography

Ahlström, J. *et al.* (2010) 'Short-time tempering kinetics of quench hardened pearlitic steels', 46(June), pp. 1–6.

Barraclough, D. R. (1973) 'Etching of prior austenite grain boundaries in martensite', *Metallography*, 6(6), pp. 465–472. doi: 10.1016/0026-0800(73)90044-X.

Bhadeshia, H. and Honeycombe, R. (2017) *Acicular Ferrite*. 4th edn, *Steels: Microstructure and Properties*. 4th edn. Elsevier Ltd. doi: 10.1016/B978-0-08-100270-4.00007-X.

Bhan, C., Quraishi, M. A. and Singh, A. (2014) '2-Aminobenzene-1 , 3-dicarbonitriles as green corrosion inhibitor for mild steel in 1 M HCl : Electrochemical , thermodynamic , surface and quantum chemical investigation Journal of the Taiwan Institute of Chemical Engineers 2-Aminobenzene-1 , 3-dicarbonitriles as green corrosion inhibitor for mild steel in 1 M HCl : Electrochemical , thermodynamic , surface and quantum chemical investigation', *Journal of the Taiwan Institute of Chemical Engineers*. Elsevier Ltd., 49(June 2018), pp. 229–239. doi: 10.1016/j.jtice.2014.11.029.

Chen, J. *et al.* (2010) 'Experimental study of residual stresses in laser clad AISI P20 tool steel on pre-hardened wrought P20 substrate', *Materials Science & Engineering A*. Elsevier B.V., 527(27–28), pp. 7265–7273. doi: 10.1016/j.msea.2010.07.098.

Ding, D. *et al.* (2015a) 'A multi-bead overlapping model for robotic wire and arc additive manufacturing (WAAM)', *Robotics and Computer-Integrated Manufacturing*, 31, pp. 101–110. doi: 10.1016/j.rcim.2014.08.008.

Ding, D. *et al.* (2015b) 'Process planning for robotic wire and arc additive manufacturing', *Proceedings of the 2015 10th IEEE Conference on Industrial Electronics and Applications, ICIEA 2015*, pp. 2000–2003. doi: 10.1109/ICIEA.2015.7334441.

Ding, D. *et al.* (2015c) 'Wire-feed additive manufacturing of metal components: technologies, developments and future interests', *International Journal of Advanced Manufacturing Technology*, 81(1–4), pp. 465–481. doi: 10.1007/s00170-015-7077-3.

Erisir, E., Gümüs, S. and Bilir, O. G. (2013) 'Microstructural Characterization of Medium Carbon Dual Phase Steels After Intermediate Quenching', *Metal*, 15, pp. 1–6.

Graf, M. *et al.* (2018) 'Numerical simulation of metallic wire arc additive manufacturing (WAAM)', *AIP Conference Proceedings*, 1960(May). doi: 10.1063/1.5035002.

Hairer, F. *et al.* (2008) 'Etching techniques for the microstructural characterization of complex phase steels by light microscopy', *Int. Doctoral Seminar, Smolenice, SK*, pp. 50–54.

Hanamura, T. *et al.* (2013) 'Effect of Austenite Grain Size on Transformation Behavior, Microstructure and Mechanical Properties of 0.1C–5Mn Martensitic Steel', *ISIJ International*, 53(12), pp. 2218–2225. doi: 10.2355/isijinternational.53.2218.

Hu, Z., Qin, X. and Shao, T. (2017) 'Welding Thermal Simulation and Metallurgical Characteristics

Analysis in WAAM for 5CrNiMo Hot Forging Die Remanufacturing', *Procedia Engineering*. Elsevier B.V., 207, pp. 2203–2208. doi: 10.1016/j.proeng.2017.10.982.

Khan, S. A. and Bhadeshia, H. K. D. H. (1990) 'The bainite transformation in chemically heterogeneous 300M high-strength steel', *Metallurgical Transactions A*, 21(3), pp. 859–875. doi: 10.1007/BF02656570.

Krupp, U. *et al.* (2018) 'The Potential of Self-Tempered Martensite and Bainite in Improving the Fatigue Strength of Thermomechanically Processed Steels', 20006. doi: 10.1051/matecconf/201816520006.

Li, H. X. *et al.* (2018) 'Selective laser melting of P20 mould steel: investigation on the resultant microstructure, high-temperature hardness and corrosion resistance', *Powder Metallurgy*, 61(1), pp. 21–27. doi: 10.1080/00325899.2017.1368965.

Mccafferty, E. (2005) 'Validation of corrosion rates measured by the Tafel extrapolation method', 47, pp. 3202–3215. doi: 10.1016/j.corsci.2005.05.046.

Nishimoto, K. and Ogawa, K. (2016) 'Corrosion properties in weldments of stainless steels (1). Metallurgical factors affecting corrosion properties', 7116(June). doi: 10.1080/09507119909452061.

Ralston, K. D. and Birbilis, N. (2010) 'Effect of Grain Size on Corrosion : A Review', 66(7), pp. 1–13.

Rosenthal, D. (2017) 'Etude theorique du regime thermique pendant la soudre á l'arc.', *Congrés national des sciences*, 31(0), pp. 1277–1292.

Schmidt, D. P. *et al.* (2015) 'CORROSION OF 3D PRINTED STEEL', (October).

Solomon, H. D. (1993) 'Fundamentals of Weld Solidification', *ASM International*, 6, pp. 45–54. doi: 10.1361/asmhba000.

Vieira, I. *et al.* (2017) 'A Dilatometric Study of Tempering Complemented by Mössbauer Spectroscopy and other Characterization Techniques', *Scientific Reports*. Springer US, 7(1), p. 17337. doi: 10.1038/s41598-017-17654-x.

Wang, F. *et al.* (2013) 'Microstructure and mechanical properties of wire and arc additive manufactured Ti-6Al-4V', *Metallurgical and Materials Transactions A: Physical Metallurgy and Materials Science*, 44(2), pp. 968–977. doi: 10.1007/s11661-012-1444-6.

Xu, X. *et al.* (2017) 'Microstructural evolution and mechanical properties of maraging steel produced by wire + arc additive manufacture process', *Materials Characterization*. Elsevier, (April 2018), pp. 0–1. doi: 10.1016/j.matchar.2017.12.002.

Yang, H. S. and Bhadeshia, H. K. D. H. (2009) 'Austenite grain size and the martensite-start temperature', *Scripta Materialia*, 60(7), pp. 493–495. doi: 10.1016/j.scriptamat.2008.11.043.

Yin, J. (2017) *Formation of Bainite in Steels*.